DOCTOR
OF
PHILOSOPHY

Giovanni
TANDA

The City University
London
1996

APPLICATION OF OPTICAL METHODS TO THE STUDY OF CONVECTIVE HEAT TRANSFER IN RIB-ROUGHENED CHANNELS

by

Giovanni Tanda

A Thesis submitted to The City University of London
for the degree of Doctor of Philosophy in Mechanical Engineering

Department of Mechanical Engineering and Aeronautics
Thermo-Fluids Engineering Research Centre
April 1996

DECLARATION

No portion of the work referred to in this thesis has been submitted in support of an application for another degree or qualification of this or any other university or other institution of learning in the U.K. or abroad.

ACKNOWLEDGEMENTS

The first experimental part of the work reported in this thesis was carried out while the author was spending a six-month period at City University, London, partially sponsored by an Italian Government MURST 60% grant. The author is grateful to Prof. J.Stasiek and Prof. M.W. Collins for their continuous help and supervision for the work developed in this project.

The author is also indebted to Prof.Guglielmini for his uninterrupted interest, encouragement and suggestions during the research activity, related to this project, conducted at the Dipartimento di Termoenergetica e Condizionamento Ambientale (DITEC), Faculty of Engineering, University of Genoa, Italy.

Finally, thanks are expressed to Mr. and Mrs. Dugard, for the considerable help given to the author and his family during their stay in London.

ABSTRACT

The non-invasive liquid-crystal and schlieren methods have been applied to the study of convective heat transfer in rib-roughened channels.

The importance of investigating heat transfer from rib-roughened surfaces and of using non-invasive tools to gain information on thermal fields for similar complex geometries is stressed in Chapter 1.

Chapter 2 is devoted to a description of main important published papers related to this project. Firstly, studies concerning heat transfer from rib-roughened surfaces in forced and free convection are listed and discussed in detail. Moreover, a literature survey on optical methods in heat transfer is presented, with special attention to the methods (liquid-crystal thermography and schlieren) applied in this study.

Experiments performed by using liquid-crystal thermography are presented and discussed in Chapter 3. Three configuration geometries have been investigated: a smooth channel (having flat plates) and two different ribbed channels. The investigated heat transfer mechanism was forced convection. These experiments were performed at City University, London.

Chapter 4 is devoted to experiments performed by using the schlieren optical technique. Again, the experimental study included a preliminary activity on smooth channels, followed by tests performed for rib-roughened channels. The heat transfer mechanism was natural convection. These experiments, which constitute the main body of the project, were conducted at the Dipartimento di Termoenergetica e Condizionamento Ambientale, Università di Genova, Italy.

Finally, most important conclusions are drawn in Chapter 5. Details of relationships between the recorded optical data and the thermal field (or heat transfer coefficients) are reported in Appendix A1 and A2 for the liquid-crystal thermography and the schlieren method, respectively.

TABLE OF CONTENTS

NOMENCLATURE

Note: only the most relevant and recurrent symbols are included here

A	heat transfer surface area, flow area
C	Gladstone-Dale constant, thermal conductance
c	speed of light
D	diameter
d	(equivalent) diameter
e	rib height
f	friction factor
Gr	Grashof number (=Ra/Pr)
g	acceleration of gravity
k	thermal conductivity
H	(channel) height
h	heat transfer coefficient
L	(channel) length
Nu	Nusselt number
n	index of refraction
P	rib pitch, pressure
Pr	Prandtl number
Q	heat flux
q	specific heat flux
R	(ideal) gas constant
Ra	Rayleigh number
Re	Reynolds number
S	wall spacing
St	Stanton number (=Nu/RePr)
T	temperature
t	thickness
x,y,z	geometric coordinates
w	velocity, rib width

α	angular deflection of light ray, rib angle-of-attack
β	coefficient of thermal expansion
Δ	difference, light ray deviation
μ	dynamic viscosity
ν	kinematic viscosity
ρ	density
τ	time
θ	dimensionless temperature

Subscripts

air	air
av	average
c	cold
f	fluid
fd	fully developed
fp	flat plate
h	hot
max	maximum
o	reference
r	rough
s	smooth
s,a	surface, air side
s,w	surface, water side
tp	test plate
w	wall

CHAPTER 1. INTRODUCTION

Heat transfer phenomena play an important role in numerous engineering applications. The aim of the discipline of heat transfer is to describe precisely the way in which the dissimilarity between temperatures of two systems (which provokes a net heat transfer exchange) governs the magnitude of the heat transfer rate Q. Generally speaking, experience shows that the heat transfer rate function Q depends on the temperatures of the two interacting systems, their thermophysical properties, size, geometric shape, relative movement or flow, and time. Knowledge of the specific mode of heat transfer (conduction, convection, and radiation) enables one to consider simpler versions of the relationship between the cause (dissimilarity between temperatures of the two systems) and the effect (heat transfer rate). For instance, in convective heat transfer, which is the major heat transfer process occurring between a solid wall and a fluid, the conventional approach consists of relating the heat transfer rate Q to the temperature difference between the two systems $T_A - T_B$ through the heat transfer surface area A and the convective heat transfer coefficient h:

$$Q = h\ A\ (T_A - T_B) \tag{1.1}$$

The evaluation of the heat transfer coefficient, which often constitutes a very demanding question, is only the starting point in the practice of heat transfer engineering. Two large classes of practical applications need a further investigation of Eq.(1.1) to achieve the relevant objectives.

The first class of problems includes applications in which a *heat transfer enhancement* is required. Bearing Eq.(1.1) in mind, it means that the major task is the augmentation of the heat transfer rate Q under the same temperature difference $(T_A - T_B)$ between the interacting systems. In heat exchanger design, for example, if the temperatures of the two systems are given, it is extremely desirable to have the maximum heat transfer rate between the systems for the assigned heat transfer area (or exchanger size).

The second class involves applications in which the main concern is the overheating of the warm surface (at temperature T_A) that produces the heat transfer rate Q. In a tightly packaged set of electronic circuits, Q is generated by Joule heating, while T_B is provided by an external fluid (ambient air, for instance). The temperature of the electrical conductors

(T_A) cannot rise too much above the ambient temperature, because high temperatures threaten the error-free operation of the electrical circuitry and tend to reduce the application life of the components themselves. In this kind of application the main objective is the *thermal control*: in fact, the high temperature T_A must be kept below that critical domain where the characteristics of the hot surface (e.g., the mechanical strength) deteriorate.

For both the above-mentioned classes of problems, the key parameter to investigate, to control and even to maximise is the heat transfer coefficient h or the product between h and the heat transfer surface area A (often called *thermal conductance*). The evaluation of the heat transfer coefficient, through experiments or numerical means, is not a simple matter. The more complicated the geometry or the flow, the more demanding is the estimate of heat transfer coefficient. From the experimental point of view, a large category of convective phenomena can be investigated by using *optical techniques*. Optical measurement of a temperature field (to which the heat transfer coefficient is directly related) has many advantages over other techniques: for instance, it enables a simultaneous analysis of a large fluid region to be performed and this in the absence of instrument probes which could influence the phenomenon. In recent years, the rapid evolution of computer facilities (image digitising and processing systems, dedicated software) has made the use of some optical tecnhiques (liquid crystal and schlieren methods) possible from a *quantitative* standpoint and no longer for a qualitative observation only. This possibility has opened new frontiers to scientists and engineers engaged in heat transfer problems, giving them the chance to conduct experiments on complex flow or geometry with the aid of simple and reliable measurement means.

Among the optical methods suitable for evaluating thermal fields / heat transfer coefficients, attention was focused, in this project, on two specific techniques: *the liquid-crystal* method and the *schlieren* method. While liquid crystal methods are generally used to measure the thermal field on a solid surface, the schlieren technique enables the temperature field in transparent fluids to be determined. Besides, the two methods are based on different physical principles: liquid crystals exhibit a selective index of reflection of white light depending on their temperature, while the schlieren effect is due to the deflection of light passing through a

non-isothermal flow. The two methods have in common their relative simplicity, ease of operation and low cost when compared with other optical techniques (such as interferometry). The last attributes make their application very interesting in a wide field of engineering problems.

In the present study, the above-mentioned optical methods have been applied to systems consisting of rib-roughened (and smooth) channels cooled in forced/free convection. As will be documented later, this kind of geometry is encountered in *heat transfer enhancement* as well as in *thermal control* problems. In fact, keeping in mind the simplest heat transfer geometries occurring in several high flux applications (i.e. of flat surfaces or smooth inner/outer cylindrical surfaces), a very common practice to increase heat transfer coefficients in forced convection consists of artificially roughening the surface by fitting protruding elements such as ribs. The use of repeated ribs causes a break-up of the laminar sublayer and creates local wall turbulence due to flow separation and reattachment between ribs, which greatly enhances the heat transfer. In other applications, the roughness elements occur naturally (for instance in electronic circuit boards and microelectronic chip modules). Here the objective is to understand the thermal behaviour of rough surfaces (both in forced and free convection) when a given amount of heat flux is dissipated into the cooling fluid.

The specific applications for which heat transfer characteristics from rib-roughened surfaces are of great importance will be presented in the following sections 1.1 and 1.2. Finally, the role played by optical methods in experimental investigations of convection over this complex geometry will be discussed in the section 1.3 of this Chapter.

1.1 Heat transfer enhancement

Roughened heat transfer surfaces can be encountered in engineering problems which are extremely diverse. One of the first applications of rib-like geometries was in the field of gas-cooled reactors. Even though gases are not good heat-transfer media, they have been extensively used as coolants in reactors owing to their low neutron absorption and low chemical activity. Usually the cooling gas flows in annular gaps between the external surface of the fuel rod and the inner surface of the confining block. In Fig.1.1 a standard fuel element installed in the core of a HTTR

(High Temperature Engineering Test Reactor) is shown (Takase et al.,1994). The element consists of a hexagonal graphite block with a number of holes in which the fuel rods are inserted. In this application the coolant is helium (heated from 395°C up to 950°C) at the pressure of 4 MPa. Ribs or artificial roughness elements can be used in order to enhance forced convection heat transfer from the external surfaces of the rods. Adding the ribs to the external rod surface increases the turbulence in the annular flow. As a consequence, both heat transfer and friction losses are increased. While the latter effect implies a higher amount of power required to pump the fluid (which generally does not constitute a problem), the former effect enables the core power density to be increased, thus reducing the electrical power generating costs.

In the last decade, the demand for increasing thermal efficiency in turbomachinery and other rotary systems has promoted a great effort in the development of efficient techniques for cooling turbine blades. Internal cooling technologies, involving passages between roughened surfaces, have been applied to advanced gas turbine blades. As depicted in the cutaway of Fig.1.2, a succession of rib turbulators are installed on the internally cooled turbine airfoil. When the cooling passages are roughened with ribs, heat transfer to the cooling air within the blade is significantly enhanced. The geometries involved in this application differ from the previous one (as do the boundary conditions at the walls) but, from the conceptual point of view, the heat transfer augmentation is provoked by the same physical phenomenon, that is the vortex generation and high turbulence levels which improve the heat exchange from the walls.

Artificially roughening internal/external surfaces of pipes and channels is also a common practice in heat exchanger design. Compact heat exchangers, for instance, require high heat transfer surface areas (and high heat transfer coefficients) concentrated in a small heat exchanger volume. Hence, any solution (adding ribs, for instance) which increases heat transfer is welcome here. Figures 1.3 (a) and (b) show externally finned pipes and internally rib-roughened passages, respectively. The use of these surfaces ranges from the automotive industry to control systems in aircraft vehicles.

So far forced convection heat-transfer applications have been presented. Natural convection flows are of interest in a number of engineering applications. In spite of lower heat transfer coefficients as

compared with those in forced convection, natural convection heat transfer is an attractive mechanism (for low-density energy production systems) owing to its reliability, simplicity and cost effectiveness. In some applications (cooling of electronic devices for telecommunications) it is even the *only* feasible way of removing the heat produced as the use of fans can disturb the correct working of the equipment.

A different approach to the study of heat transfer enhancement problems in free convection is generally required. In fact, in a forced convection problem, the heat transfer augmentation provided by the enhanced system (with respect to a reference unaugmented system) under given constraints (at fixed mass flow rate, for instance) occurs at the price of higher pressure drop and pumping power. Since the mass flow rate is controlled independently of the thermal problem, the penalty of higher costs to pump the fluid can be accepted if the heat flux exchange is the major task. In a natural convection system no energy costs are needed to pump a given mass flow rate. In fact, if a system operates in a natural convection situation, the flow rate is not externally controlled but derived from a balance between the buoyancy and the friction forces. Thus, higher friction, occurring for instance when a flat surface is artificially roughened, leads to a lower flow rate which tends to reduce heat transfer. Conversely, the augmented heat transfer surface area as well as the modified local heat transfer characteristics (for example vortex generation or fluid recirculation) generally cause an increase in heat transfer which may or may not counterbalance the negative effect related to the reduction in mass flow rate. Therefore, it is not possible to establish " a priori" if a rib-roughened surface, which represents a forced convection enhanced system, could be regarded as an enhanced system in natural convection.

Three examples of possible enhanced surfaces in free convection are shown in Fig.1.4 (Fujii et al.,1973). The external surface of a cylinder, cooled by a liquid in natural convection, is roughened using repeated ribs (Fig.1.4 a), dispersed-protrusion elements (Fig.1.4 b), and dense-pyramid elements (Fig.1.4 c). Increases in the average heat transfer coefficients in the range 0-10% were observed relative to data for a smooth cylinder. In spite of this result (and others obtained for similar configurations), the literature seems somewhat contradictory with some researchers finding increases of 100% and others finding no increases and even decreases (Bhavnani and Bergles, 1990). If it is indeed possible to enhance heat

transfer, then it is important to understand how various surface modifications (for instance a vertical rib-roughened surface or channel) produce this enhancement.

1.2 Thermal control

Understanding the thermal performance of systems on which the roughness is present naturally is of great importance when the main concern is the thermal control of the surface. Electronic equipment packages represent an industrial situation in which convective heat transfer in roughened channels is encountered. In current designs of low-power-rated electronic components on printed circuit boards, specific consideration is given to heat transfer analysis to achieve high heat dissipation rates and to limit peak temperature levels. Currently, low Reynolds number forced convection and natural convection heat transfer are useful to guarantee the appropriate working temperature of components. In most of the recent literature, the circuit board is simulated by an array of heated square blocks deployed along a wall of a parallel-plate channel, as depicted in Fig. 1.5 (Faghri and Asako, 1994). The problem has been investigated numerically (even by three-dimensional analysis but in the laminar regime) and experimentally (using a two-dimensional test section). Natural convection cooling of electronic equipment continues to be an important thermal control mechanism in applications such as telecommunications electronics, in which long term reliability is an overriding design criterion, and consumer electronics in which acoustic noise is undesirable. In typical "passive" cooling applications (i.e. free convection cooled), densely packed boards are vertically oriented in order to promote the most effective buoyancy flow condition (Fig. 1.6, Choi and Ortega, 1993).

Other applications of studies on free convection from arrays of heated roughness elements include the design of solar collectors, fluid-filled thermal storage tanks, operation and safety of nuclear reactors, and fire prevention and safety.

1.3 Why use optical methods in experiments on rib-roughened channels?

The applications mentioned in the previous paragraphs demonstrate the usefulness of the investigation of forced/natural convection heat transfer

in rib-roughened channels. Owing to the complexity of the geometry, the ability to predict analytically and numerically the effect of the ribs on the flow field and heat transfer is limited. Therefore, experimental investigation is the most reliable and effective approach to verify the influence of the relevant geometrical parameters on heat transfer and friction characteristics. In this connection *optical methods* represent an extremely versatile tool for making quantitative measurements of thermal phenomena. In complex flow situations, such as those encountered in convection from ribbed surfaces, the use of traditional sensors (thermocouples, for instance) does not permit whole-field information to be obtained on the observed phenomenon (unless the displacement of a very large number of miniaturised sensors in the test section is provided) and may alter flow and thermal characteristics owing to the physical presence of the probes. These disadvantages are efficiently overcome by optical methods, which allow a non-intrusive analysis over the whole optical field. A large variety of optical methods is currently employed in experimental investigations of complex flows. Most of them are based on physical principles known since the last century. Their use has mainly been qualitative for several years. The recent development and wide-spread availability of inexpensive video digitisers combined with the increased power of computers has made routine digital image analysis feasible. It means that, if the relationship between the optical parameters recorded and the temperature (or the temperature gradient) is well established, the digitised optical field can be, in real time, processed and converted in the thermal field, or, alternatively, the thermal parameters of interest, such as local heat transfer coefficients, can be easily extracted.

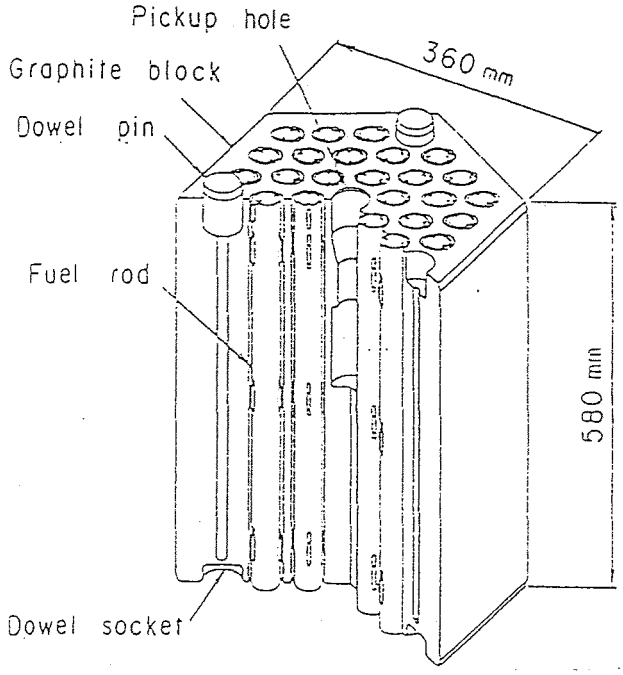

FIGURE 1.1. A fuel element with 33 standard fuel rods in High Temperature Test Reactor.

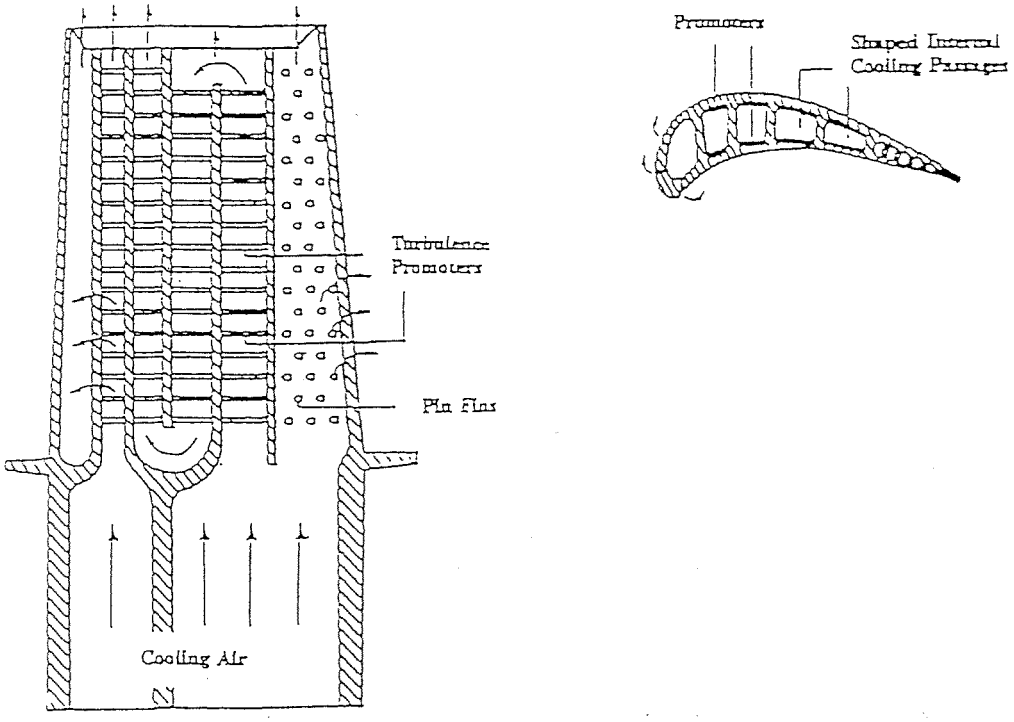

FIGURE 1.2. Cutaway view of an advanced gas turbine blade.

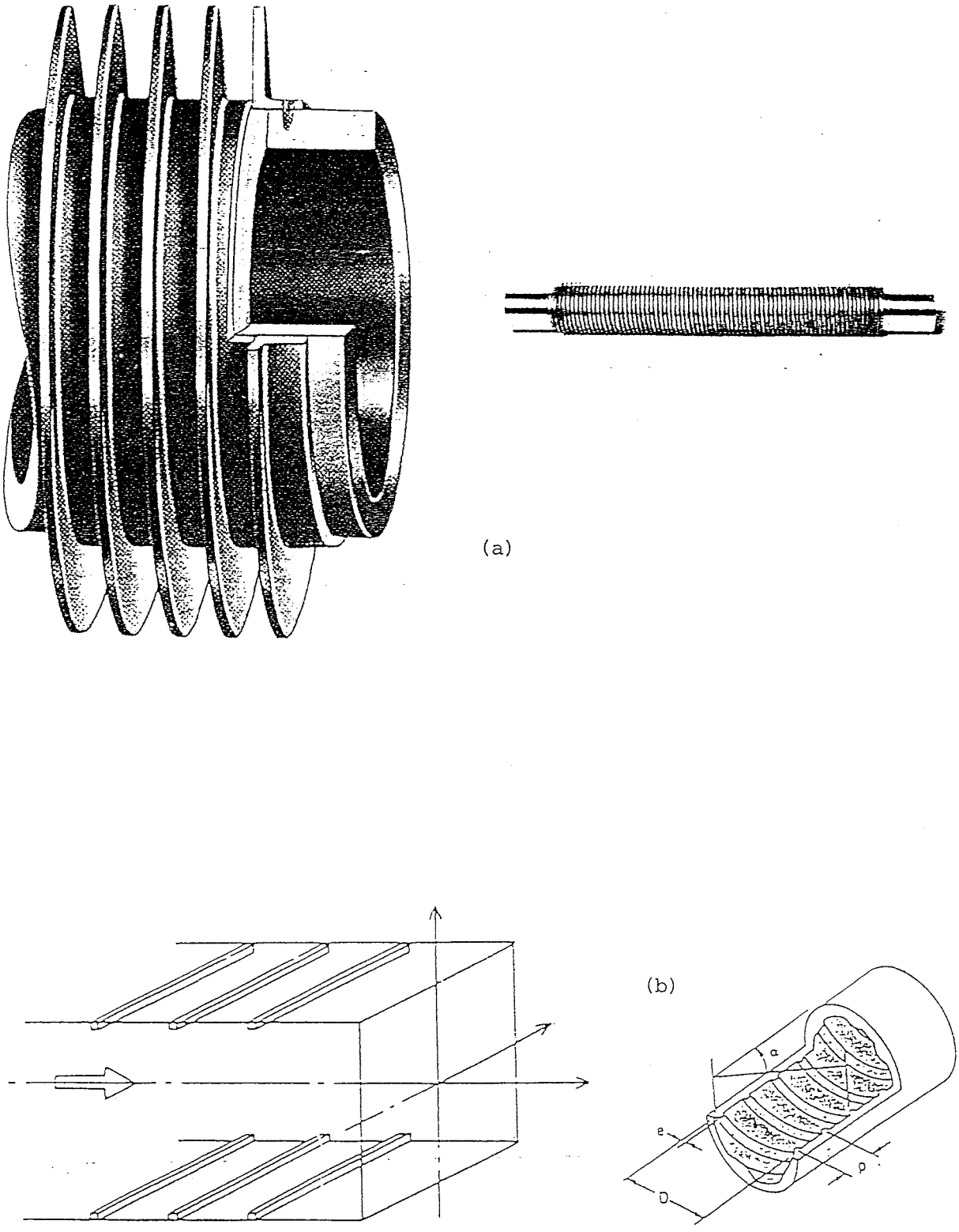

FIGURE 1.3. (a) Externally finned tubes and (b) internally roughened passages commonly used in heat exchangers.

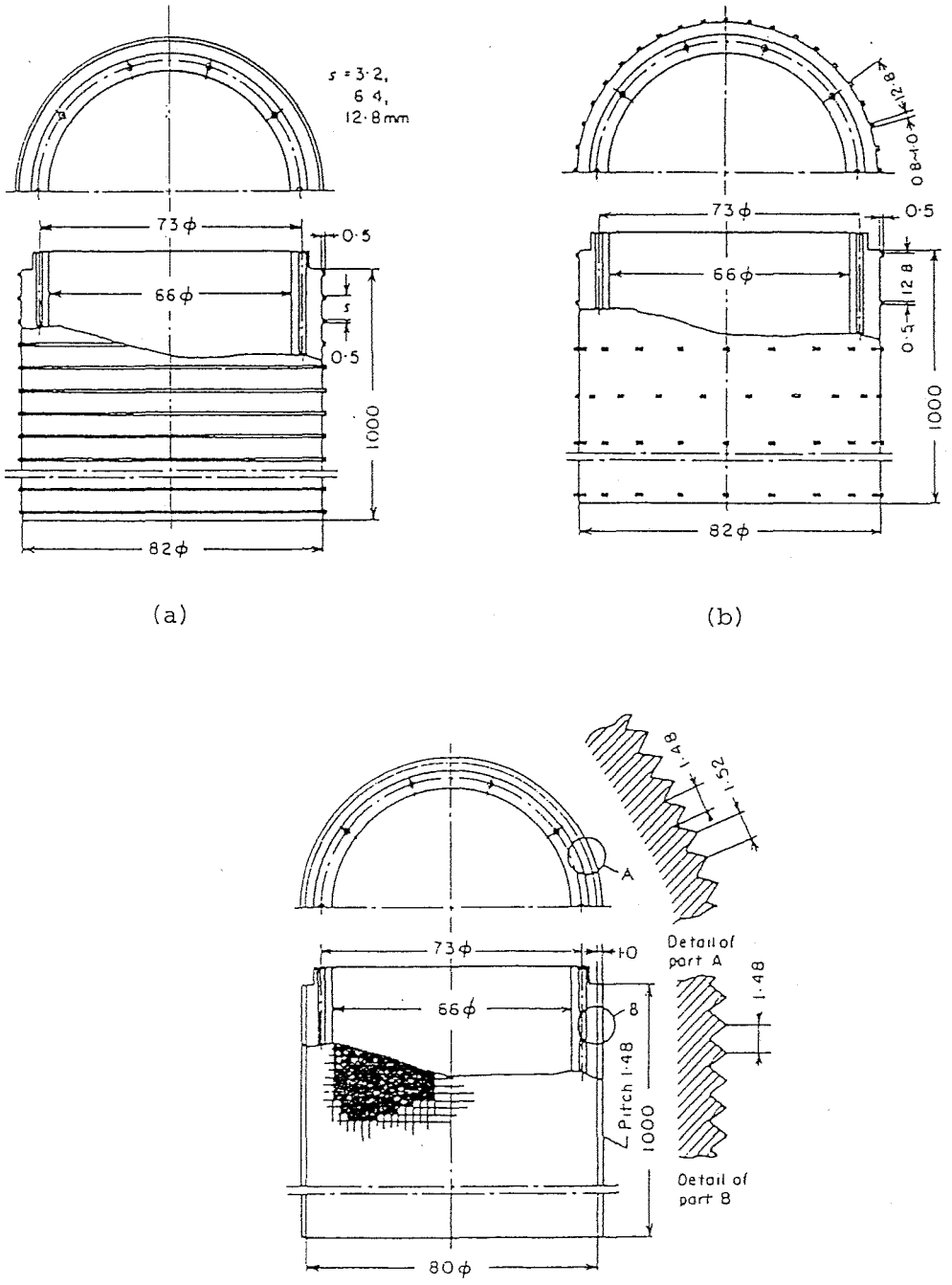

FIGURE 1.4. External surface of a vertical cylinder roughened by (a) repeated ribs, (b) dispersed-protrusion elements, (c) dense-pyramid elements.

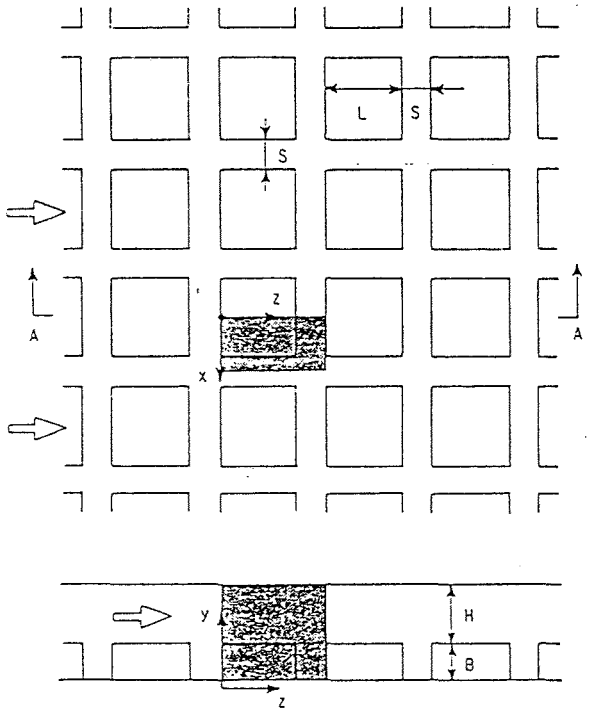

FIGURE 1.5. Schematic diagram of array of rectangular modules along a flat plate simulating a circuit board.

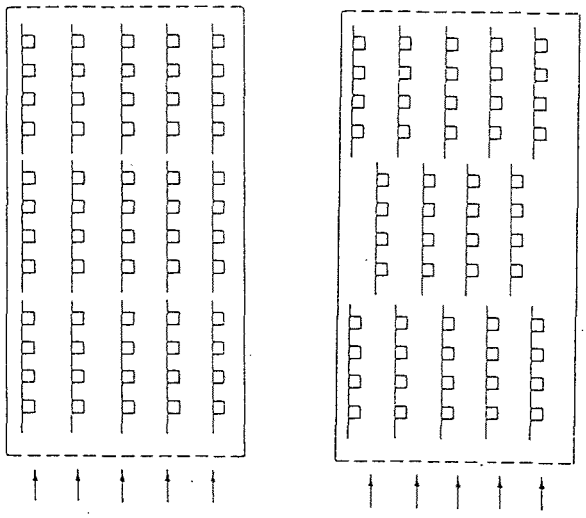

FIGURE 1.6. Printed circuit board in a cabinet: packaging alternatives.

CHAPTER 2. LITERATURE SURVEY

A considerable number of flow and heat transfer studies in rib-roughened channels is documented in the technical and scientific literature. A general review of the wide bibliography dealing with heat transfer from roughened surfaces could be organised according to different criteria: the chronological order, the approach followed in the study (theoretical, numerical, or experimental), the application, and so on. In addition, as stated in the previous Chapter, artificially roughened surfaces can be encountered in applications involving flows in either forced or natural convection. Therefore, a subdivision of published papers based on *the nature of the convective flow* was deemed to be the most appropriate choice. Even though similitudes and connections between forced and natural flows on ribbed surfaces are present, the nature of flow (forced or natural) affects the extent of heat exchange, the distribution of heat transfer coefficients and the features of the experimental apparatus. For example, the experimental study of forced convection requires wind tunnels, heaters able to supply large quantities of power to the fluid, flow rate and pressure instrumentation devices and other equipment. The experimental study of natural convection generally requires less demanding equipment but it has to be performed in a laboratory with high thermal stability and isolated from external disturbances (without external walls, vents and thermal sources).

The consideration that this project consists of two separate experimental parts which differ owing to the nature of the air flow (and to the different optical method employed) is a further reason to support the classification of the references in the two following groups:

2.1 Forced convection from rib-roughened surfaces;
2.2 Natural convection from rib-roughened surfaces.

A third section 2.3 will contain a brief review of optical techniques suitable for convective heat transfer investigations, with specific interest for methods employed and developed here (liquid crystal and schlieren methods).

2.1 Forced convection from rib-roughened surfaces

A large number of papers have been published on this subject and only

a selection of them will be discussed and quoted in the list of references. The majority of studies involve experimental investigations of two-dimensional geometries. Also, numerical analyses have been developed in the last decade, both for the laminar and turbulent flow regimes.

2.1.1 Historical background and state-of-the-art

The effects of surface roughness on flow and heat transfer characteristics have been investigated since the first decades of this century. While initial studies were inspired by the need to clarify phenomenological aspects of the problem, specific applications (heat transfer enhancement in gas-cooled nuclear reactors) necessitated the performance of experiments in annular passages. The majority of experiments conducted in the 50's and 60's were developed in annuli with heated roughened inner and unheated smooth outer surfaces, thus simulating as closely as possible conditions occurring in the cooling of fuel element rods. Alternatively, rectangular channels with the ribbed plate heated and the other (smooth) plates unheated were considered.

The main challenge faced in those years concerned the most convenient format of presentation of the large quantity of experimental data obtained. Since the characteristics of the roughened surface were of primary interest, different methods were proposed to separate the properties of the two surfaces forming the annulus (or the channel). The first method developed was called the "Hall transformation" (Hall, 1958). This method assumes that the surface of zero shear stress is a boundary within which the structure of the turbulence is unaffected by changes in the structure occurring beyond the surface. For instance, in a channel formed by two infinite flat plates, one rough and one smooth (Fig.2.1 (a)), the flow between the region of the rough surface and the plane of zero shear stress would be unaffected if the smooth plate were removed and replaced by an identical rough plate but at the same distance as the first rough plate is from the plane of zero shear stress (Fig.2.1 (b)). Further assumptions are that the surface of zero shear stress coincides with the surface of maximum velocity (y_m) and that the use of the equivalent diameter defined by the flow area between the roughened surface and the surface of maximum velocity accounts for a change in passage shape so that results apply to a roughened circular pipe, for example. Measurements of velocity and temperature profiles in the passage allow mass flow rate and equivalent diameter to be calculated for the rough zone; therefore, transformed friction factor and

Reynolds number can be calculated for the roughness region only. Similarly, assuming that the line of zero shear stress and the adiabatic line are coincident, it is possible to calculate transformed heat transfer coefficients (generally recast in dimensionless form, Nusselt or Stanton numbers) for the roughened region from temperature distribution data.

Unfortunately the measurement of velocity and temperature profiles in the passage, required to localise the maximum velocity line, is demanding and time-consuming in most experimental situations. Therefore Wilkie (1966) proposed a simplified method which does not require velocity (and temperature) profile measurements. From detailed local measurements in different annuli he evaluated the average velocities w_r and w_s in the two regions (rough and smooth, respectively) of the annulus (separated by the maximum velocity criterion) and the (transformed) friction factor f_r of the inner rough surface. He found that the ratio w_r/w_s depends on the ratio f_r/f_{r0} (f_{r0} being the friction factor of a smooth pipe at the same transformed Reynolds number, assumed to be $0.046\ Re_r^{-0.2}$) only when f_r/f_{r0} is lower than two (Fig.2.2). When f_r/f_{r0} is larger than two, the two average velocities w_r and w_s are equal within 2 percent. Therefore, the assumption $w_s=w_r=w$ (w being obtained from the measured mass flow rate) can be made. The (transformed) equivalent diameters of rough and smooth regions d_s and d_r and the friction factor f_r of the rough surface can be derived from the solution of the following set of equations:

$$w_s=w_r=w \tag{2.1a}$$

$$d_s=4A_s/\Gamma_s \tag{2.1b}$$

$$d_r=4A_r/\Gamma_r \tag{2.1c}$$

$$A = A_s+A_r \tag{2.1d}$$

$$\Delta P/L=f_r(4/d_r)(1/2\rho w_r^2) \tag{2.1e}$$

$$\Delta P/L=f_{s0}(4/d_s)(1/2\rho w_s^2) \tag{2.1f}$$

$$f_{s0} = 0.046\ Re_s^{-0.2} \tag{2.1g}$$

where A is the annulus flow area, A_r is the flow area between the rough surface and the plane of maximum velocity, and A_s is the flow area between the plane of maximum velocity and the smooth surface. Γ_r and Γ_s represent the (known) perimeters of the rough and smooth surfaces, respectively, while $\Delta P/L$ is the measured pressure drop along the annulus length L. In Eq.(2.1g), Re_s is based on w_s and on the unknown equivalent diameter d_s. Results from rectangular and annular channels showed that the transformed friction factor of a smooth surface was increased when facing a

progressively rougher surface, this being in contrast to the concept of the separation line between smooth and rough zones. Wilkie took into account the departure of transformed smooth friction factor f_s from f_{s0} (=0.046 Re_s^{-2}) by introducing in his simplified transformation method a further empirical relationship between (f_s/f_{s0}) and (f_r/f_{r0}).

The partial failure of the Hall transformation method lies in the fact that in annuli with strongly asymmetric velocity profiles there is no coincidence between the lines of zero shear stress and of maximum velocity, the position of no shear being shifted towards the outer smooth surface (Kjellstrom and Hedberg, 1966). Therefore a different method was proposed by Maubach (1969, 1972) known as the "Maubach transformation". This method is based on the existence of dimensionless velocity profiles obeying "the law of the wall":

$$w_s^+ = A_s \ln y^+ + B \qquad (2.2a)$$

$$w_r^+ = A_r \ln(y/e) + R \qquad (2.2b)$$

where w^+ stands for the local streamwise velocity normalised by the friction velocity $(\tau_w/\rho)^{1/2}$. The slopes A_r and A_s are generally taken to be the same and equal to 2.5. The parameters B and R can be determined by experimental results. In order to separate the two zones in asymmetrical flows Maubach assumed that the zero shear stress line is given by the intersection of the two velocity profiles originating at the respective walls. A good agreement with the experimentally determined line was found. Once the separation line has been obtained, integration of equations for w_s^+ and w_r^+ over the respective flow areas yields the relevant friction factors and Reynolds numbers. Further modifications to this method were proposed by Dalle Donne and Meerwald (1970), Warburton and Pirie (1973), Dalle Donne (1976) and Dalle Donne and Meyer (1977).

In spite of the different ways of recasting data, the proposed transformation methods are valid from an engineering standpoint and distinctions between data transformed by the Hall or Maubach methods can be generally neglected.

Once the different methods of interpretation of experimental results are clarified, it should be pointed out that further discrepancies appeared in the results of various investigators even when analysed by the same transformation method. This is due to the frequently poor definition of the roughness being studied (that often makes a comparison among data

unfeasible), to the different geometric conditions (for example annuli with different radius ratios, rectangular channels, parallel plates), and to the different quality of the experimental approaches. The problem is complicated by the large number of parameters involved. Therefore, the validity of results proposed by each author is limited to the parameter ranges indicated and the poor agreement between data obtained in similar conditions makes it difficult to generalise the effect that a specific parameter is expected to have on friction and heat transfer characteristics.

The first attempt to correlate heat transfer results obtained in annuli (with heated roughened inner and unheated smooth outer surfaces) was conducted by Gomelauri (1964). The proposed relationship is based on data obtained by Nunner (1956), Fedynsky (1959), Brauer (1961) and Gomelauri (1964) and expresses the Nusselt number as a function of the untransformed Reynolds number (based on the equivalent diameter of the annulus):

$$Nu_f = 0.0218\ Re_f^{0.8} Pr_f^{0.4} (Pr_f/Pr_w) \exp(f_n(P/e)) \qquad (2.3)$$

where the subscripts f and w refer to properties evaluated at the film temperature (average between wall and bulk temperatures) and at the wall temperature, respectively. Further:

$f_n(P/e) = 0.85\ (P/e)_{opt}/(P/e)$ when $P/e \geq (P/e)_{opt}$

$f_n(P/e) = 0.85\ (P/e)/(P/e)_{opt}$ when $P/e \leq (P/e)_{opt}$

$(P/e)_{opt}=13$; $6\times10^3<Re<90\times10^3$; $1<Pr<80$.

Since the relationship (2.3) correlates data obtained for square, triangular and rounded roughness elements, it is expected to be somewhat roughly approximated, even if adequate for engineering calculations.

One of the most important and exhaustive studies on the effects of the geometrical parameters on friction and heat transfer characteristics was performed by Wilkie (1966, a). He collected heat transfer and pressure drop data from annuli with heated roughened inner and unheated smooth outer surfaces (Fig.2.3) interpreted by means of the Hall transformation. Effects of geometric parameters P/e and e/d (the latter not evidenced by Gomelauri) as well as of the transformed Reynolds number Re were discerned. According to the Hall transformation, the equivalent diameter d is defined as $4A/\Gamma$ where A is the flow area between the rough surface and the maximum velocity surface (at the distance y_m) and Γ is the perimeter of the wall surface only, the perimeter of the surface of maximum velocity being excluded. Rib

height e varied from 0.1 to 1.6 % of the equivalent diameter d of the annular passage and the rib pitch to height ratio P/e from 2.5 to 50. Further experiments (without heating) were conducted for rib-width to rib-height ratio w/e from 0.5 to 2.5. The following main conclusions were reached:

(i) friction factor is independent of Re at high Re and e/d as shown in Fig.2.4;

(ii) the variation of St number (St=Nu/RePr) with Re depends on e/d; as emerges from inspection of Fig.2.5, small e/d exhibit less variation than large e/d, the latter showing the same variation as smooth surfaces;

(iii) the friction coefficients and the St numbers for the rough surfaces, normalised by the relevant values for a smooth inner surface and plotted against P/e (Figs 2.6 and 2.7, respectively) show a maximum. The P/e value giving maximum friction and maximum Stanton number varies with e/d (the lower the e/d, the higher the P/e) and it is almost independent of Re (in the range $Re=1-3x10^5$). The two maxima are obtained for P/e=6 at large e/d and for P/e=6-8 when e/d=0.01-0.016. Reducing e/d implies a larger P/e value ($=(P/e)_{opt}$) to achieve the best relative heat transfer performance (Fig.2.8); this information is crucial for the correct design of annular passages with internal rough surfaces. Since Gomelauri (1964) did not consider e/d as an independent variable (its effect is diluted in his definition of Re), direct comparison between $(P/e)_{opt}$ obtained by Wilkie (Fig.2.8) and Gomelauri (=13) is not feasible.

Finally, Wilkie investigated the effect of w/e for a limited number of experiments (at constant P/e and e/d). Strong reductions in friction can be achieved by increasing the rib width to height ratio (Fig. 2.9); no heat transfer data were obtained in these conditions.

The effect of the roughness shape was investigated by Williams and Watts (1970). Ribs having square, chamfered and wedge profiles were tested in a rectangular channel. In order to gain a better understanding of the reasons for the differences found among the three types of rough surface, flow visualisations were carried out, using small polystyrene particles dispersed in the water flow. The picture which emerged from this investigation is essentially a sequence of vortices starting, growing, and then moving downstream as in Fig.2.10 for (untransformed) $Re=1.7x10^5$, P/e=7. Visualisations showed that reducing the pitch to height ratio P/e for square ribs from 7 to 3 leads to the formation of a standing vortex

between the ribs occupying approximately two thirds of the cavity. This explains the noticeable reductions in heat transfer performance found by Wilkie (Fig.2.7). In addition, local heat transfer coefficients at P/e=7 and 3 were evaluated, by a mass transfer analogy technique, for square, chamfered, and wedge ribs (Fig.2.11 (a) and (b)).

Interest in local flow and heat transfer characteristics was progressively becoming the main concern of investigations in view of the availability of considerable global flow and heat transfer information. Local velocity and pressure profiles obtained by Aytekin and Berger (1979) and Meyer (1980) led to quantitative assessments of the mainstream reattachment length (Fig.2.12) and to a refined dimensionless velocity distribution in the rough zone without the assumption of a constant profile slope (Fig.2.13) . A further contribution to the local heat transfer analysis in systems simulating fuel element cooling in Advanced Gas-cooled Reactor (AGR) was given by Lockett and Collins (1990). Their experimental local heat transfer coefficients were obtained by means of an interferometric analysis applied to square and rounded rib-roughness elements. For square ribs (Fig.2.14), local coefficients on the forward facing rib wall were found to increase from the base to the tip of the rib. On the rib top, Nu generally decreases far from the leading edge, with strong reductions on the rear facing rib wall. In the inter-rib region, the Nu number has an initial peak downstream of the reattachment point. The growth of the boundary layer after the reattachment is responsible for the subsequent decrease. A second peak in the Nu distribution was observed very close to the trailing rib corresponding to the reattachment point of the secondary recirculation in the corner between the inter-rib space and the forward facing rib wall. Recently, Aliaga et al. (1994) performed accurate local heat transfer measurements and flow visualisations for the same geometry (a heated plate with square ribs opposed to an adiabatic plate) including the fully developed region as well as the entrance region, as shown in Figs. 2.15. Even though results refer to a small range of Reynolds number ($1.0\text{-}1.5\ 10^6$), they are useful in clarifying the complex interactions between the flow field features and the local heat transfer performance. It was found that for the smaller pitch-to-height ratio a single recirculation bubble is formed in the cavity between consecutive ribs and heat transfer is impaired. For the larger P/e value, however, the effect of the ribs seems to be excessively diluted, with a clear heat

transfer decrease between the reattachment and the (second) separation points (Fig.2.16). Finally, different heat transfer coefficient profiles were identified around the first three ribs owing to possible flow distributions (Fig.2.17).

Since the 1970's, the demand for increasing thermal efficiency in numerous engineering sectors (heat exchanger design and turbomachinery, for example) has promoted great efforts in the development of heat transfer enhancement techniques. As a consequence, the traditional annular geometry (with one heated rough surface and the opposite unheated smooth surface), simulating a typical nuclear reactor situation, was progressively abandoned in favour of more complex geometries. These involved two or three dimensional channels roughened on one or more sides with ribs of different shape and inclination.

Webb et al. (1971) were among the first to develop a generalised understanding of the friction and Stanton number characteristics of "repeated-rib" roughness in turbulent pipe flow. The study provided correlations for f and St for e/d (d being the "transformed" equivalent diameter) between 0.01-0.04 and P/e between 10 and 40, in addition to drawings of flow patterns as a function of P/e (Fig.2.18).

Han et al. (1978) considered a geometry consisting of two parallel plates roughened by symmetric and staggered ribs. Results were presented without a transformation for data reduction. In the ranges of parameters investigated, the Stanton number is maximised for P/e = 10, which is not too far from values suggested by Wilkie for an annular passage asymmetrically heated. Some years later, Han (1984) extended the analysis to square ducts with two opposite rib-roughened walls (Fig.2.19), addressing his study specifically to turbine blade internal cooling design.

The combined effect of the rib-angle-of-attack and the channel aspect ratio on the distributions of the local heat transfer coefficient for developing flow in rectangular channels with opposite rib-roughened walls was determined by Han and Park (1988). Owing to the entrance effect, for a square channel roughened by ribs with angle-of-attack normal to the main flow, the (periodic) Nusselt number decreases in the streamwise direction and then reaches a constant periodic distribution after three times the hydraulic diameter of the channel (Fig.2.20). Some modifications are induced by a different angle-of-attack in square and rectangular channels. The best heat transfer performance (as compared with that for a smooth

channel at the same Re) were obtained for the square channel with ribs at an angle-of-attack α=60°; this is apparent from inspection of Fig. 2.21.

Several experimental contributions are reported in the literature of the 1980's and 1990's. The majority of papers are aimed at the specific application of turbine blade cooling and therefore the ribbed passage under study is subject to further modifications in order to represent as closely as possible the application. For instance, a rotating serpentine passage with rib-roughened surfaces was studied by Fann et al. 1994.

So far, most of the relevant experimental work dealing with flow and heat transfer characteristics for rib-roughened surfaces has been mentioned. It is apparent that the geometries investigated were strictly related to the specific applications: asymmetrically heated annular passages for nuclear reactor cooling problems (from the 1950's to the present day), square and rectangular channels with different conditions of heating and roughness at the walls for turbomachinery, heat exchangers and electronic equipment cooling problems (in the last two decades). Owing to the complexity of flow features in channels with rough walls, only in a few studies has the problem been tackled analytically or numerically. The first attempt to determine analytically the roughness functions for flow over rectangular ribs was made by Lewis (1975). The flow was approximated by a series of attached and separated flow regions, and some empirical information from experiments over cavities and steps was required. One of the first numerical analyses for forced convection heat transfer from rib-roughened surfaces was conducted by Rowley and Patankar (1984). The geometry investigated was a tube with internal circumferential fins cooled by a laminar flow of fluid at different Prandtl numbers (Fig.2.22). It was found that the ribs do not always increase heat transfer in the laminar regime. Despite the increased area provided by the ribs, the distortion of the flow that the ribs cause (with weak recirculating motion between adjacent ribs, Fig.2.23) can substantially diminish the heat transfer from the duct wall and thus lower the overall heat transfer. In particular, for a Prandtl number typical for air (Pr=0.7), a reduction in heat transfer was *always* obtained (Fig.2.24).

The numerical study of turbulent convective flow in rib-roughened channels implies a higher degree of complexity of the problem, owing to the four-dimensional (three spatial, one time, coordinates) character of turbulence. Most of the computational results obtained in the turbulent

flow regime were based on the k-ε turbulence model (Wilkes, 1980, Fodemski and Collins, 1988, Lee et al.,1988, Takase et al.,1994 among others). More recently LES (Large-Eddy Simulation) results have been obtained for turbulent flow and heat transfer in a plane channel with transverse square ribs on one side (Ciofalo and Collins, 1992). Local heat transfer results, compared with k-ε predictions and experimental data, presented many features in agreement with experimental data not evidenced by k-ε simulations. For instance, the second Nu maximum in the reattachment region was predicted, as shown in Fig.2.25.

2.1.2 Experimental techniques

This project is mainly based on an experimental programme dealing with heat transfer from rib-roughened channels. Therefore, in the literature review, particular attention is given to the experimental techniques developed to obtain heat transfer data. As discussed in the previous paragraph, at first the main concern was overall heat transfer performance in annular passages. Typically, heat transfer experiments were conducted using a cylindrical electric heater located inside the inner, rib-roughened tube, while the outer smooth tube was thermally insulated. The test section included a very large number of repeated ribs in order to gain fully developed flow and heat transfer conditions. Because of the thermal conductivity of the inner tube material, the temperature tended, in these systems, to attain a nearly uniform profile along the surface (with small increases from the entrance to the exit) in spite of the uniform heat flux dissipated by the heater. Therefore the thermal boundary condition at the heated wall was often somewhere between uniform heat flux and uniform temperature conditions. Thermocouples were generally deployed in small holes drilled in the inner (rough) tube at several locations (to record the mean heated wall temperature T_w) and in the inlet/outlet sections (to record a mean coolant temperature T_f). Since the dissipated heat flux (by Joule effect) could be easily measured, the mean heat transfer coefficient h at the inner rough surface is derived from the simple relationship

$$h = Q / [A (T_w - T_f)] \qquad (2.4)$$

where A is the heat transfer surface area and Q is the electric heat flux corrected to take into account radiation heat exchanges and conduction heat losses.

This kind of experimental approach could be unsuitable for local heat

transfer observations. In fact, if the local heat transfer coefficient is required, the above relationship needs to be applied on a local basis. Since the wall temperature or the specific heat flux to the fluid may change from point to point (as well as the local bulk temperature of the fluid), care must be taken to ensure well-defined thermal boundary conditions and to make measurements of the surface temperature in detail (that is in a large number of spots). This is shown, for instance, in Fig.2.26 (Hong and Hsieh, 1993). The manufacture of a similar test section is time-consuming and expensive. In addition, many measurements need to be performed and processed in order to reconstruct local heat transfer coefficients limited to a discrete number of locations, namely those monitored by thermocouples. To overcome these fundamental difficulties, methods based on the heat/mass transfer analogy and optical techniques were successfully applied to the study of rib-roughness geometries. A description of methods employed as alternatives to thermocouples measurements is given in detail. Comparisons of results obtained by some of the above-mentioned methods will be presented in section 3.4.3.

(a) Thin film naphthalene.

The similarity between the mechanism of heat and mass transfer can be used to evaluate heat transfer coefficients. If the surface is covered by a uniform thickness of a volatile substance (for instance naphthalene), the local thickness variation after a predetermined period of flow exposure indicates the mass transfer (equivalent to the heat transfer) from the wall to the fluid. No heating of the test section is required. Kattchee and Mackiewicz (1963) performed experiments for rib-roughened surfaces with P/e =7 and 8.5. Sparrow and Tao (1983) used this technique to study local heat transfer from a wall with rod-type disturbance elements oriented transverse to the flow direction. The correct application of this technique requires extra care in the naphthalene deposit, which must have a uniform thickness; this operation may be time-consuming and expensive, particularly for complex surface geometries.

(b) Evaporation from water absorbent paper.

The heat/mass transfer analogy can also be applied by covering the surface with a layer of absorbent paper previously impregnated with a solution of cobaltous chloride. At the start of each test, the surface is sprayed evenly with water. After this treatment, the test assembly exhibits

a bright pink colour. The time interval between the start of the flow and the colour change (from pink to blue) is proportional to the local heat transfer coefficient. This technique was developed and applied to rib-roughened surfaces (P/e=7) by Williams and Watts (1970).

(c) Electrochemical analogue technique.

The transfer rate of certain ions in aqueous solutions to an electrode is proportional to the local heat transfer rate. An aqueous solution of potassium ferri- and ferrocyanide with sodium hydroxide as the inert electrolyte was used by Berger and Hau (1979). A strip of nickel was used as the anode and a ribbed surface of nickel as cathode. The measurement of the electric current at certain stations around the surface enables the heat transfer coefficient distribution to be determined.

(d) Copper foil technique.

This method involves the use of a series of copper strips placed on a ribbed surface. If the dependence of electrical resistance on the temperature of the strips is known, then ranges of known electric power may be dissipated into the strips, giving uniform heat flux over the ribbed surface. Then the readings of the voltage drop and current across each strip allow the heat transfer coefficients (averaged on each strip) to be determined. If numerous thin strips are fitted onto the ribbed surface, the local heat transfer coefficient distribution can be extracted (Watts and Williams, 1981).

(e) Holographic interferometry.

The above mentioned techniques present several inconveniences: poor resolution, uneasy machining of the test section, availability of relative and not absolute results (a,b,c methods), no information on the flow field. Holographic interferometry (as well as classical interferometry from which the former represents an evolution) provides a method which is optical, non-invasive and whole-field in character, and can investigate thermal effects. This technique was applied to the study of forced convection from rib-roughened surfaces by Walklate (1983), Lockett and Collins (1990), and Liou and Hwang (1993).

(f) Thermographic methods.

Owing to the recent developments in image processing as well as software and computer capabilities, thermographic methods have gained

recognition as appropriate research tools in the evaluation of heat transfer performance of complex geometries. Infrared thermography was used by Aliaga et al. (1994) to determine heat transfer coefficients along a surface with a series of repeated square transverse ribs. In particular, infrared thermography gave the local wall temperature for a known wall emissivity, while local heat flux was measured as a difference between the electrical power and conductive/radiant calculated losses. As an alternative to infrared thermography, which involves the use of expensive devices and extra care in the operating procedure, thermochromic liquid crystals can be used. Liquid crystal thermography enables the wall temperature pattern to be obtained and then the heat transfer coefficient distribution to be reconstructed. Liquid crystals, deposited on thin sheets directly attached to the ribbed surface, need only to be illuminated by non-coherent light under suitable conditions. The reflected image, which contains a colour pattern related to the wall temperature field, is recorded by a camera, and then digitised and processed even in real time. No systematic experiments using liquid crystals on rib-roughened surfaces are reported in the literature. The present report will show the ability of liquid crystal thermography to obtain detailed distributions of heat transfer coefficient on complex surfaces involving the placing of ribs in both transverse and normal directions to the flow.

2.1.3 Future developments and areas of research

For roughened surfaces with transverse square ribs the effects of the rib height, the rib pitch and the channel equivalent diameter on the fully developed average heat transfer and friction factor are well established over a wide range of Reynolds number. Modifications to the basic rough geometry have been introduced, by considering an angle of attack different from 90° (inclined ribs instead of transverse) and different shapes of ribs (rectangular, chamfered, wedged and rounded); heat transfer performance improved in some cases.

The majority of experiments have shown that the poorest heat transfer regions occurred downstream of the ribs, where a recirculation zone is formed. Conversely, heat transfer coefficients are high after the reattachment length and along the forward facing rib wall (for the fluid impingement) and the rib top. Therefore, one possibility of improving heat transfer conditions is to create more turbulence particularly in the less active inter-rib region. Adding a groove between two adjacent ribs reduces

the reattachment length and generates higher levels of turbulence with higher heat transfer coefficients. Also a higher heat transfer surface area results. This concept is illustrated in Fig. 2.27 (Zhang et al.,1994). Corresponding St numbers, as compared with ribbed surfaces without grooves are shown in Fig. 2.28.

Another important consideration involves the local velocity distribution generally occurring in channels roughened only on one wall (the others being smooth). As documented in several references, the maximum velocity occurs close to the smooth wall. This means that only a fraction of the cooling flow rate actively contributes to the removal of heat from the rough wall. The installation of turbulence promotors placed in front of the rough wall or mounted on the opposite smooth wall may increase the turbulence level and drive the flow towards the heated surfaces in a more effective way. This generally occurs at the price of a higher pressure drop. Two interesting examples are presented in the literature, given by Hung and Lin (1992), and Myrum et al. (1993). Figures 2.29 (a) and (b) show the type of turbulence promotor adopted. While Hung and Lin found larger heat transfer enhancements with decreasing P/e ratio (in the range 2.5-10), Myrum et al. (1963) found that their generators had a larger impact on the heat transfer performance for the higher P/e value explored (P/e=38.4) rather than the smaller (P/e=19.2). Recently, Zhu et al. (1995) have numerically studied, using the k-ε turbulence model, three-dimensional turbulent flow and heat transfer in a channel with longitudinal vortex generators on one wall (rectangular winglets) and rib-roughness elements on the other wall (Fig.2.30). The comparison with data for a channel with an adiabatic wall and an isothermal wall without winglets and ribs showed that the combination of ribs and winglets produces more than 450% heat transfer enhancement.

In spite of the large quantity of papers dealing with rib-roughened heat transfer surfaces, the author is not aware of any work which has been published on flow and heat transfer in channels where the rib-roughened surface is not the heat transfer surface but only acts as a vortex generator to increase flow turbulence in the channel. It is well known that an obstacle mounted on a flat plate cooled by forced convection can increase heat transfer from the plate. In fact, the formation of complex secondary flows downstream of the obstacle ("horseshoe vortex", Fig.2.31) increases levels of turbulence and mixing, leading to local heat transfer

enhancement. Some examples are reported on Figs. 2.32 for two different geometries: a cylinder (a, Ireland and Jones, 1986) and two delta winglets (b, Tiggelbeck et al., 1991) attached to the cooled plate. Higher local heat transfer coefficients are achieved; however the features of the mechanism of heat transfer enhancement strongly depend on the geometry of the obstacle, the Reynolds number, and the position on the flat plate. The investigation of heat transfer modifications induced by a rib-roughened wall mounted normal to a flat plate constitutes one of the experiments conducted in this research project.

2.2 Natural convection from rib-roughened surfaces

Investigation of natural convection heat transfer from rough surfaces is useful mainly to resolve two issues: (i) the possibility of enhancing heat transfer from vertical surfaces by using roughness elements, (ii) the thermal behaviour of free-convection-cooled systems on which the roughness occurs naturally (such as electronic circuit boards).

Relatively little information is available in the literature on the effect of complex geometries on natural convection. In particular, the results obtained by artificially roughening vertical surfaces seem to conflict with one another with respect to the increase in the heat transfer. A compilation of published results for rough surfaces in natural convection has been presented by Bhavnani and Bergles (1990), as shown in Fig.2.33. Standard correlations giving the Nusselt number against the Rayleigh number for smooth vertical plates and cylinders together with data for rough surfaces (using the projected base area as a reference) are reported. Relationships for smooth geometries have been deduced by McAdams (1954), Eckert and Jackson (1951), Fujii et al. (1973), Heya et al. (1982). Large enhancements (50-200%) appear from data obtained by Jofre and Barron (1967) and by Ramakrishna (1978). They dealt with free convection in air from vertical surfaces roughened with triangular grooves and vertical cylinders with wires wrapped, respectively. Only moderate enhancements (0-10%) were found by Fujii et al. (1973) for roughened large-diameter vertical cylinders with repeated ribs, dispersed protrusions, and closely spaced pyramids. The study was experimentally performed with water and spindle oil as convective fluids. No increase in average heat transfer coefficient was reported by Heya et al. (1982) for convective heat transfer

in air and water from horizontal cylinders with dense pyramid-type, streak-type, and check-type roughness elements.

Together with data collected from the literature, Bhavnani and Bergles (1990) presented interferometric heat transfer results obtained for unbounded free convection from vertical surfaces with repeated ribs and steps. While the stepped surfaces were found to increase heat transfer (with respect to the smooth vertical plate) up to 23%, the ribbed surfaces resulted in degraded heat transfer performance. In spite of the increase in heat transfer surface area due to the ribs, the heat flux had a reduction up to 26%. As emerges from inspection of local heat transfer distributions for the vertical smooth plate (Fig.2.34 a) and for the square-rib-roughened plate with P/e=8 (Fig.2.34 b), the heat transfer coefficients for the rough surfaces are especially low just downstream and upstream of the ribs. This is due to reduction in buoyant flow velocity occurring near the obstruction. The high coefficients localised on the rib top do not compensate for the reduced heat exchange in the inter-rib regions.

A similar result was obtained by Acharya and Mehrotra (1993) for free convection in air in channels having either smooth or ribbed walls. Experiments, conducted for uniform heat flux and uniform wall temperature conditions, are condensed in the graphs of Figs.2.35 (a) and (b), respectively, in terms of average Nusselt number of the channel versus the modified Rayleigh number. Heat transfer reductions are typically of the order of 10% in the ranges of parameters explored.

2.3 Optical methods in heat transfer

Compared with other measurement methods in the area of heat transfer, optical methods possess remarkable advantages. First, the measurements do not disturb the temperature field since in most cases the energy absorbed by the medium is small compared to energy exchange by heat transfer. Second, the information is usually obtained over the entire temperature field (in the format of a simple photograph, for instance) instead of by point-by-point measurements. Optical methods in heat transfer can broadly be divided into two groups: the thermographic methods, which allow the thermal field evaluation on a solid surface and the index-of-refraction methods, which enable the reconstruction of the temperature distribution in transparent media. The two classes of methods are based on different

physical principles and generally their use involves a completely different instrumentation. Usually, the choice of the most suitable method is driven by the specific application; in some cases, thermographic and index-of-refraction methods can be jointly employed in the study of the same phenomenon (for instance, when thermal fields on solid surfaces and in a fluid are both to be determined).

2.3.1 Thermographic methods

Infrared thermography and liquid crystal thermography represent the most common optical methods used in detecting the temperature distribution on a solid surface. In infrared thermography the radiation heat transfer between the solid wall and the thermographic unit (a special camera) is detected by a sensor. A microprocessor reconstructs the thermal field on the emitting object from the radiant power exchanged, the object emissivity as well as the heat radiation laws being known. The output is generally a coloured image, displayed on a video screen, where each colour corresponds to a given temperature interval, according to a conventional code. The uncertainty in wall temperature has been estimated by Aliaga at al. (1994) to be ± 0.3°C.

Liquid crystal thermography is based on the selective reflectance (to white light) possessed by a surface when contaminated by particular substances called liquid crystals. The term **liquid crystal** derived from the characteristics of this material, which exhibits, in a particular phase called **mesophase**, the fluidity of a liquid while maintaining the anisotropic, ordered structure of a crystalline solid. The mesophases may be classified as nematic, cholesteric, and smectic (Jones, 1991). Their structures are shown schematically in Fig.2.36. In the nematic mesophase the molecules tend to line up in the same direction without order associated to the position. In the cholesteric mesophase the structure is similar to the nematic except for the direction of alignment of molecules which rotates with height through the liquid crystal. Several forms of the smectic mesophase can be identified: among them, the smectic A mesophase, in which monolayers of molecules are stacked upright and the smectic C mesophase, in which the molecules are stacked at an angle to the layer normal. The cholesteric liquid crystals are widely used as thermoindicators. In this phase the texture of the liquid crystal can exhibit two forms: the focal-conic and the grandjean textures. In the focal-conic texture the cholesteric helices pack around elliptical and

hyperbolic paths, in the grandjean texture the helical axes being aligned in the same direction. In this form, obtained from the focal-conic by mechanical shear, the liquid crystal is characterised by the selective reflection of white light. Over a known, reproducible range of temperature, the helix pitch, comparable with the visible light wavelength, changes with temperature. As a consequence, the wavelength of the reflected light changes and the liquid crystal will exhibit the corresponding colour of the visible spectrum (Fig.2.37). The range of temperature over which the colours are visible (**colour-play interval**) is usually narrow (a few K degrees); the colour displayed at the lower temperature margin is red whereas it becomes blue as the upper end of the interval is approached. The 'colour-play' interval is centred around the nominal **event temperature**. The colour-play interval as well as the event temperature can be varied by adjusting the liquid crystal composition, as shown in Fig. 2.38.

Liquid crystal compounds are difficult to deal with under most heat transfer laboratory conditions. Mechanical forces, chemical contamination and ultra-violet light can change the pitch of the helix and even destroy the material. Several approaches have been developed to make liquid crystals more practical to use: the most popular method of protection is to encapsulate the liquid crystal in small polymer shells as gelatin. These capsules (from 5 to 50 microns in diameter) are mixed with a binder and sprayed onto the surface under test to form a thin coating (Fig.2.39 a). In alternative methods, the unencapsulated (neat) material can be applied on the surface with a clear plastic sheet (Fig.2.39 b) or dispersed in a continuous polymer sheet (Fig.2.39 c). The solutions described effectively isolate the liquid crystals from the degrading effects of the environment, although ultraviolet light can still cause problems.

Before applying the liquid crystals the surface must be coated with black paint (to avoid interaction between the reflection of the liquid crystal film and of the substrate). The black paint must be compatible with solvents used for the liquid crystal mixture composition. The most convenient manner to measure the thermal field on a complex surface is to coat it with a pre-packaged assembly consisting of a liquid crystal layer painted on a plastic sheet having a background colour with black ink. A liquid crystal monolayer of a few microns is sufficient to display brilliant colours.

The use of liquid crystal is not limited to temperature measurements on

solid walls. In fact, both neat and encapsulated liquid crystals can be mixed (in small percentages, such as 0.5-1% by weight) in fluids (such as glycerol) as streamline tracers and temperature indicators (Hiller and Kowalewski,1986, Tanaka,1988, Akino et al.,1989).

Before the execution of a thermal visualisation experiment, the optical characteristics of the combination of the liquid crystal sheet, the light source, and the optical and camera system (if any) have to be identified. Usually, a calibration experiment is performed using the same material (liquid crystal, light sources and optical devices) as the main experiments. The aim of the calibration is to assess the relationship between the temperature and the colour. The calibration experiment can be conducted on a separate system (on which controlled thermal conditions are imposed) or directly on the surface under test, equipped with a number of pre-calibrated thermocouples in order to associate the colour with the recorded temperature. Care must be taken to ensure, during the main experiments, the same lighting and viewing conditions as the calibration test, since the colour pattern can be significantly affected by lighting and viewing angles.

In order to interpret the colour pattern exhibited by the liquid crystal sheet, three broad classes of techniques are available: (i) human observation, (ii) intensity-based image processing, and (iii) hue-based image processing. Human observers can interpret liquid-crystal images by direct visual inspection of the test section, of colour photographs, or of tape recorded video images. The associated uncertainty is generally 1/3 of the colour play interval, i.e. about 0.2-0.5 K for narrow band liquid crystals. The second method is based on narrow-band optical filters, through which equally coloured regions can be extracted. Using a multiple narrow-band spectral intensity interpreter, that is, a set of narrow-band filters, the behaviour of liquid crystals can be interpreted in terms of the variation of intensity with wavelength. The resolution of this method is about 0.1 K (Akino et al.,1989). The third approach is based on the relationship between the hue and the temperature. The hue is an optical attribute related to the actual colour of the point of observation. The hue distribution can be obtained by converting the image recorded by a RGB videocamera in the dominion of HSI parameters (Hue, Saturation and Intensity) by using an appropriate frame grabber. Among these parameters, hue is directly related to temperature through a known relationship

obtained from calibration. Therefore, the thermal field reconstruction can be performed in real time again within 0.1 K of resolution.

2.3.2 Index-of-refraction methods

In these methods, the index of refraction or a spatial derivative of the index of refraction of a medium is measured, and from this the temperature distribution of the medium is determined. They are used to study thermal and density fields in transparent substances, generally gases or liquids. The index-of-refraction methods can be divided into two groups: the interference methods based on differences in lengths of the optical paths, and the shadowgraph and schlieren techniques, utilising the deflection of light in the measurement media. Although all these methods depend on variation of the index of refraction in a transparent medium and the resulting effects on a light beam passing through the test region, quite different quantities are measured with each one. Only a brief description of some index-of-refraction methods will be given in this paragraph since they are extensively described in the literature (e.g., Hauf and Grigull, 1970, Merzkirch, 1974, and Eckert and Goldstein, 1976).

The index-of-refraction techniques are valuable when visualising flows in which density differences occur naturally or are artificially induced. They are essentially integral (the measured quantity is integrated over the length of the light beam) and thus well suited to measurements in two-dimensional fields which do not have significant density variations along the light beam path. Even so, developments in three-dimensional conditions are under progress (Michael and Yang,1992 and Collins et al.,1994) involving tomographical reconstruction procedures.

In these methods, the index of refraction determines the light pattern. According to the Gladstone-Dale equation, the index of refraction n of gases, when close to 1, is simply related to the local density:

$$(n-1)/\rho = C \qquad (2.5)$$

The Gladstone-Dale constant C is a function of the particular gas and varies slightly with wavelength. For example, for air C is about $0.226 \cdot 10^{-3}$ m^3/kg in the visible wavelength range. In reference conditions (P_o=1 atm, T_o=20°C) one obtains

$$(n_o-1)/\rho_o = C \qquad (2.6)$$

It follows that:

$$\rho = \rho_o (n-1)/(n_o-1) \tag{2.7}$$

In two-beam interferometry, the distribution of the index of refraction n is obtained. Using the ideal gas model:

$$1/T = (1/T_o)\cdot(n-1)/(n_o-1) \tag{2.8}$$

from which the temperature field can be directly evaluated.

When the spatial first derivative of n is determined from the optical techniques, such as schlieren or differential interferometry, one obtains

$$\partial\rho/\partial y = (\partial n/\partial y)\cdot\rho_o/(n_o-1) \tag{2.9}$$

and therefore

$$\partial T/\partial y = -T^2\cdot(\partial n/\partial y)\cdot R\cdot\rho_o/(P\cdot(n_o-1)) = -T^2\cdot(\partial n/\partial y)\cdot R/(P\cdot C) \tag{2.10}$$

where R is the gas constant and P the pressure.

Interferometry is a powerful method for investigating convective heat transfer. It enables an entire flow field to be viewed and gives a permanent record of the flow. The thermal field information is condensed in an interference pattern arising from the recombination of two beams travelling along different paths. An early interferometer was designed by Michelson in 1881. As shown in Fig.2.40, the beam emitted by the light source is divided in two by a beam-splitter. The two rays travel normal to each other to separate plane mirrors and are then reflected back to the beam-splitter. Parts of the wave then unite and leave the beam splitter in the direction of the screen. If the two distances between the beam splitter and the mirrors are strictly equal, the angle θ is exactly 45° and the fluid is isothermal, the light beams travel at the same speed along paths having the same length; then for this case no interference is expected. When in the test section the fluid is not isothermal, since the index of refraction changes with temperature the two beams reach the screen with a phase difference and hence interference fringes are observed on the screen. Since each fringe represents the locus of points of the test section that shift the beam by integer multiples of the source wavelength, it may be easily shown that the fringes represent lines of equal index of refraction n and, according to Eq.(2.8), of equal fluid temperature.

A modification to the Michelson interferometer was developed by Mach and Zehnder in 1891. In the Mach-Zehnder interferometer, sketched in Fig.2.41, the source beam is divided into two halves, each travelling along two sides of a quadrilateral arrangement. They thus recombine and form

interference fringes on the screen when the test section is not isothermal. Even in this device accurate alignment and high quality optics are necessary.

Many other interferometers exist to study a wide range of optical phenomena. Whereas the Michelson and Mach-Zehnder instruments operate a division into two of the source beam (two-beam interference), in differential interference each source ray is split into two parallel rays travelling with a small lateral displacement. In such an arrangement, both measurement and reference beams pass through the test section before interfering. The fringes formed on the screen are related to the index-of-refraction gradients. Therefore, Eq.(2.10) has to be applied so as to reconstruct the thermal field in the test section. The splitting of the source rays is usually produced by a birefringent prism (Wollaston prism) consisting of two birefringent uniaxial crystals glued together.

Further developments in interferometry occurred with the application of principles of holography and with the invention of a coherent light source (the laser). Among the advantages of holographic interferometry is the relatively low cost of the system as compared to the Mach-Zehnder arrangement, since very high quality optics are no longer required. In addition, the laser source greatly improves the quantitative interpretation of the interferometric pattern. A typical holographic system is schematically shown in Fig.2.42. The light beam, coming from a laser source, is split into two coherent beams, one of which passes through the test section while the other (the reference beam) bypasses the test section. The two beams are recombined on a photographic plate. The resulting hologram is a diffraction grating formed by the emulsion of the plate. Two different procedures are mainly followed, namely *double-exposure* and *real time* techniques.

In the double exposure technique, two exposures are recorded on the hologram: the first of the test section in the isothermal condition, and the second after a phase change (such as a thermal gradient) introduced to the test section. The diffraction grating formed on the hologram has to be successively interrogated illuminating it by the reference beam only. The diffraction of the reference beam produces the fringe pattern directly related to the thermal field in the test section.

The real time technique involves taking one exposure on the plate (with the test section isothermal). The plate is then developed and

replaced, with great accuracy, in its original position. In such a way, when thermal gradients are present, the fringes are observed in 'real time', thus enabling temperature changes with time to be detected.

Unlike interferometric systems, there is a different class of methods which are not based on phase shift between two rays but depend on the spatial deflection of a light beam owing to index-of-refraction inhomogeneities. Among these methods, the schlieren techniques is the most frequently employed for qualitative and quantitative investigations.

The principles of the schlieren method have been known since the 17th century, according to Hooke and Huygens schlieren observations but the technique laid dormant for 200 years. The French astronomer Leon Foucault (1859) used it as a means of quality control in the manufacture of large astronomic objectives. Some years later, the German physicist August Töpler (1864) applied the method to the study of gaseous inhomogeneities ("schlieren" is the German term for striations or inhomogeneities). The connection between the light ray deflection and the thermal field in the test section can be illustrated by means of the sketch of Fig.2.43. The figure shows a light beam, travelling initially in the z direction, passing through a medium whose index of refraction n varies (for simplicity) only in the y direction. At the time τ the beam is at position z, and the wavefront (surface normal to the path of the light) is as shown. Since n is a function of y, the speed of the light $c = c^*/n$ (c^* being the light speed in vacuum) will not be the same for the incoming wavefront. With reference to the two margin rays delimiting the wavefront, after a time interval $\Delta\tau$, they have moved along z a distance of $c_y\Delta\tau$ and $c_{y+\Delta y}\Delta\tau$, respectively. As a consequence, the light beam has turned through an angle $\Delta\alpha_y$ given by:

$$\Delta\alpha_y=(c_y\Delta\tau - c_{y+\Delta y}\Delta\tau)/\Delta y = -(\Delta c/\Delta y)\Delta\tau = =-c^*(\Delta(1/n)/\Delta y)\Delta\tau \qquad (2.11)$$

Since the variations of n are generally small, the distance Δz can be expressed as $\Delta z = c\Delta\tau = c^*\Delta\tau/n$. It follows that

$$\Delta\alpha_y=-n(\Delta(1/n)/\Delta y)\Delta z \qquad (2.12)$$

and, in the limit of very small increments,

$$d\alpha_y=-n(d(1/n)/dy)dz = [(1/n)dn/dy]dz \qquad (2.13)$$

Integrating the above relationship along the optical path L (in the z-direction) leads to:

$$\alpha_y=\int_L[(1/n)dn/dy]dz \cong L(1/n_o)dn/dy \qquad (2.14)$$

where n_o is the index of refraction of the medium outside the test section and dn/dy is the local index-of-refraction gradient, constant along z.

Introducing the Gladstone-Dale rule and the ideal gas equation of state, one obtains:

$$\alpha_y=(-CP/RT^2)(\partial T/\partial y) \qquad (2.15)$$

and, in the x-z plane

$$\alpha_x=(-CP/RT^2)(\partial T/\partial x) \qquad (2.16)$$

Therefore, a schlieren system is basically a device to measure the angle α (or an optical parameter connected to it) as a function of position in the x-y plane normal to the light beam.

The basic arrangement of the schlieren processor was developed by Töpler (Fig.2.44). It consists of a non-coherent light source, two lens and a screen. The first lens L_1 provides a parallel light beam entering the field of disturbance in the test section. The light (deflected and undeflected rays) is then collected by a second lens L_2 ("schlieren head") and projected onto a screen located at the conjugated focus of the test section. The angular deflection α of each ray can be identified by placing, on the focal plane of lens L_2 (cut-off plane), a knife or a filter. As shown in Fig.2.44, if the light beam at a position x,y in the test region is deflected by an angle α_y, the image of the source coming from that position will be shifted at the knife-edge by an amount $\Delta_y=f_2\alpha_y$, where f_2 is the focal length of the lens L_2. Therefore, if the knife-edge is moved from its original position by an amount equal to Δ_y (along the focal plane of the schlieren head), a shadow will be formed on the screen. The boundary between light and shadow defines the locus of images of points which deflect light through the same angle of deflection α_y $(=\Delta_y/f_2)$.

Several different arrangements have been proposed in lieu of the original Töpler scheme ("Z" arrangement instead of on-line optical path, focal filament and colour filters instead of the knife-edge), and most of them have been described by Vasil'ev (1971) and Settles (1985). From the quantitative point of view, temperature distribution in convective flows can be extracted from schlieren photographs (obtained by replacing the screen by a camera) such as the ones shown in Fig 2.45 (Tanda, 1993). Since the dark regions (except for the opaque bodies profiles) represent the shadows of a thin filament moved on the cut-off plane and then the locus of points deflecting the light through the same (known) angle, by processing a

series of such photographs it is possible to obtain the distribution of the temperature in the test section. This operation can be performed manually even though very time-consuming, or automatically. The sequence involves digitising a series of photographs recorded for different values of α, superimposing them, extracting the α-distribution in the optical fields and processing this data, by appropriate algorithms based on Eqs.(2.10), to reconstruct eventually the thermal field.

The quantitative schlieren system based on the focal filament is relatively simple, neither laser source nor light intensity measurements being required. The equipment is straightforward to align, easy to operate and inexpensive.

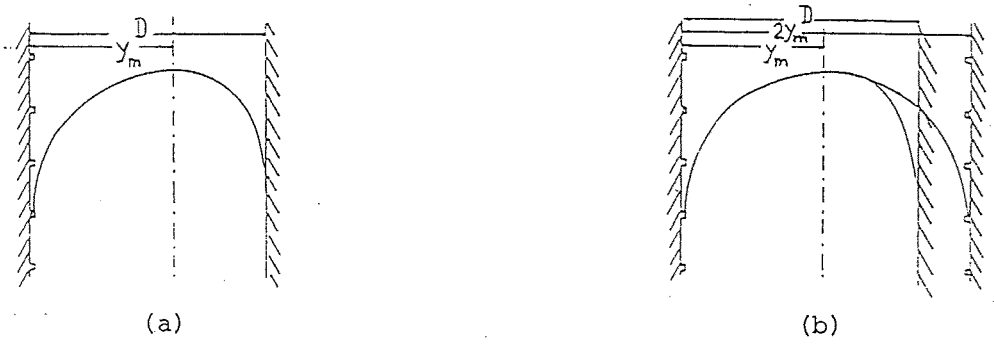

FIGURE 2.1 Schematic presentation of the Hall transformation theory: (a) the real rough channel; (b) the "equivalent" rough channel.

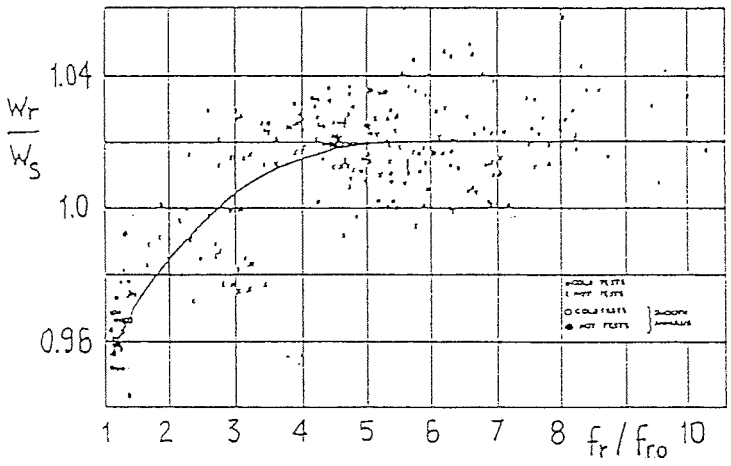

FIGURE 2.2 Ratio of mean velocities as a function of friction ratio.

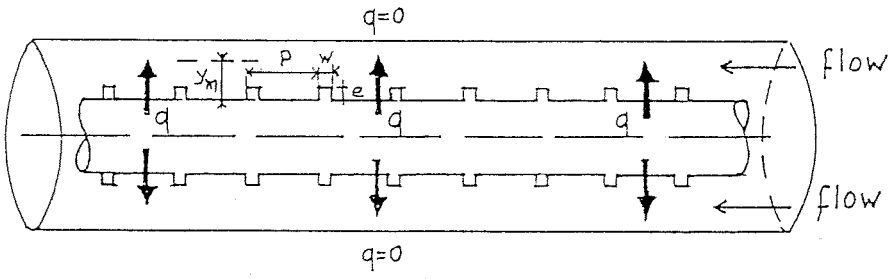

FIGURE 2.3 Drawing of an annulus with rough-inner and smooth-outer surface

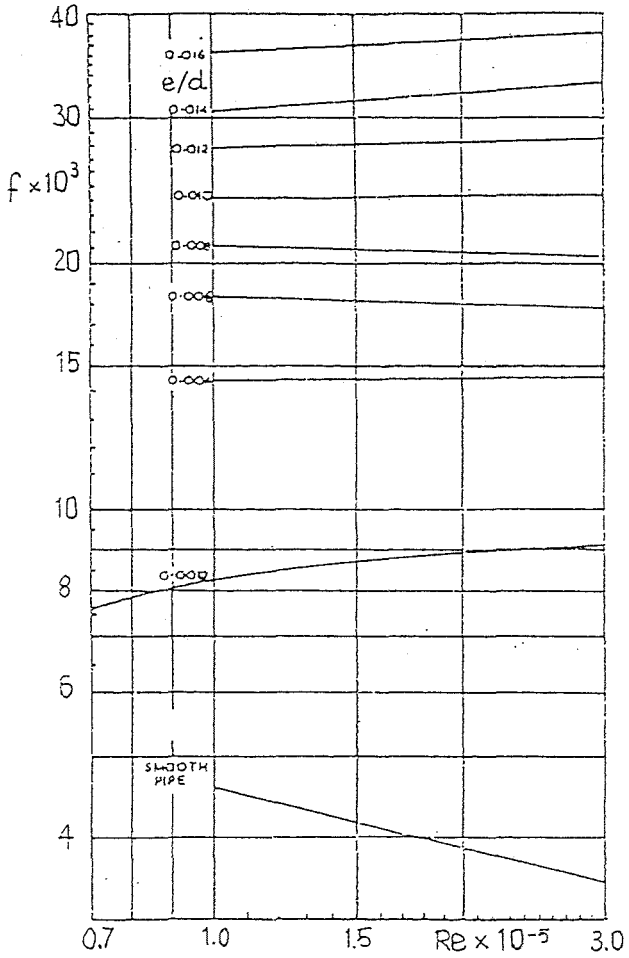

FIGURE 2.4. Friction factor for rough surfaces with P/e=12.

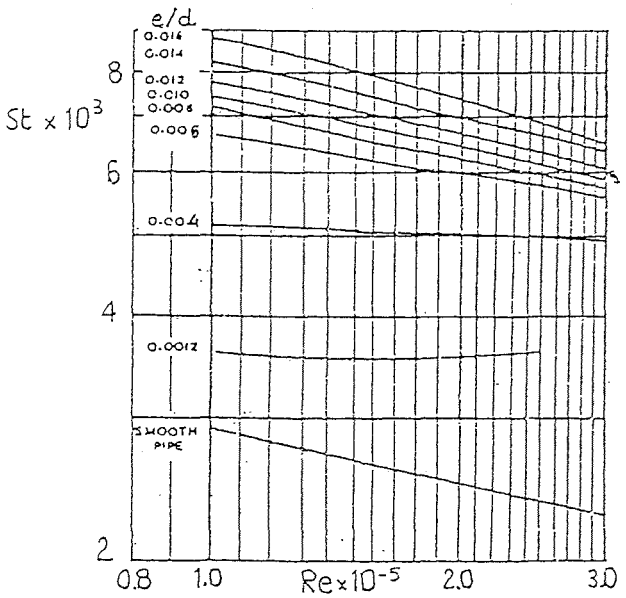

FIGURE 2.5. Stanton number for rough surfaces with P/e=12.

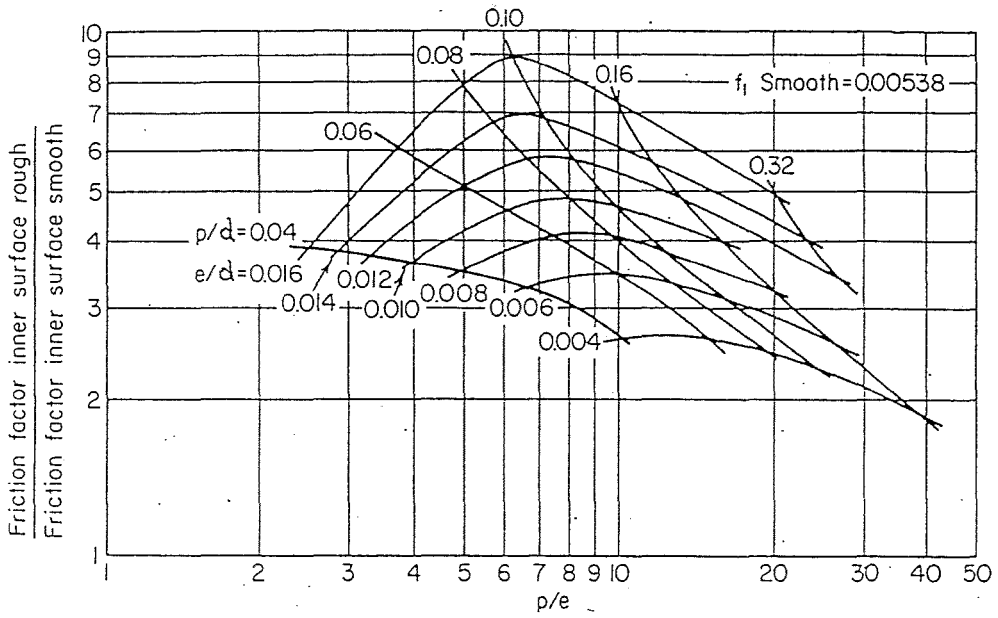

FIGURE 2.6. Friction factor relative to smooth surface value ($Re=10^5$).

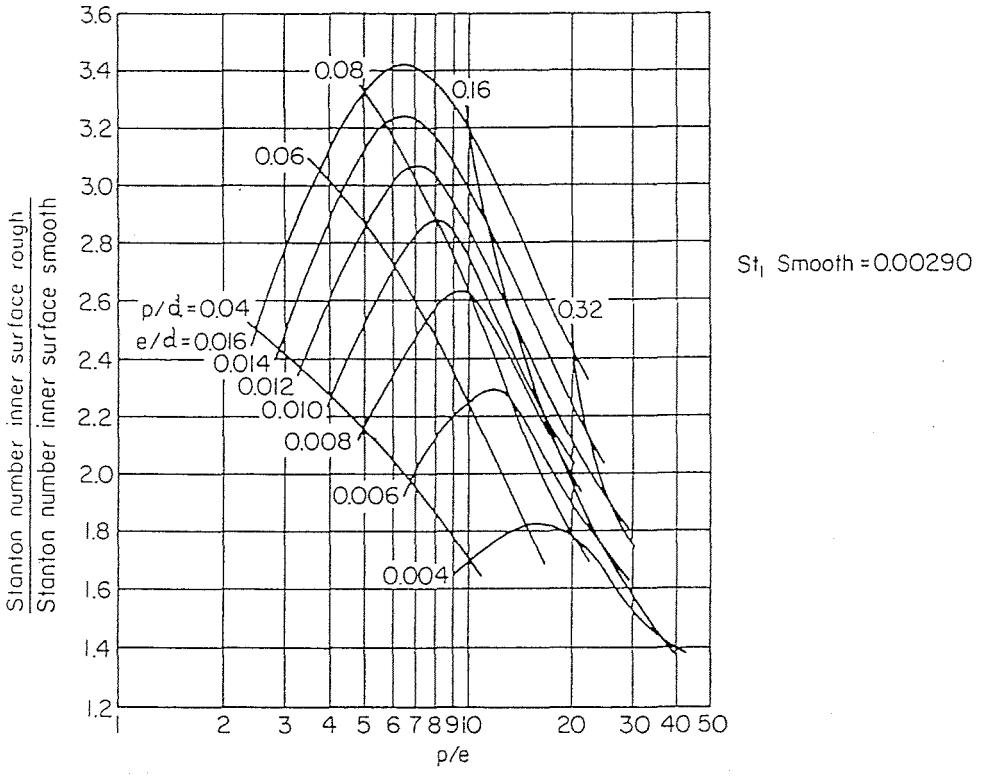

FIGURE 2.7. Stanton number relative to smooth surface value ($Re=10^5$).

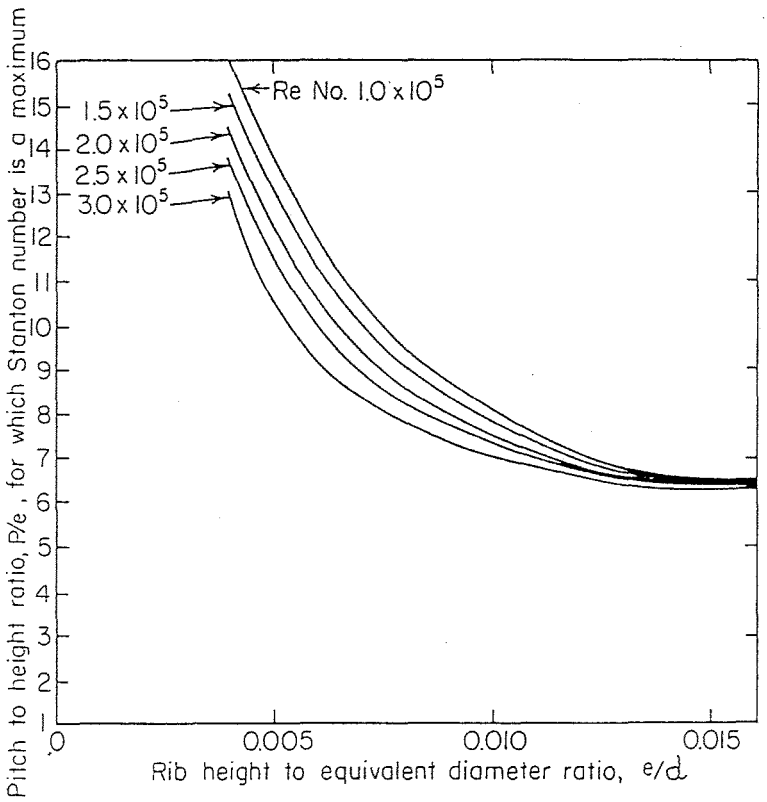

FIGURE 2.8. Values of P/e for which St number is a maximum.

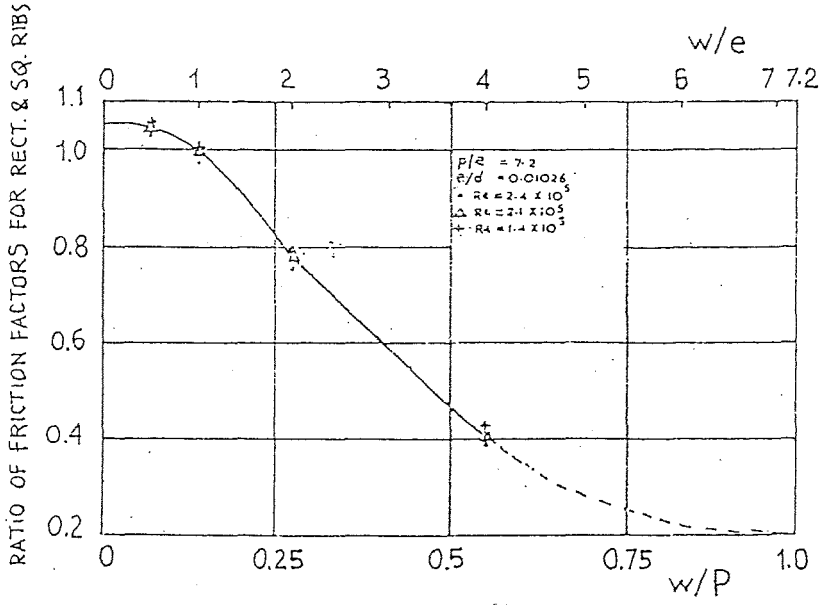

FIGURE 2.9. Effect of rib width w on friction.

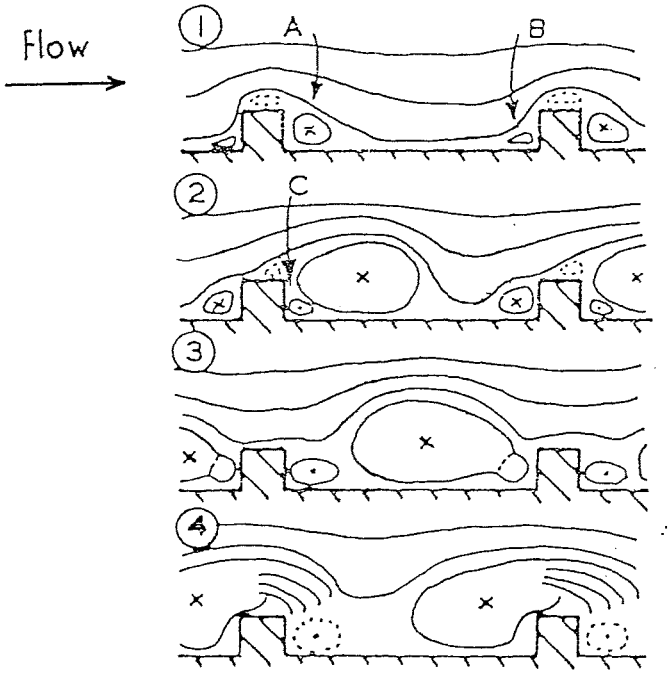

FIGURE 2.10. Time-evolution of flow patterns (square ribs, P/e=7).

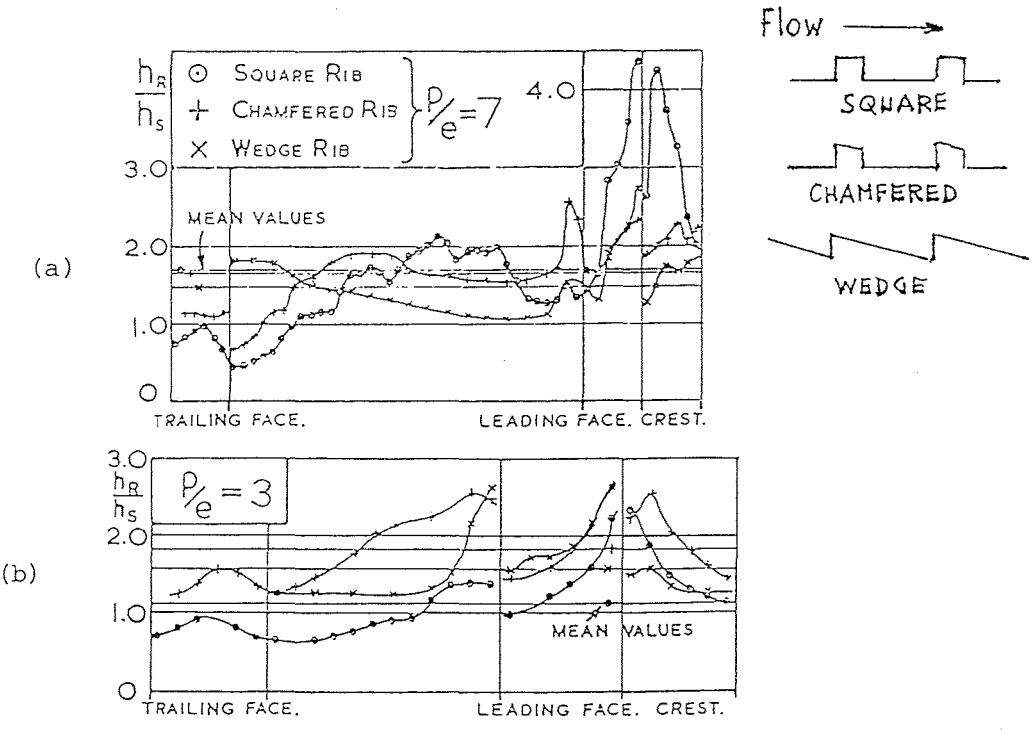

FIGURE 2.11. Relative heat transfer distributions: (a) P/e=7, (b) P/e=3.

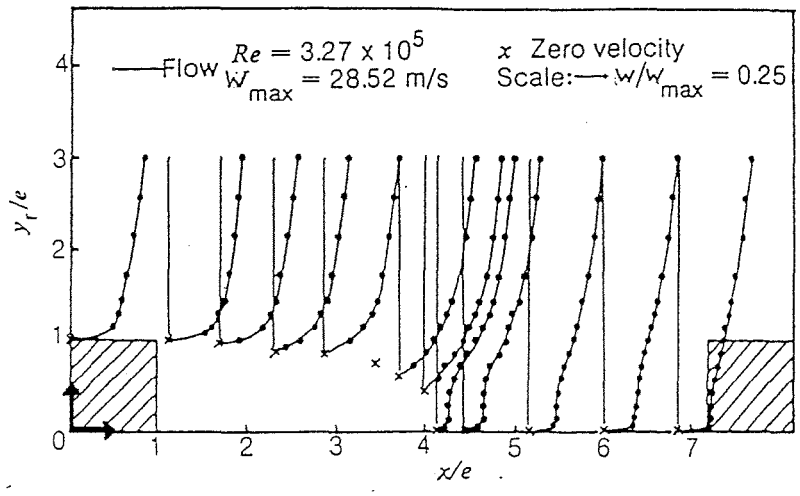

FIGURE 2.12. Mean velocity profiles between the ribs. The reattachment point occurs at 3.1e behind the ribs, independently of the channel height.

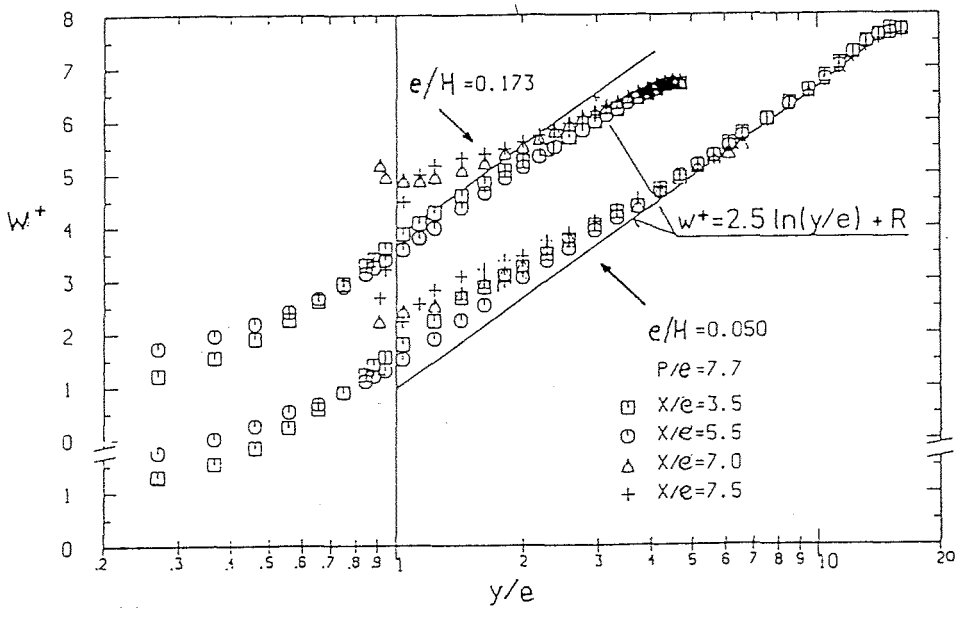

FIGURE 2.13. Non-dimensional rough-wall velocity profiles as compared with constant-slope velocity profiles (H = channel height).

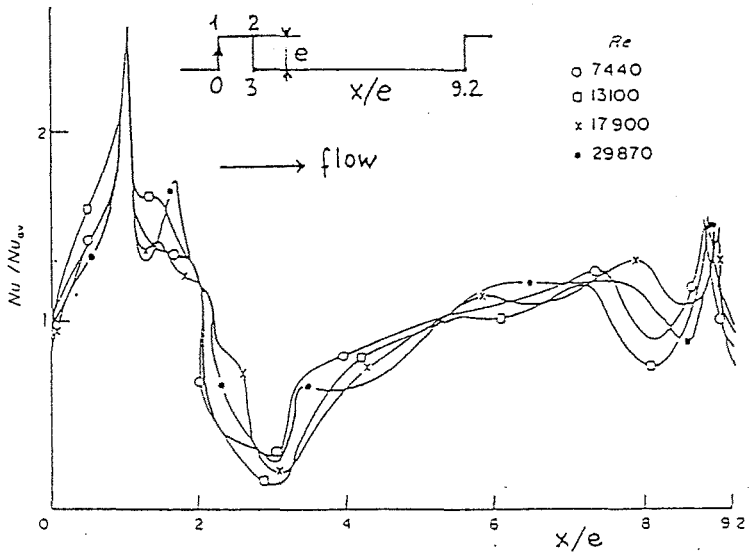

FIGURE 2.14. Relative Nusselt number distributions for square-rib geometry

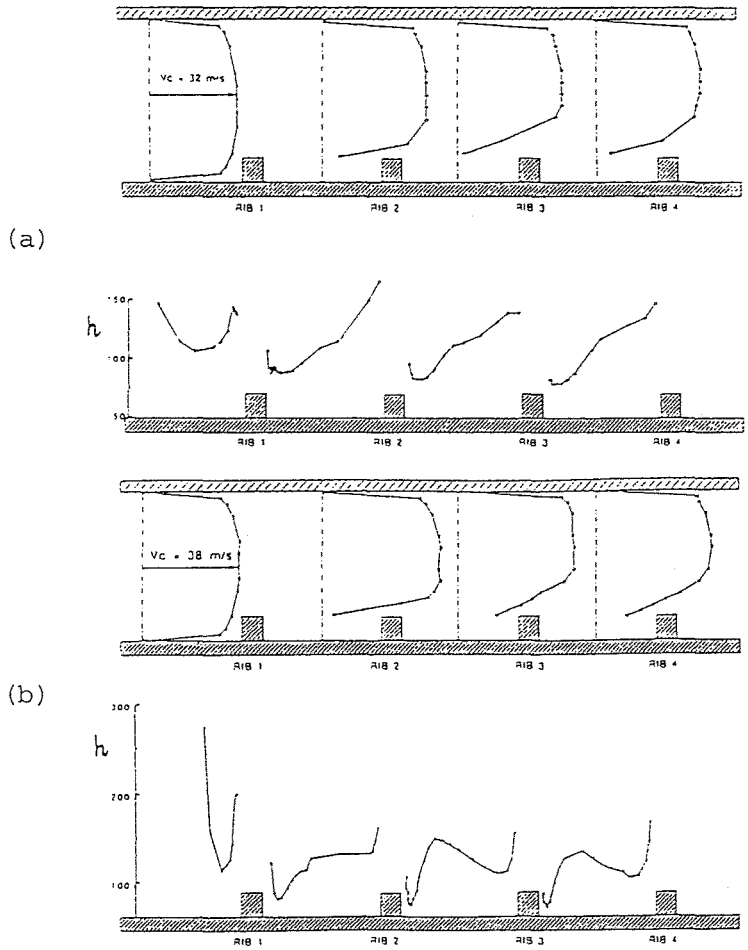

FIGURE 2.15. Mean velocity profiles and heat transfer coefficient distributions along ribbed plates. (a) P/e=5, $Re=10^6$, (b) P/e=12, $Re=1.5 \cdot 10^6$.

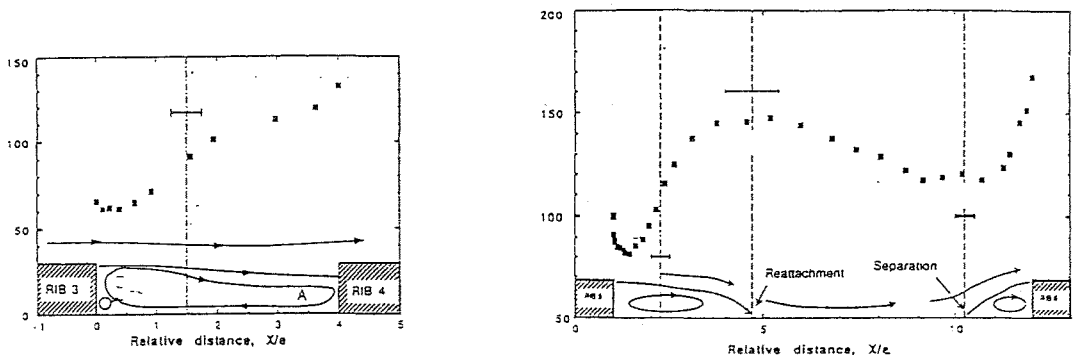

FIGURE 2.16. Heat transfer coefficients and possible flow distributions around first three ribs: P/e=5,Re=10^6 (left) and P/e=12, Re=$1.5 \cdot 10^6$ (right)

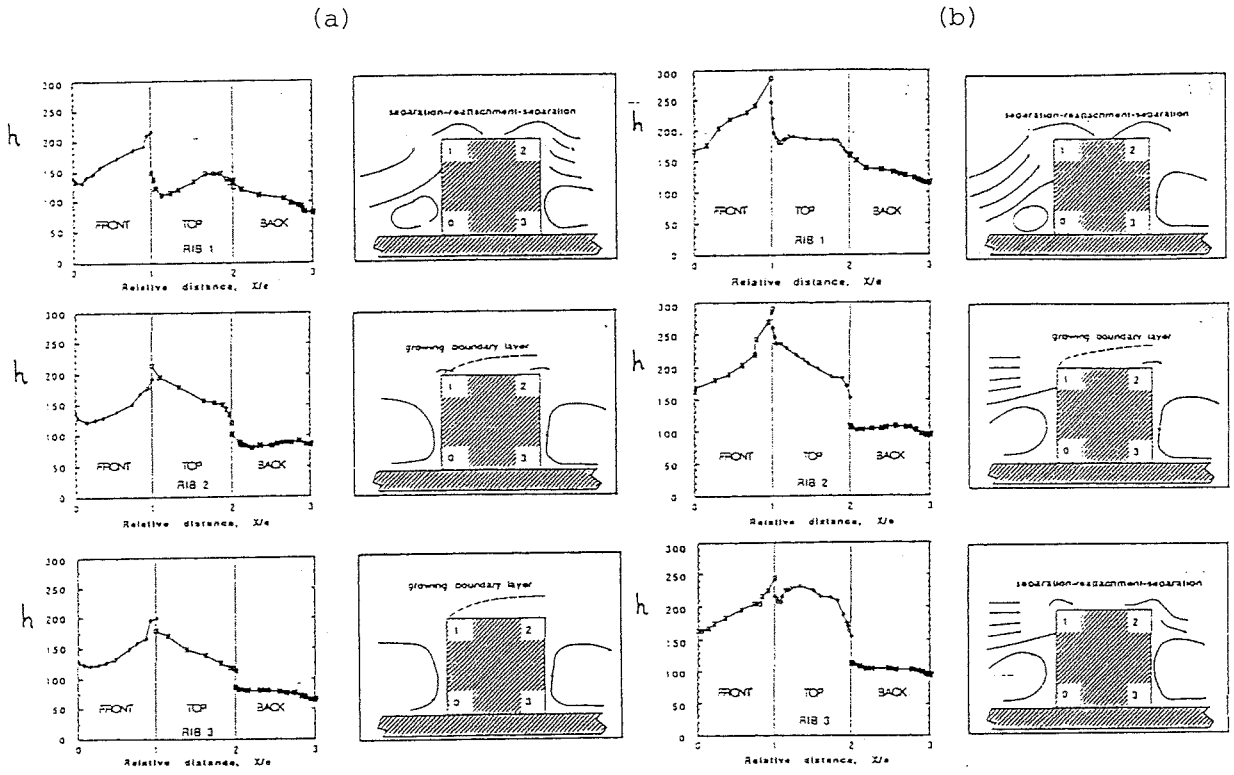

FIGURE 2.17. Local heat transfer coefficients and flow visualisation. (a) P/e=5, Re=10^6, (b) P/e=12, Re=$1.5 \cdot 10^6$.

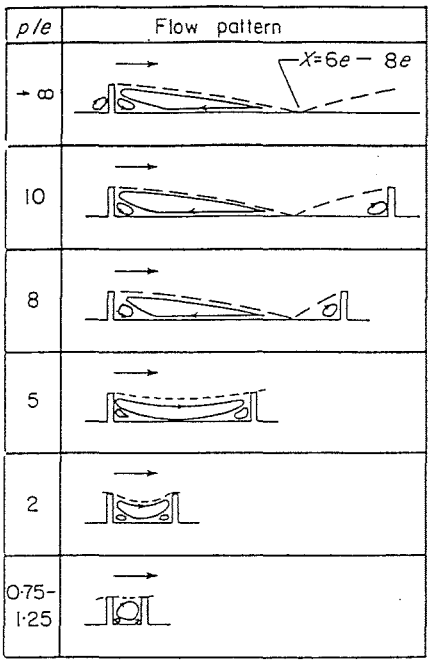

FIGURE 2.18. Flow patterns as a function of P/e.

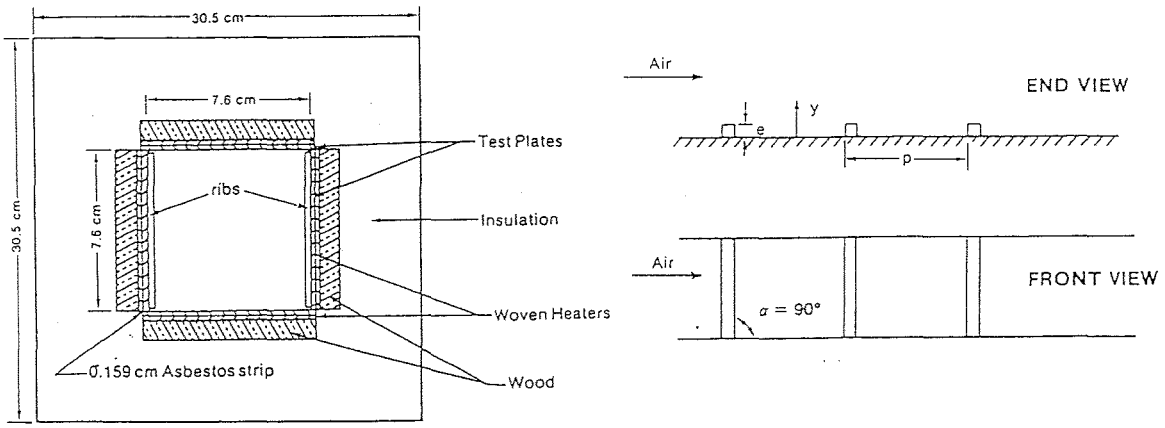

FIGURE 2.19. Cross section of a two rib-roughened wall channel and end/front view of the ribbed surface.

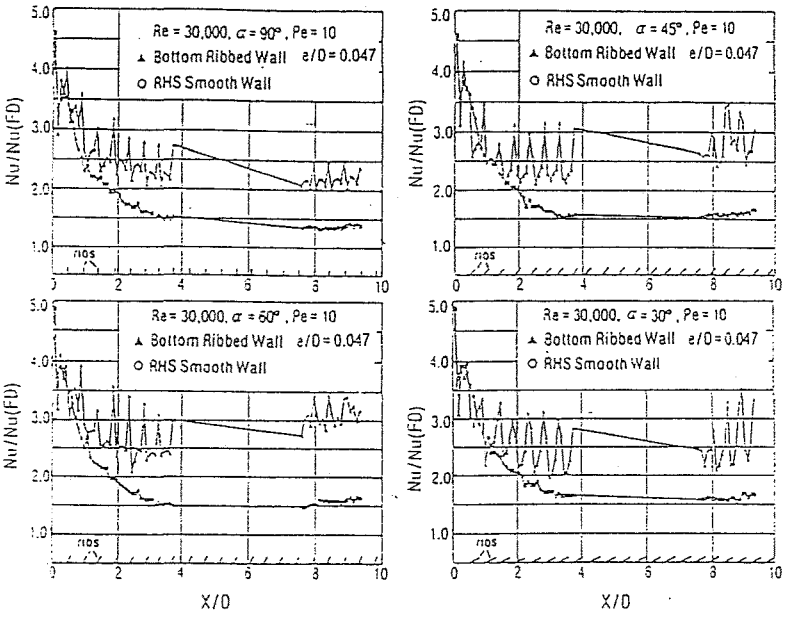

FIGURE 2.20 Centreline heat transfer distributions in the square channel (D equivalent diameter, Nu(FD) Dittus-Boelter Nusselt number).

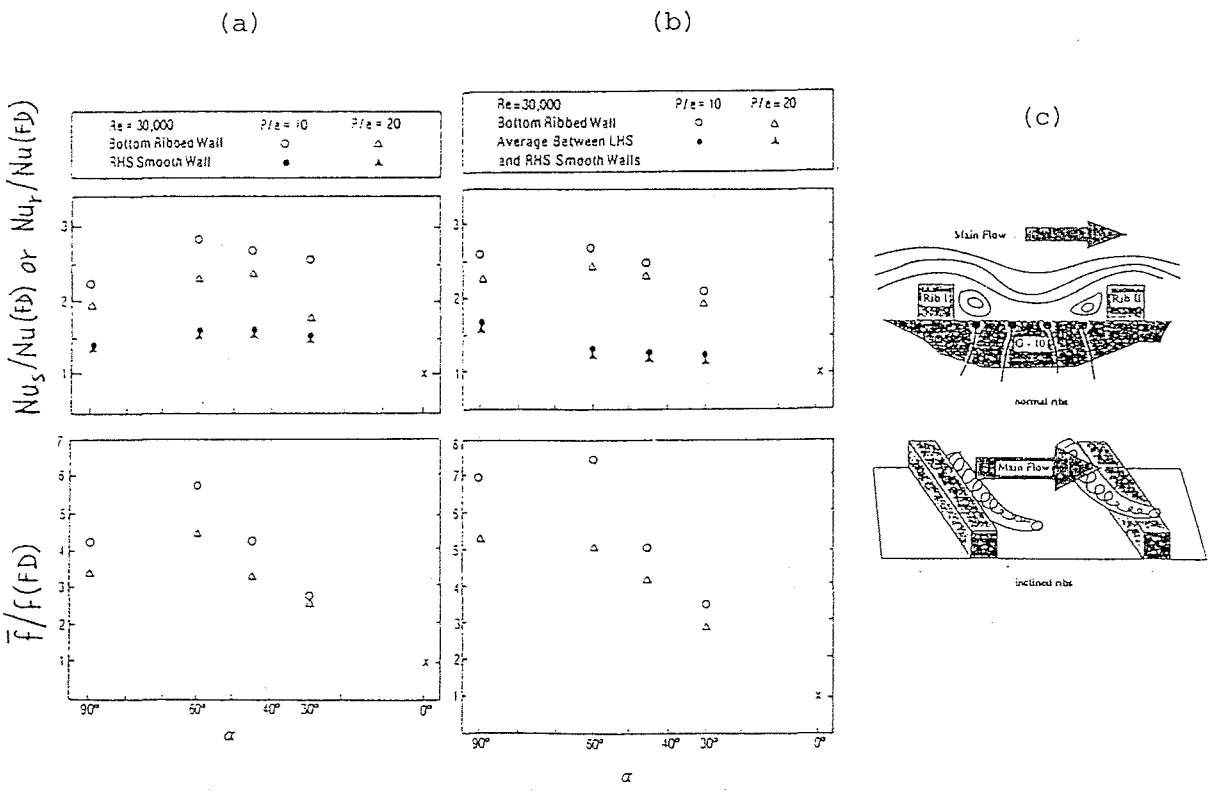

FIGURE 2.21 Heat transfer and friction versus rib angle-of-attack α: (a) square channel; (b) rectangular channel (aspect ratio 4). (f(FD) Blasius friction factor; $\bar{f}$ mean friction; Nur,Nus refer to rough and smooth sides); (c) flow mechanism in passages with normal and inclined ribs.

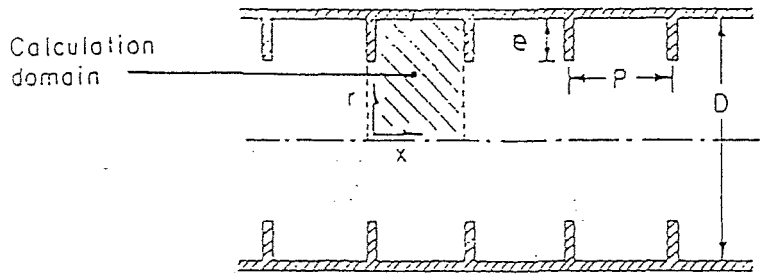

FIGURE 2.22 Tube with internal circumferential fins.

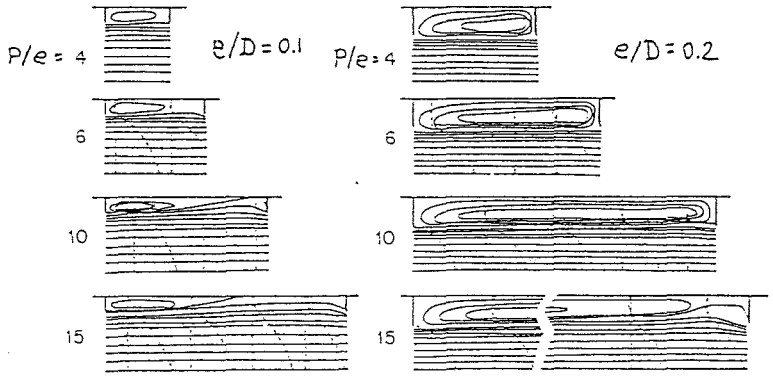

FIGURE 2.23 Velocity fields for Re=500.

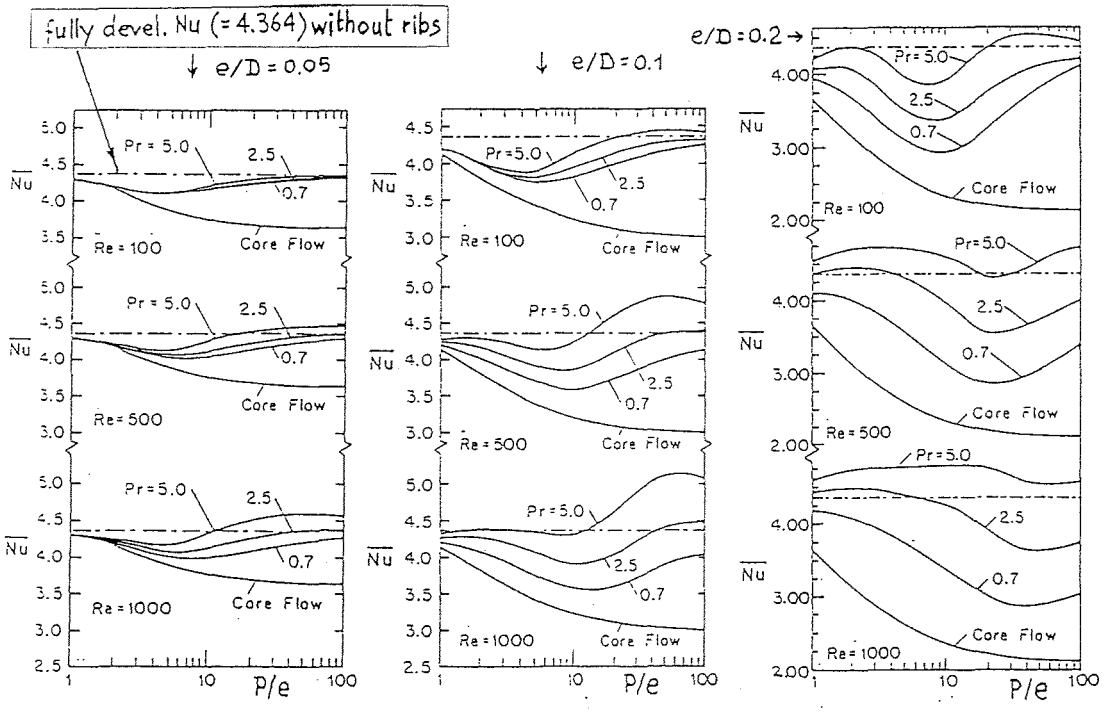

FIGURE 2.24 Overall Nusselt number for e/D = 0.05, 0.1, and 0.2.

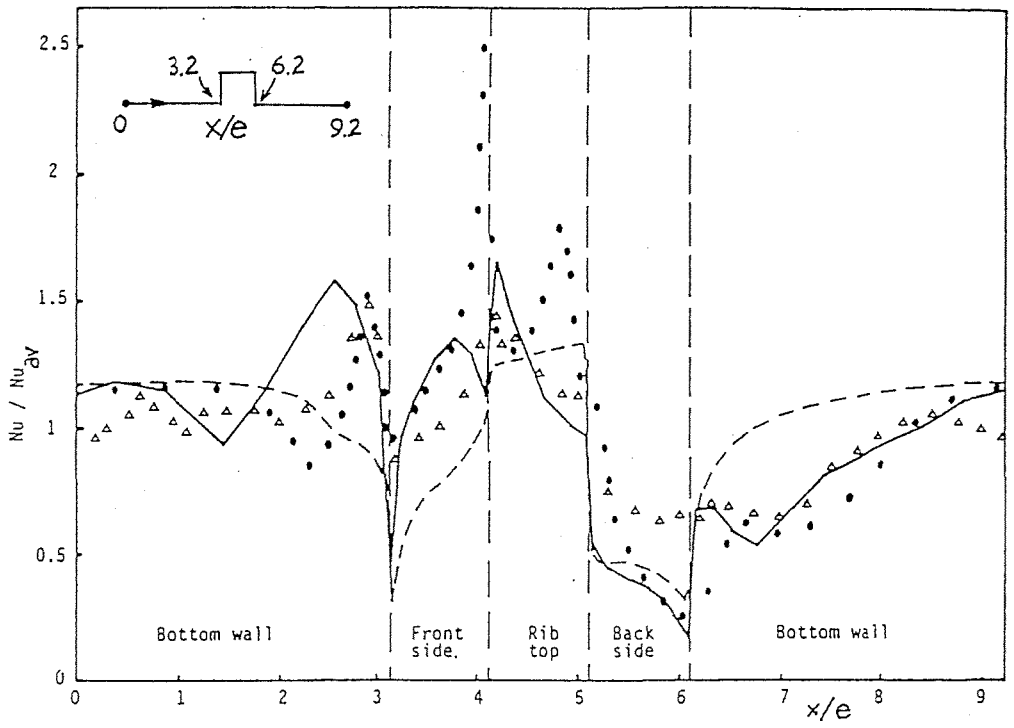

FIGURE 2.25 Relative Nu number along the ribbed wall (continuous line: LES predictions, dashed line: k-ε predictions, symbols: experiments).

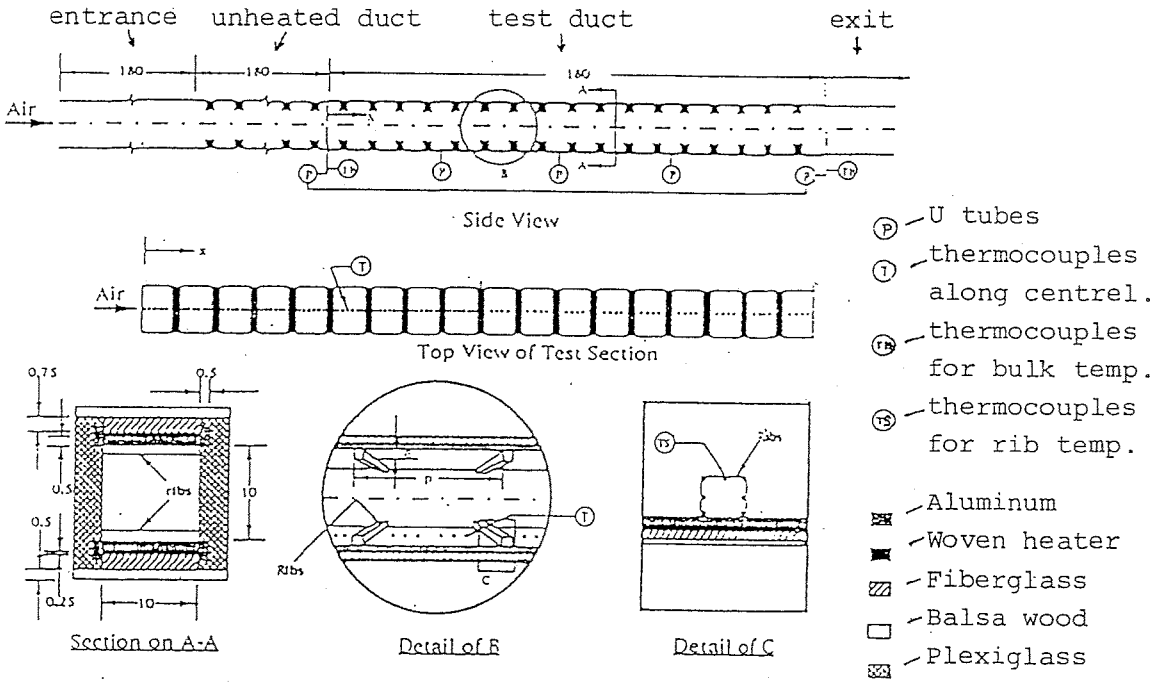

FIGURE 2.26 Detailed thermocouple locations in a ribbed wall.

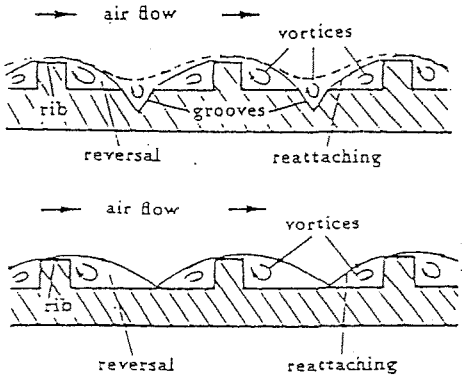

FIGURE 2.27 Conceptual flow pattern in channel with ribbed-grooved wall (top) as compared with the ribbed wall channel case (bottom).

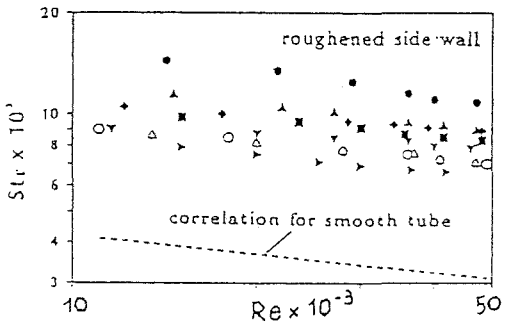

FIGURE 2.28 Stanton number versus Reynolds number (closed symbols: ribbed-grooved wall, open symbols: ribbed wall).

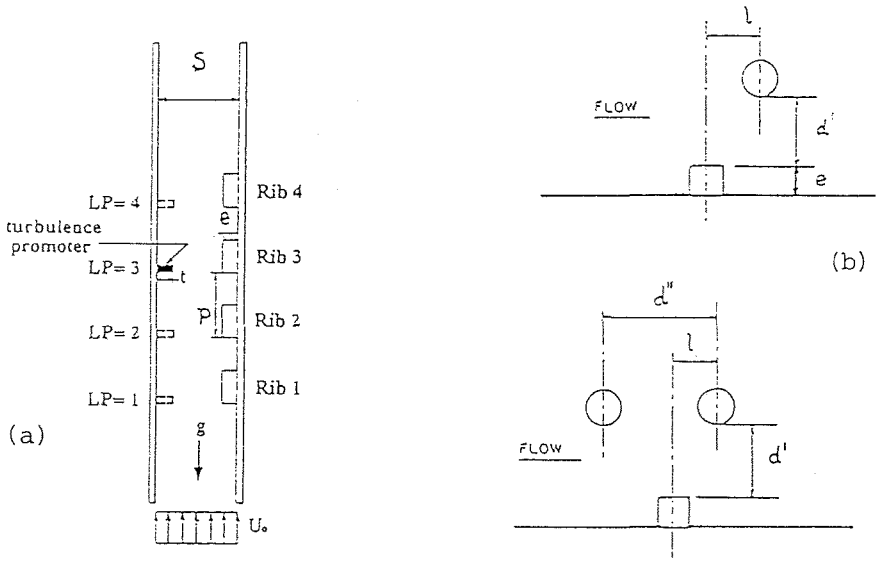

FIGURE 2.29 Prismatic (a) and cylindrical (b) turbulence promotors displaced in front of a rib-roughened surface.

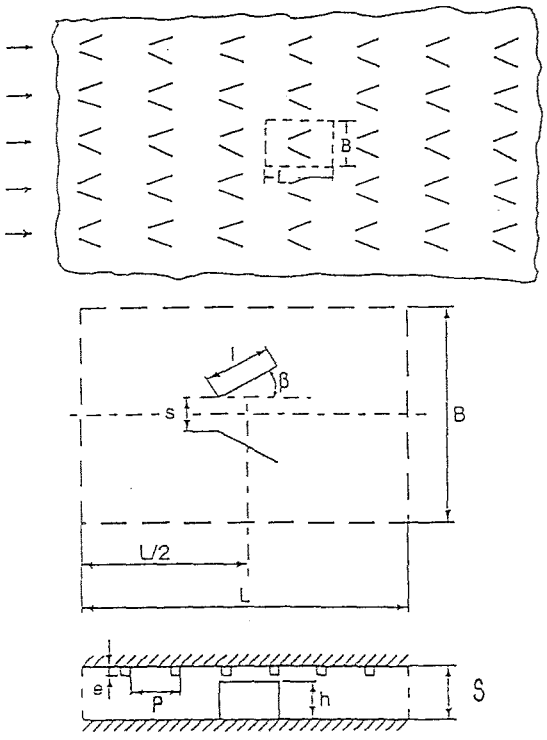

FIGURE 2.30 Schematic of a parallel wall channel with a series of vortex generators mounted on one channel wall opposite to a rib-roughened surface.

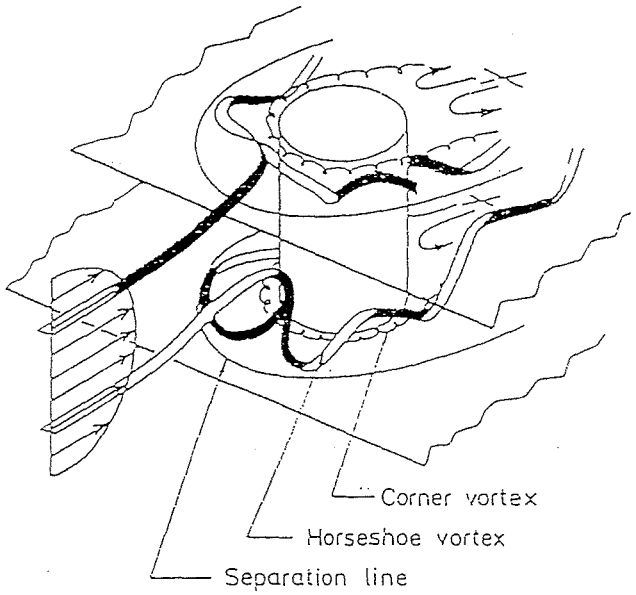

FIGURE 2.31 A simplified sketch of the vortex structure around a pedestal in fully developed passage flow.

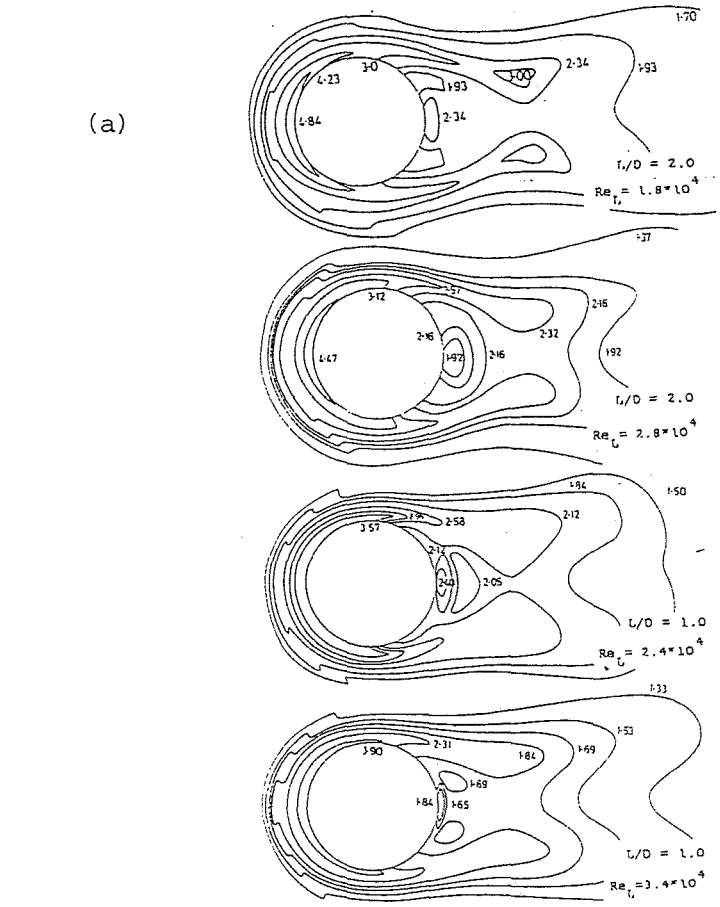

FIGURE 2.32 End wall Nusselt number contours for (a) a cylindrical pedestal (values normalised with respect to those for smooth surface) and (b) for a pair of delta winglets.

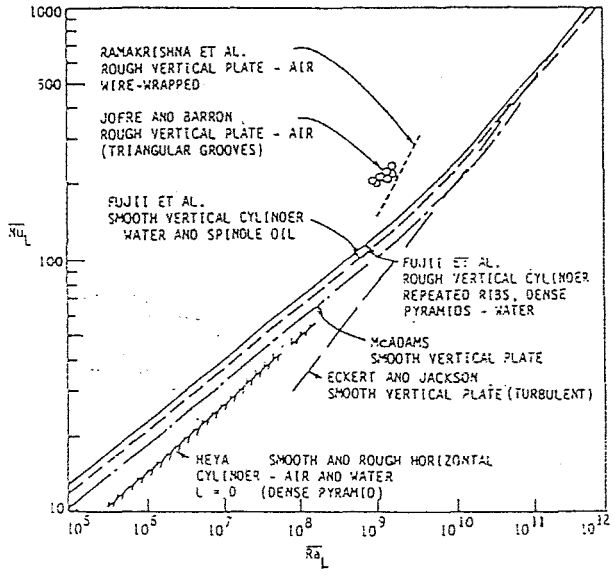

FIGURE 2.33 Composite of data on rough surfaces in free convection.

(a)

(b)

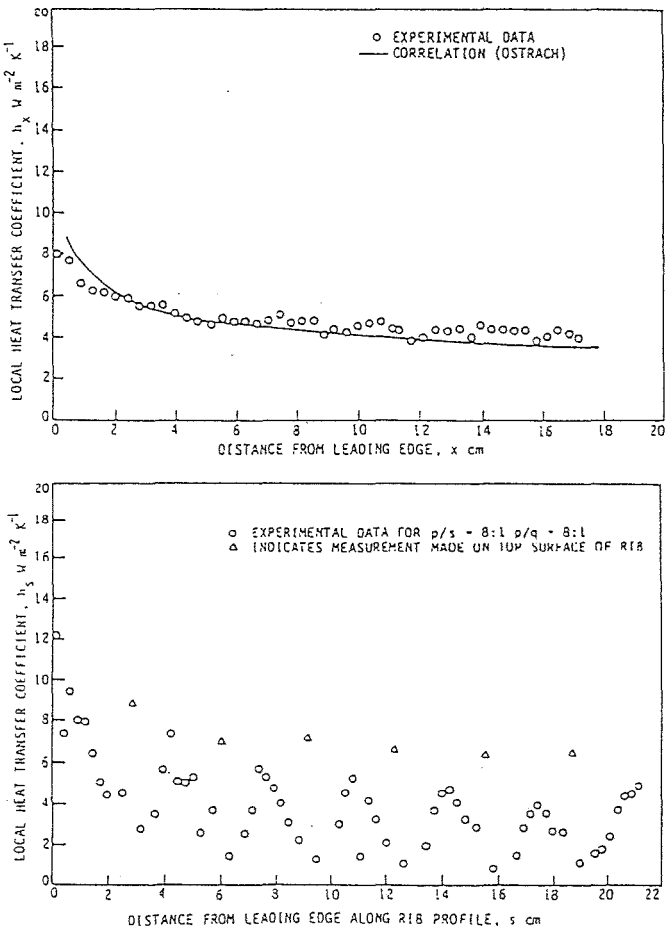

FIGURE 2.34 Local heat transfer coefficient (a) for a vertical isothermal plain plate, (b) for a vertical plate roughened by square ribs (P/e=8).

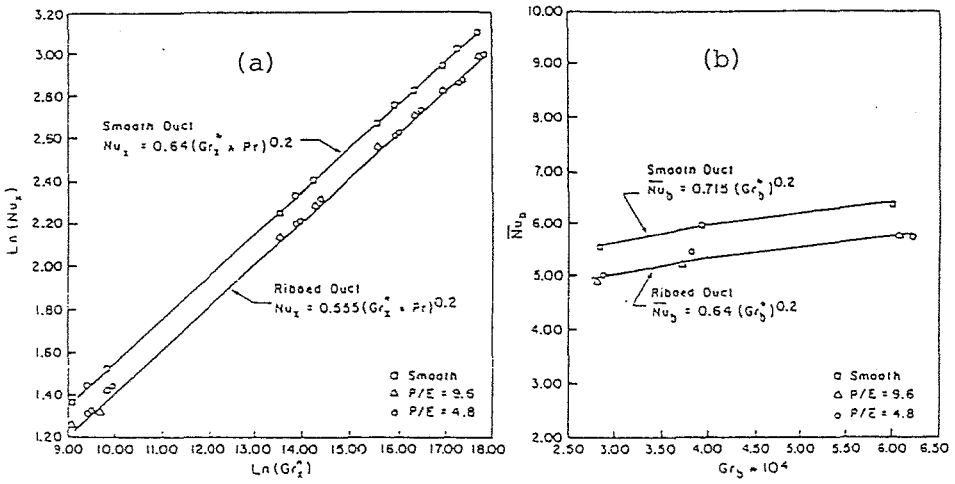

FIGURE 2.35 Average Nusselt number for smooth and ribbed vertical channels: (a) Uniform Wall Temperature, (b) Uniform Heat Flux.

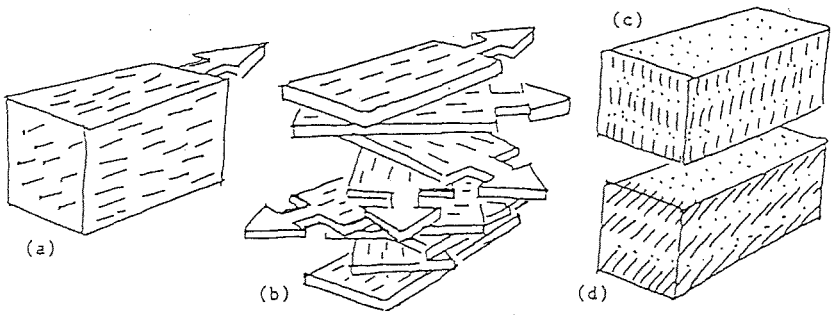

FIGURE 2.36 Liquid crystal mesophase structures: (a) Nematic, (b) Cholesteric, (c) Smectic A, (d) Smectic C.

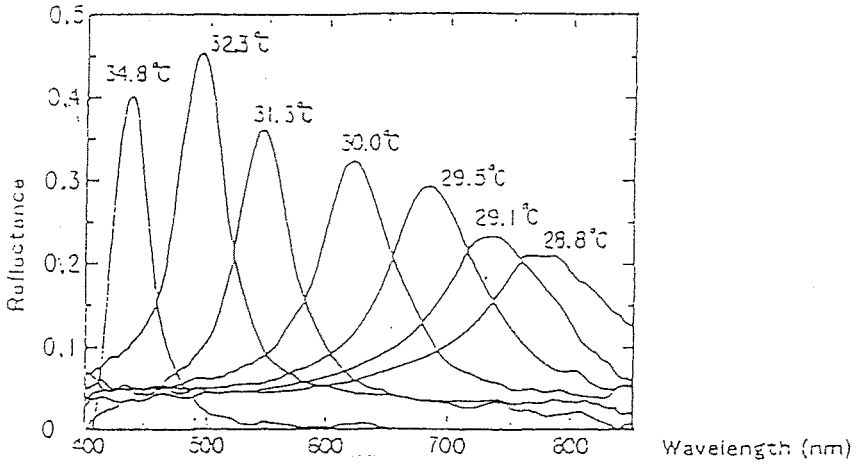

FIGURE 2.37 Typical distribution of intensity of reflected light versus the wavelength, showing the variation of the spectrum with temperature for a given liquid crystal.

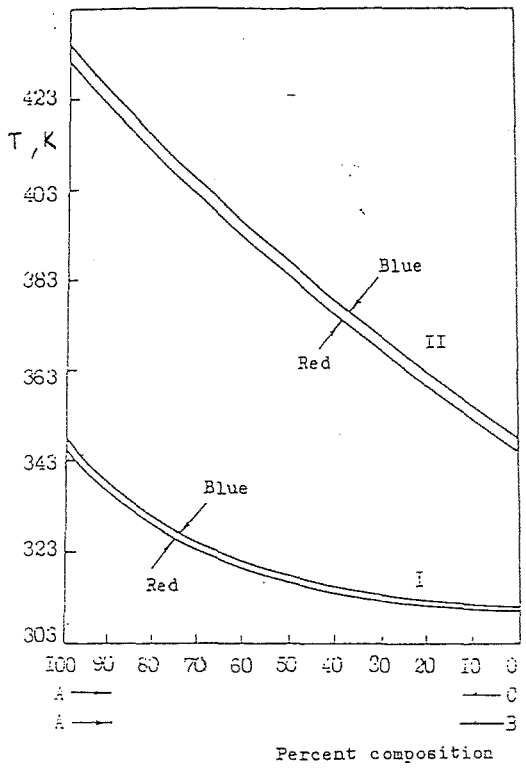

FIGURE 2.38 Temperature dependence of selective light reflection of cholestrol ester mixtures: I. cholesterylnonanoate (A)- cholesterylnonyloxibenzoate (B); II. cholesterylnonanoate (A)- cholesteryloleate (C).

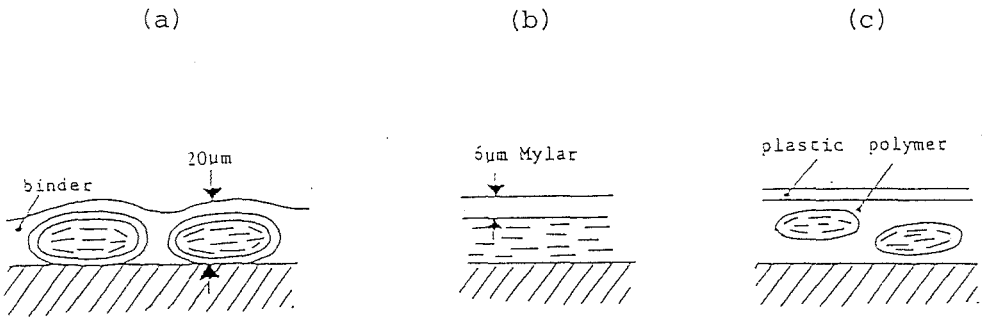

FIGURE 2.39 Methods of applying liquid crystal for temperature measurement: (a) encapsulated material, (b) neat material with a plastic film, (c) polymer dispersion.

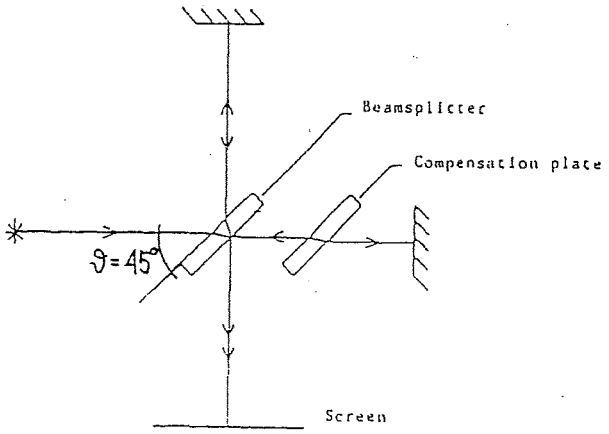

FIGURE 2.40 Schematic of the Michelson interferometer.

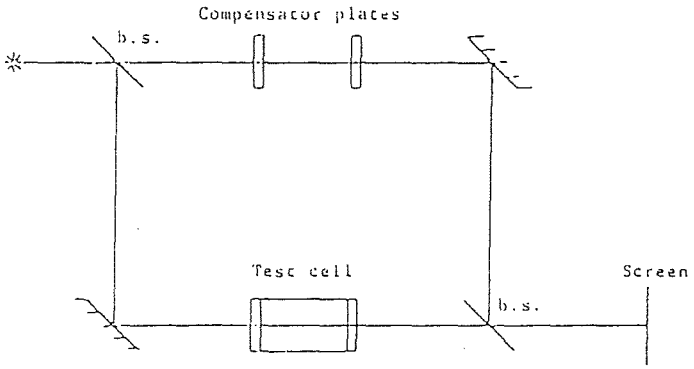

FIGURE 2.41 Schematic of the Mach Zehnder interferometer.

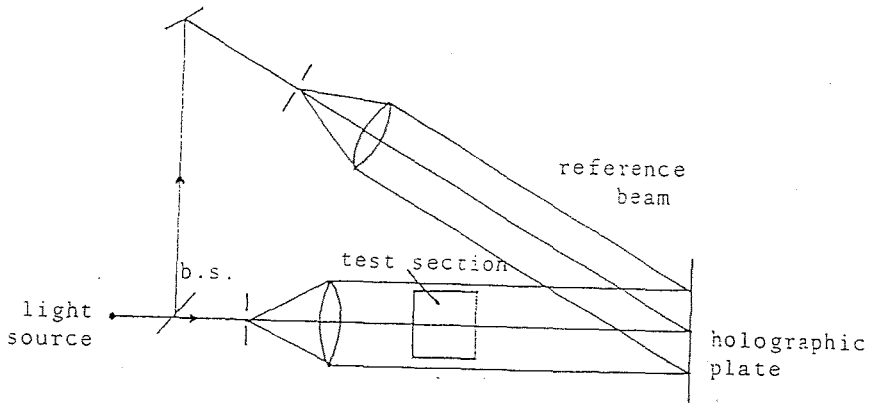

FIGURE 2.42 Schematic of conventional holographic interferometer.

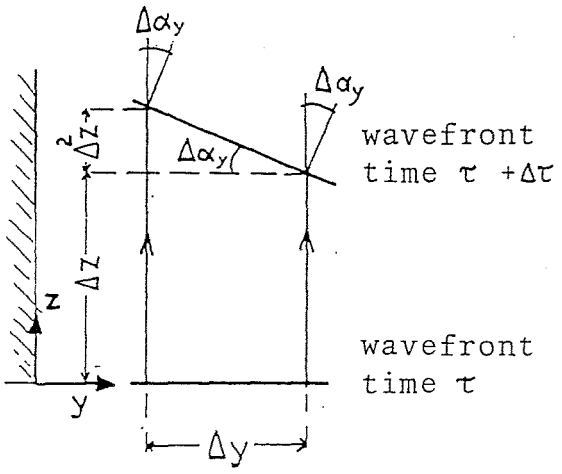

FIGURE 2.43 Bending of light rays in an inhomogeneous medium due to the "schlieren" effect.

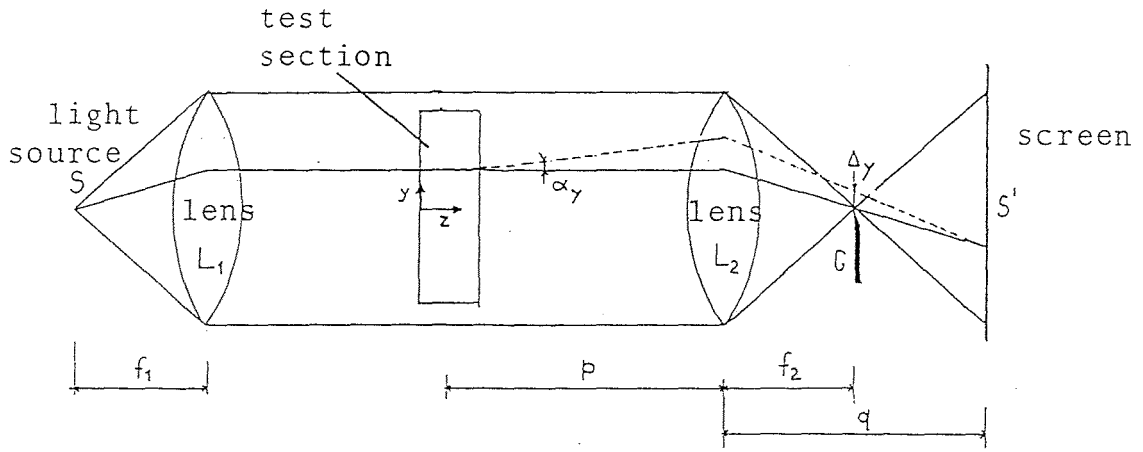

$\alpha_y \simeq \Delta'/p$

$\beta \simeq \Delta'/f_2$

$\gamma \simeq \Delta'/q$

$\alpha' = \beta - \gamma \simeq \Delta'\left(\frac{1}{f_2} - \frac{1}{q}\right) = \frac{\Delta'}{p} = \alpha_y$

$\Delta_y \simeq f_2\alpha' = f_2\alpha_y$

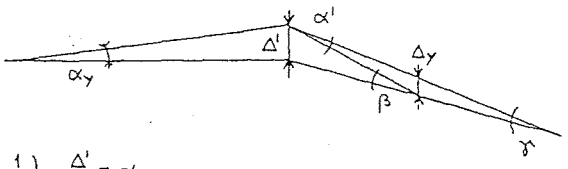

FIGURE 2.44 Standard schlieren system (Töpler system) using lenses.

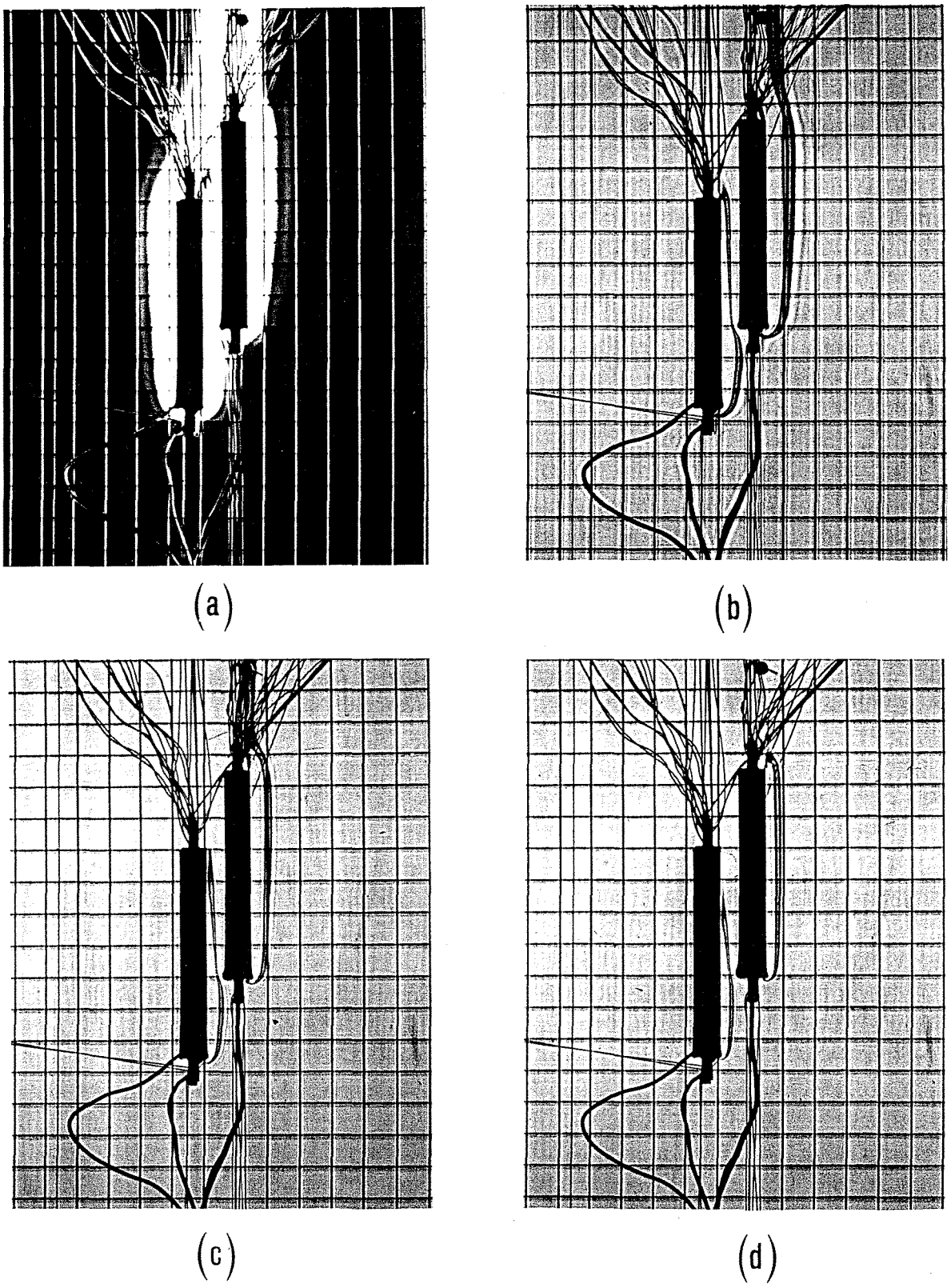

FIGURE 2.45 Schlieren images (obtained by the "Z" schlieren arrangement, focal filament method) of two vertical staggered plates cooled by air in free convection. From (a) to (d): the focal filament is progressively shifted on the focal plane of the schlieren head.

3. LIQUID CRYSTAL EXPERIMENTS IN RIB-ROUGHENED CHANNELS

The liquid crystal technique was employed to study experimentally **forced convection** heat transfer in rib-roughened channels. Two different configurations of ribbed channels were considered. For comparison purposes, a set of tests was also performed in a channel without ribs (flat plate case).

3.1 The apparatus

Liquid crystal experiments were performed in a small-scale, low-turbulence wind tunnel. Basically, the experimental apparatus includes: (a) the wind tunnel, (b) the test section, (c) instrumentation to record fluid velocity, temperature and liquid crystal images, (d) the image processing system.

The main components of the experimental apparatus were designed by Stasiek (1992). Some modifications to the apparatus, and to the operating procedure, have been applied in the course of this study.

3.1.1 The wind tunnel

The tunnel is an open cycle configuration with exhaust air discharged to ambient at the exit section. A schematic drawing of the wind tunnel is shown in Fig.3.1. Ambient air is drawn into the tunnel by a centrifugal fan at a controlled flow rate by adjustment of inlet valves. An electric heater placed downstream of the entry section enables the air flow to be heated to the desired temperature. After a settling chamber with diffusing screens and honeycomb, the air flow enters the developing section. This has a rectangular cross-section (56 mm height x 224 mm width) and extends in length for about twenty hydraulic diameters in order to establish fully developed conditions (or very close to them) in the flow approaching the test section. The lateral walls, made of perspex, have a thickness of 8 mm.

3.1.2 The test section

The test section is a tunnel having the same passage area as the developing section. A schematic drawing and a photograph of the test section are shown in Figs.3.2 and 3.3, respectively. The lower plate of the test section, termed the **test plate**, can be cooled or heated by an impinging jet of water coming from a thermostatic bath. Therefore, a net

heat transfer rate can be obtained across the lower plate between the water and the air flow. Conversely, the other three plates forming the test section are assumed to be practically adiabatic. The test plate and the other walls of the test section are made of perspex with a thickness t of 8 mm. After the test section, the air flow rate passes through a redevelopment section before being exhausted to the atmosphere.

3.1.3 The instrumentation

The tunnel is instrumented with copper constantan (type T) thermocouples, calibrated to within ±0.1 K. One thermocouple is placed at the inlet of the test section, at midheight, 2 cm from the side wall in order to measure the air temperature. Additional thermocouples, able to be moved vertically, have been employed in order to check temperature gradients in the air flow, as will be shown later.

Two to four thermocouples have been used to measure the water-side wall temperature of the test plate. The water, whose temperature is controlled by a thermostatic bath to within ±0.025 K, exchanges heat with the bottom surface of the test plate. Owing to the nature of the heat transfer (forced convection of water), heat transfer coefficients are very high; thus a condition of uniform wall temperature is expected on the water-side surface of the test plate. This temperature can be varied over a wide range by selecting the appropriate value on the thermostatic bath panel control.

The air-side surface temperature of the test section lower plate was measured by using a 0.15 mm liquid crystal sheet (Fig.3.4). The sheet, manufactured by Liquid Crystal Devices Inc., consists of a polyester film with a substrate of black paint over which a 0.01 mm liquid crystal layer is deposited. Encapsulated liquid crystals in the cholesteric phase were used in this study. The event temperature range is about 31 to 33 °C. The liquid crystal sheet was attached to the air-side test plate using adhesive tape. Care was taken to avoid impurities and air bubbles being sandwiched between the perspex plate and the sheet, thus ensuring a perfect thermal contact. Four thermocouples were sited below the liquid crystal layer, embedded in small grooves to ensure the liquid crystal sheet remained planar. This was in order to allow "in situ" calibration of the liquid crystal sheet.

All thermocouple signals were read by a Keithley millivoltmeter giving the value of the electric potential difference between the selected probe

and the reference 0°C junction. This value was then converted to Celsius degrees using the Standard Tables of Conversion for type-T thermocouples.

The colour patterns exhibited by the liquid crystal sheet during experiments were recorded by a RGB video camera and analysed by an image processing system. The video camera was placed about 0.5 m above the test section, focusing on the liquid crystal sheet. Four 100 W lamps were employed to light randomly the test section. The lamps were switched on just a few seconds before the acquisition of a given image (and switched off immediately after) in order to prevent radiant heat exchange.

Finally, the centreline velocity of air at the inlet of the test section was measured by a Pitot tube connected to a digital micromanometer. For the lowest air flow rate, a precalibrated hot-wire anemometer was used.

3.1.4 The image processing system

The image processing system (schematically shown in Fig.3.5) includes a PC386 equipped with a 512x512 pixels, 8 bits (256 grey levels) Colour Frame Grabber board DT2871 and an auxiliary Frame Processor DT2858, a 19" colour display and a colour laser printer. The video input section of the frame grabber incorporates a 10-MHz RGB/HSI (Red Green Blue / Hue Saturation Intensity) converter for transforming in real time digitised pixel values representing weighted combinations of the primary colours (RGB) into new values representing hue, saturation and intensity (HSI). The characteristic value of each HSI component ranges between 0 and 255 (the limit for 8 bits). Among these distinct colour attributes, the hue (or chromaticity), which represents the spectral colours present, can be related to the temperature. In particular, in a narrow range of hue values, the relationship between the hue exhibited by the liquid crystal sheet and its surface temperature can be determined during calibration experiments. The knowledge of this empirical relationship allows one to reconstruct, from the hue field the temperature field or, as performed in this work, to segment the colour image in order to select regions having a given value of hue to which corresponds a given value of surface temperature.

The photograph of Fig.3.6 shows the image processing system working during the analysis of an experimental test.

3.2. The geometry

The aim of the study was to determine the heat transfer

characteristics in a channel with rib-roughened walls and to assess whether a similar geometric configuration enables significant heat transfer improvements to be reached with respect to a reference plane-wall channel.

All experiments were conducted by arranging the following boundary conditions. At the inlet of the test section, a uniform profile for air temperature and a fully-developed profile for air flow were imposed. Departures from these conditions occurred during some experiments, and will be discussed later. As previously mentioned, the air flow exchanges heat with the test plate in the test section, maintained at **uniform wall temperature** on its bottom surface (water-side).

3.2.1 The flat plate

A first set of experiments was arranged by studying the heat transfer characteristics for a **flat plate** (actually the test plate previously described in an unchanged state) cooled by air in forced convection (Fig.3.7). Even though theoretical, numerical and experimental results are available in the literature for this well known configuration, it was believed to be of great importance to carry out these experiments using the same technique and operating procedure as the tests in the presence of ribs. In fact the flat plate results can be compared with data in the literature to provide further checks on the experimental technique and used to normalise the ribbed channel results.

3.2.2 The rib-roughened channels

Two different configurations of ribbed channels were studied. In the first case, depicted in Fig.3.8, a plate, having a series of five parallel square-ribs attached at regular intervals, was vertically mounted on the test plate. With such a configuration, the ribbed surface acts as a promotor of turbulence in the air flow in order to produce large heat transfer coefficients on the test plate, with respect to the flat plate configuration. The dimensions of the ribbed plate are as follows: height and length (in the main direction of flow) of ribs: e = 7.9 mm, rib pitch: P = 56.9 mm, inter-rib spacing (P-e) = 49 mm, distance from the side flat walls S'= 107.5 mm (rib-pitch to rib-height ratio P/e=7.2, ribbed-channel width to rib-height ratio S'/e=13.5). The rib-roughened plate is made of perspex. This channel configuration will be termed **CONFIGURATION R1**.

Another set of experiments was conducted for a different ribbed channel configuration, in which five ribs were attached, at regular

intervals, directly on the test plate, as shown in Fig.3.9. The ribs are of square section (of dimensions e=7.9mm) with a pitch P = 56.9 mm, (pitch-to-height ratio P/e=7.2, ribbed channel height to rib-height ratio S/e=7.1). As in the previous case, the ribs create flow separation and heat transfer enhancement, but the features of flow and thermal fields are obviously expected to be largely different. This second ribbed configuration will be termed **CONFIGURATION R2**.

3.3. Operating procedure

The operating procedure followed to carry out the experiments is practically independent of the specific geometric configuration studied. The first step consists of the calibration of the liquid crystal sheet, i.e. the determination of the relationship between hue and temperature. After that, experiments can be performed by selecting convenient values of air flow rate, air temperature and water temperature. The image processing analysis forms the last stage of each experimental test.

3.3.1 The liquid crystal calibration

The calibration of a liquid crystal sheet identical to that employed in the forced convection experiments was performed using the apparatus designed by Stasiek (1992) and schematically depicted in Fig.3.10.

The apparatus consists of a brass plate (the calibration plate) along which a constant surface temperature gradient is imposed, by cooling one end with a circulation of water and heating the opposite end (Joule effect). The liquid crystal sheet is attached to the surface of the brass plate. Several thermocouples embedded in the brass plate (as close as possible to the LC layer) enable the temperature distribution on the plate to be measured. The brass plate / LC sheet assembly is covered by a perspex plate and uniformly illuminated by four 100 W lamps in order to reproduce the same optical conditions as those present in the experiments. When a proper temperature gradient along the brass plate is imposed, the LC sheet displays colours related to its local surface temperature distribution measured by the deployed thermocouples. The colour pattern is then recorded by the RGB video camera placed above the calibration plate and analysed by the image processing system in order to map the hue distribution (see Fig.3.11, bottom). This procedure enables the relationship to be determined between hue and temperature, for the specific LC sheet and lighting

conditions.

Since the colour-play interval occurs in a narrow range of temperature (for this work about from 31 to 33 °C), only one colour band was considered during experiments. The selected band corresponds to the hue range between 45 and 55 (light green). For this range of hue, the temperature after calibration turned out to be 32.1°C± 0.1°C, as explained in detail in Appendix A1. This temperature will be termed the **LC reference temperature**. Further details about how experiments were conducted using a one-colour analysis are given in Appendix A1.

A further calibration test has been performed "in situ", i.e. by checking the hue/temperature relationship directly during a forced convection experiment. The "in situ" calibration consists of imposing the same temperature for the air and water flows. Once steady-state conditions are reached, the test plate assumed a uniform temperature and the LC sheet exhibits a unique colour. In Fig.3.11 (top) the RGB image of the test plate (with ribs mounted vertically, config. **R1**) is depicted, for air and water at 32.1 °C ±0.1 °C. The window opened in the optical field has been processed and colours segmented in order to show regions whose hue is between 45 and 55. As expected, practically the entire processed field exhibits the same hue range, thus confirming the result obtained by the "calibration plate" experiment.

3.3.2 The experimental tests

The experimental apparatus was designed to study forced-convection heat transfer in air from a plate (the test plate) whose temperature is controlled by an impinging water jet at the opposite side. Basically, each experiment requires the following steps:

(1) selecting a flow rate of air through the wind tunnel, by adjusting the setting of the valves;

(2) heating the air, by supplying power to the heater up to the desired temperature, noting that this step is omitted when working with air at ambient temperature;

(3) waiting for thermal steady-state conditions in the development section (up to 2-3 hours may be required owing to the thermal inertia of the tunnel walls);

(4) heating or cooling the test plate by impingement of water at controlled temperature;

(5) waiting for thermal steady-state conditions in the test section

(generally 5 to 30 minutes);
(6) recording values of air flow velocity and of temperature by the thermocouples deployed;
(7) recording and storing the colour pattern image shown by the LC sheet (lamps are switched on a few seconds before and switched off a few seconds after the image acquisition).

As discussed in Appendix A1, only one colour band is used: it gives the locus of points characterised by a given Nusselt number value. In order to obtain the contours of lines at constant Nusselt number, two different procedures can be followed:
(8a) **procedure ATF** (Air Temperature Fixed): varying the temperature of the impinging water and keeping the air temperature fixed; after a new water temperature value is selected, previous points (5-6-7) have to be repeated;
(8b) **procedure WTF** (Water Temperature Fixed): varying the temperature of the flowing air and keeping the water temperature fixed; for each value of air temperature selected points (5-6-7) have to be repeated.
The first procedure (8a) was preferred mainly for two reasons: (i) varying the temperature of air leads to modifications in Reynolds number (based on conditions at the inlet of the test section) since kinematic viscosity changes with temperature; (ii) the accuracy of results generally improves when both air and water temperature are far from the LC reference temperature. Hence the best results are achieved by varying the water temperature rather than the air temperature.

After a sufficient number of image acquisitions have been performed (either under procedure 8a or 8b), each image is processed and segmented. The segmented images (representing the pattern of the reference temperature for different wall-to-air temperature differences) are then overlapped by a proper algorithm which assigns to each of them a conventional colour. The final result is a pattern of lines at different colours with each colour corresponding to a given Nusselt number value. In Fig.3.12 the image processing steps are sequentially shown: from the "true colour" LC image, recorded for a given experiment (top), only the reference colour band (hue 45-55) is extracted (middle). Changing for instance the water temperature (i.e. the local Nusselt number) leads to a change in the reference colour band pattern. The "false colour" image (bottom) resulted from overlapping one by one the reference band patterns for the selected water temperature values: each colour corresponds to a different Nusselt number.

3.3.3 The direction of the heat flux

As previously described, the experimental apparatus enables both the water to be cooled or heated as well as the air to be heated or not, for specific experimental purposes. Therefore, experiments can be conducted by imposing a heat transfer rate (across the test plate) either from the water to the air flow or vice versa.

In the first case, the water is heated up to a given value (by selecting a proper temperature value on the thermostatic bath panel control) while the air is maintained close to the ambient temperature. It should be noted that, owing to the passage through the fan, ambient air undergoes a rise in temperature of about 7-8 K, at the steady state, even if the electrical heater is switched off. Under this procedure, termed **HFU** (Heat Flux Upward), the heat flux is directed upward from the bottom surface of the test plate, against which hot water impinges, to the top surface, cooled by flowing air.

In the second case, the air is heated up to a given value by varying the power supplied to the heater, while the water is maintained at a lower temperature value. The heat flux, under this second procedure (termed **HFD** - Heat Flux Downward), is directed downward across the test plate, from the air to the water.

The two procedures (HFU and HFD) present advantages and disadvantages. The HFD allows more brilliant and contrasting colours to be obtained. Unfortunately, heating the air flow up to temperature values suitable for establishing an accurately detectable downward heat flux (say 40 °C, for instance) leads to nonuniformities in the air temperature profile at the inlet of the test section. In fact, even though the perspex walls of the tunnel are poor heat conductors, a non-negligible heat transfer is transferred from the flowing air to the ambient air through the tunnel side walls, accompanied by temperature gradients near the boundaries. The presence of a non-uniform temperature profile in the air flow entering the test section is disadvantageous for the following reasons: (i) the measurement of air temperature in a single spot is no longer sufficient but vertical and spanwise temperature profiles are required to evaluate an average value of inlet air temperature; (ii) the reproducibility of tests is very critical: even a 2-3 K change in ambient temperature due to external climatic conditions renders almost impossible the repetition of an experiment since the air temperature profile at the inlet will not be the

same; (iii) the presence of temperature gradients in air could affect, or make more complicated, the interpretation of results; (iv) a flat temperature distribution at the inlet is a standard thermal boundary condition for this kind of problem and enables comparisons with computational data to be made more easily.

In order to reduce and control the temperature nonuniformity at the inlet of the test section, the development section has been thermally insulated by means of a 20 mm layer of polystyrene and a thermocouple has been located between the perspex wall and the polystyrene, as depicted in Fig.3.13.

During the majority of experiments conducted under the HFU procedure, differences in temperature values recorded by thermocouples A,B, and C (see Fig.3.13) were confined to within 2 K, with a temperature difference between flowing and external ambient air of 7-8 K. If one accounts for the thermal resistance of the perspex wall, a maximum of 1.5 K in air temperature nonuniformity generally occurred. Comparisons performed between tests with the same input data and inlet air temperature nonuniformities in the range 0-1.5 K did not give appreciable differences in results.

In spite of the careful thermal insulation of the developing section, air temperature gradients occurring under the HFD procedure still remained high, reaching even 6-7 K when the flowing air temperature exceeds by 25 K the external ambient air temperature. Therefore, the procedure HFD was progressively abandoned in the course of experiments.

3.4. Results and discussion

As discussed in Appendix A1, for each geometric configuration investigated, the input parameter is expressed by the Reynolds number of the air flow. For a given air flow rate, the local Nusselt number distribution on the test plate can be evaluated. An additional output variable will be used in the presentation of the results: the heat transfer enhancement factor N, which represents the ratio between the ribbed channel Nu value and that for the flat plate at the same Reynolds number.

Heat transfer results will be presented in the following sequence:

a) flat plate configuration;

b) rib-roughened channel **R1**;

c) rib-roughened channel **R2**.

Most of the experiments have been conducted by imposing an upward heat

flux (HFU procedure) and by mapping the Nusselt number contours keeping the air temperature fixed and varying the water temperature (ATF procedure).

For the cases involving the flat plate configuration (a) and the rib-roughened channel **R2** (c), comparisons of experimental results with data reported in the literature will be also presented and discussed.

3.4.1 The flat plate

The Nu distributions along the main direction of flow are reported in Fig.3.14 for Re=3500-20000. As expected, the higher values occur close to the entrance region. Downstream, the thermal boundary layers become thicker and heat transfer coefficients,hence Nu values, decrease. The length of the test section (262 mm, about 3 times the tunnel hydraulic diameter d=8.96cm) does not enable thermal fully developed conditions to be reached for any Reynolds number. In fact, the thermal field develops after a length of about ten times the hydraulic diameter for Re>2000 (Bejan, 1993). It is apparent from graphs plotted in Fig.3.14 that Nu values are far from the asymptotic limits expected for the largest x values. However, some conclusions may be drawn on the basis of values recorded at distances sufficiently far from the entrance (x/d=2). The measured Nu values are reported in Table 3.1 and compared with data reported in the literature. In particular, experimental results were compared with the following data:

(i) $Nu_{fd} = 0.023\ Re^{0.8}Pr^{n}$, Dittus-Boelter formula for channels with Re>2500, x/d>60 and thermal fully developed conditions (n=0.4 when the fluid is heated),

(ii) $Nu_x = Nu_{fd}(1+(d/x)^{0.7})$, Thomas, 1980, valid for circular tubes with Re>2500 and accounting for entrance effects in the range 2 <x/d<20 (Nu_{fd} is the Dittus-Boelter value),

(iii) $Nu_{x,t}$, derived from the theoretical solution for turbulent heat transfer in a parallel plate channel with one plate uniformly heated and the opposite plate adiabatic (Hatton and Quarmby, 1964) obtained for Re=7100, 73700, and 495000 (Pr=0.7) and here extrapolated down to Re=3500.

Finally, it should be noticed that the Reynolds number, from which (i), (ii), and (iii) Nu values depend, are based on the **mean** velocity. Therefore Re numbers were recast before the comparison according to a common definition. As emerges from inspection of Table 3.1, Nu values measured at x/d=2 greatly exceed fully-developed values Nu_{fd} since the thermal field is far from the fully-developed condition. The comparison between experimental results and literature data Nu_x and $Nu_{x,t}$ is rather

satisfactory for the highest Re values, especially for Re=20000. In this case, the conditions for the comparison are the most favourable, as the flow is fully turbulent and the experimental uncertainty is low. Conversely, when the Reynolds number falls in the transitional regime (Re=3500-6000), both experimental and data from literature are affected by large uncertainties.

	Nu (exp.) x/d=2	Nu_{fd}	Nu_x x/d=2	$Nu_{x,t}$ x/d=2
Re = 20000	80	51.3	82.9 (+3.6%)	72.5 (-9%)
10000	59	29.8	48.1 (-18%)	45.5 (-23%)
6000	47	19.6	31.7 (-33%)	32.0 (-32%)
3500	36	12.7	20.5 (-43%)	24.0 (-33%)

Table 3.1

Comparison between experimental results and data from literature for the flat plate

3.4.2 The rib-roughened channel R1

The present configuration involves the rib-roughened plate vertically mounted on the test plate (Fig.3.8). The ribs, together with the plate to which they are attached, act as obstacles for the air flow, thus promoting vortex formation and increased levels of turbulence. The strong modification in fluid flow leads to different and generally improved conditions of heat transfer, with higher heat transfer coefficients as compared with the flat plate case due to the effective mixing of flowing air.

Numerous preliminary tests were performed for this geometry either changing the direction of heat flux (HFU or HFD procedure) or changing the procedure for displaying the Nusselt number contours (ATF or WTF procedure). Examples of "true colour" LC images, for HFU and HFD procedures are reported in Figs.3.15 and 3.16. Each figure shows three images of the test plate (from rib C to rib E, see Fig.3.8) obtained for the same Reynolds number (Re=20000) and different values of the water temperature. Figure 3.15 refers to upward heat flux conditions (HFU), the water

temperature being progressively *decreased* from the top image to the bottom image. Figure 3.16 reports the colour patterns for the downward heat flux conditions (HFD), the water temperature being progressively *increased* from the top image to the bottom image. In Fig.3.17 the lines at constant Nusselt number are reported for the same Reynolds number (Re=20000) and different directions of heat flux. The same Nusselt number values are displayed by the same colour on both pictures; this makes it possible to estimate the difference in results due to the different procedures. The patterns of lines appear to be qualitatively unaffected by the specific procedure followed, but noticeable differences emerge from the quantitative point of view. The largest differences (20-30%) occurred for the lowest Nusselt number, in the space between two adjacent ribs and their baseplate. It is believed that the different air temperature profile at the inlet of the test section is mainly responsible for the poor agreement. The non-uniform air temperature profile at the inlet occurring for the HFD procedure introduces additional uncertainty in the mean air temperature estimate and probably affects the distribution of heat transfer coefficient. As further evidence of this explanation, the disagreement between tests performed with different directions of heat flux markedly increases as the Reynolds number decreases. In fact, decreasing the flow rate leads to larger temperature nonuniformities in air flow before it enters the test section.

Once the direction of heat flux across the test plate is chosen (the HFD procedure was abandoned since it is considered to be less accurate), further experiments were performed either with ATF (Air Temperature Fixed) or WTF (Water Temperature Fixed) procedures. In principle, the two techniques should enable the same Nusselt number patterns to be obtained for a given air flow rate. Actually, differences in results may appear owing to the dependence of thermophysical properties of air on temperature and for the small temperature difference between liquid crystals and air when the WTF procedure is selected. As discussed in Appendix A1, this causes poorer accuracy especially for the highest Nu values. Therefore, the ATF procedure, coupled with the Heat Flux Upward procedure, was followed for all the following experiments. Once established to be the more reliable procedure to follow in the experiments, reproducibility checks were performed by repeating the same experiment under identical input conditions. Examples of reproducibility tests are displayed in Figs.3.18-3.21. Figures 3.18, 3.19, and 3.20 show "false colour" images for

two identical tests and for Re=20000, 10000 and 3500, respectively. In Fig.3.21 the Nu values for pairs of identical tests are superimposed and the reproducibility directly checked. Repeatability in Nu values is found to be in the 0-10% range which is considered to be satisfactory for the experiments.

After the preliminary experiments were completed, the main body of experimental runs was performed, again in the Re range between 3500 and 20000. Attention was focused on heat transfer both from the entrance region (close to the first two ribs designated A and B in Fig.3.8) and from the "developing" region, through which a fully developed thermal field should be approached. Visual presentation of tests performed by monitoring the whole test plate (with all the five A-E ribs) is given in Figs. 3.22-3.24 as a combination of true-colour images (recorded for different values of water temperature and the same flow rate) and the false-colour image, obtained by processing a set of true colour images and representing the Nusselt number line patterns. Each figure refers to a different Reynolds number, that is Re=20000 (Fig.3.22), Re=10000 (Fig.3.23), Re=6000 (Fig.3.24), and Re=3500 (Fig.3.25). Generally speaking, when the whole test plate is framed by the video camera, the resolution after image processing and segmentation is poor. Besides, some spots of the optical field (the regions immediately upstream of the first and second ribs and downstream of the fourth rib), are shadowed by the ribs themselves making the colour recording not feasible in these zones. In order to overcome these difficulties, some tests were repeated by alternatively focusing the first half (from rib A to rib C) and the second half of the test plate (from rib C to rib E). The Nusselt number contours obtained for the two halves of the test plate were eventually matched in order to attain an accurate map over the whole ribbed region. False colour images obtained from these experiments are presented in Figs. 3.26, 3.27, and 3.28, for Re=20000, 10000 and 6000, respectively.

Data are summarised in Figs. 3.29-3.32, where lines of constant Nu values (manually extracted by the false colour images previously shown) are reported for the whole Reynolds number range investigated (Fig.3.29, Re=20000, Fig.3.30, Re=10000, Fig.3.31, Re=6000, and Fig.3.32, Re=3500). The shape exhibited by the Nusselt number lines is similar for all Re values investigated, even though the absolute value tends obviously to increase as the air flow rate is increased. Entrance effects are dominant along the first half of the test plate, while in the second half heat

transfer coefficient contours tend to repeat themselves at regular intervals, equal to the rib pitch.

Results are now discussed in detail. At first, attention is focused on the entrance region. Here the strongest modifications in flow characteristics are expected: the fully developed velocity profile is destroyed as the inlet air flow impinges against the first rib and recirculating structures are likely to form downstream of the obstacle. As a result, a region characterised by high heat transfer efficiency is concentrated near to the first rib top where vortex structures are generated. In contrast to this, flow separation leads to reduced heat transfer rates from the space confined between the first and second ribs. Here, a minimum value of Nu is reached near to the rib baseplate, just in the midspace between ribs. Closer to the main airstream, Nu values tend to increase showing profiles almost parallel to the rib baseplate. Downstream of the second rib, the inter-rib region becomes suddenly more effective, from the heat transfer point of view, near to the forward-facing rib wall, while poorer heat transfer conditions are established near the rear-facing rib wall. It is interesting to notice that heat transfer from regions immediately surrounding the third rib (C) is more intense than that from regions around the previous rib (B) as though the main airflow, after the impingement against the first rib (A), had "by-passed" the second rib (B). This phenomenon occurs for each Reynolds number investigated. Downstream of the third rib (C), the flow gradually approaches fully-developed conditions and a periodic pattern of heat transfer coefficient distribution is established.

Further features can be discerned from Figs.3.33 and 3.34, where heat transfer results are presented in a different format. Figures refer to two different Reynolds numbers (Re=20000 and Re=6000) and present Nu and N values along the spanwise y-coordinate (normalised by the rib-height e) at different axial locations x. It is worth recalling that N values denote the extent of heat transfer enhancement relative to a flat plate at the same spot and in the same flow rate and heating conditions.

When the Reynolds number is high (Re=20000, Fig.3.33) large heat transfer coefficients as well as large increases with respect to the flat plate are obtained. For instance, near to the third rib C, Nu exceeds by 2.5 times the value recorded, at the same spot, for the unribbed flat plate ($N \approx 2.5$). The comparison of N profiles along lines **a**, **b**, and **e** is of particular interest since these lines have a spacing equal to that of the

ribs. The highest N values are measured along the **b**-line (which is aligned with the forward-facing wall of third rib C), near to the rib itself. The N profile along the **a**-line (one rib-pitch upstream of line **b**) has a different shape and even smaller values. As expected, only small differences are found between the N profiles along the **b** and **e** lines, since heat transfer coefficients around ribs here are similar. Comparisons between measurements along **c** and **f** (as well as **d** and **h**) lead to the same consideration. Nu values lower than those recorded for the flat plate (i.e. N<1) are recorded in the regions obstructed by the rear-facing walls of the ribs (see N profile along **g**-line for y/e<1) owing to the flow separation and weak fluid recirculation.

When the Reynolds number is low (Re=6000, Fig.3.34) the degree of heat transfer enhancement achieved by inserting the ribs seems to be reduced. Again, comparisons between profiles recorded at one-rib-pitch distance provide for quasi fully-developed thermal conditions achieved after the third rib (C).

3.4.3 The rib-roughened channel R2

A typical enhanced heat transfer geometry involves the use of ribs directly attached to the heat transfer surface as in Fig.3.9, the rib-roughened configuration R2. Owing to restrictions in time, for this geometry experiments were conducted for Re=20000 and 10000 only, again using the HFU-ATF combined procedure. Preliminary experiments showed a fall in repeatability to within the same range as the previous experiments for the R1 configuration (0-10% for Nu values). Two sets of true colour images are reported in Figs. 3.35 and 3.36 for Re=20000 and 10000, respectively. The false colour image at the bottom of each figure represents the final processing (segmentation and superimposition) of the above images. As expected, the iso-Nusselt number lines are fairly parallel to the ribs. Since the recorded optical field covers the central portion of the test section, in this region there is no evidence of significant three-dimensional effects.

The profiles of Nu values along the main direction of flow (x) are reported in the graph of Fig.3.37. The Nusselt number distribution for the flat plate Nu_{fp} (without ribs) at the same Reynolds number is also shown. The trends exhibited by Nu profiles have the same features for both the Reynolds numbers investigated. In the first module (region between first and second rib) the inter-rib region is characterised by low heat transfer

coefficients from the first rib up to the midspace between ribs. Nu values are approximately constant downstream of the first rib and then show a quasi-linear increase along the x coordinate. This increase leads to local heat transfer coefficients markedly higher than those for the flat plate. In the second module (region between second and third ribs) Nu begins to increase in a region close to the upstream rib and then reaches a maximum value in the inter-rib space. This value seems to remain unchanged as the downstream rib is approached. For the last two modules Nu values are found to increase linearly in the first half of the inter-rib region. For the second half, Nu values are practically constant. As expected, in the last two modules large heat transfer enhancement (with respect to the flat plate) is achieved, with the exception of the zones immediately downstream of the ribs, where the weak recirculation of fluid does not allow heat transfer to be effectively convected to the main airstream. The strong similitude in results obtained for the two last modules indicates that fully-developed conditions are close to being reached.

Finally, comparisons of results obtained by different non-intrusive techniques (including LC, liquid crystals) for the same geometry have been performed. The results presented in Fig.3.38 refer to ribbed surfaces with P/e=7-7.2 and to untransformed Reynolds numbers between $2 \cdot 10^4$ and $1.3 \cdot 10^5$. To facilitate the comparison, all Nusselt number data are normalised by the average value for the ribbed surface. Main differences in the local heat transfer results arise on the rib top ($1 < x/e < 2$) and in the inter-rib region at $x/e > 8$. In these regions the Nu distribution is Re-dependent (as demonstrated by Lockett and Collins, 1990) and thus the differences in Reynolds number can explain the disagreement. Moreover, for some published data the other geometric parameters affecting the phenomenon (e/d or e/S) are not given, therefore the comparison is not as reliable as it might be. Liquid crystal results, relative to the region between third rib C and fourth rib D for Re=20000 (see Fig.3.9, top), have been recast in dimensionless form using the average Nusselt number obtained by interpolation of data by Lockett and Collins (1990) at the relevant Reynolds number. The profile of normalised Nu number given by the liquid crystals, obtained in the x/e range from 4 to 8, is qualitatively in agreement with those obtained by other techniques in similar conditions. In Fig.3.39, absolute Nu values obtained by liquid crystal and interferometry (Lockett and Collins, 1990) for $Re \approx 20000$ are compared taking into account different definitions in Re; there is a common value of P/e equal to 7.2.

The ratios between the rib heights e and the untransformed equivalent diameters are close to each other (e/d=0.088 liquid crystals, e/d=0.066 interferometry). The profile given by LC analysis turned out to be higher than that from the interferometric analysis by 10-25 percent. The disagreement can be due to the slightly different thermal boundary conditions between the two experiments as well as to the experimental uncertainties associated with the two methods.

A comparison of the LC results with infrared thermography (IR) results obtained by Aliaga et al.,1994 is presented in Fig.3.40. Experiments conducted by the two different optical methods seem to be in good agreement, in spite of the different pitch-to-height ratio and Reynolds number. Firstly, it may be noted that thermal development occurs after the third rib. Then, the distributions of Nu along the first module for P/e=5 (IR) and P/e=7.2 (LC) show a uniform increase with x/e, owing to a trapped vortex between first and second ribs. Along the successive modules, while for P/e=5 (IR) the recirculating region continues to fit the whole space between ribs, for P/e=7.2 (LC) Nu reaches a nearly constant value probably due to the reattachment of the flow. For the largest P/e value (P/e=12, IR), the recirculating vortex is likely to occupy a reduced portion of the inter-rib space: as a consequence, a peak value of Nu (downstream of the second rib) is shown.

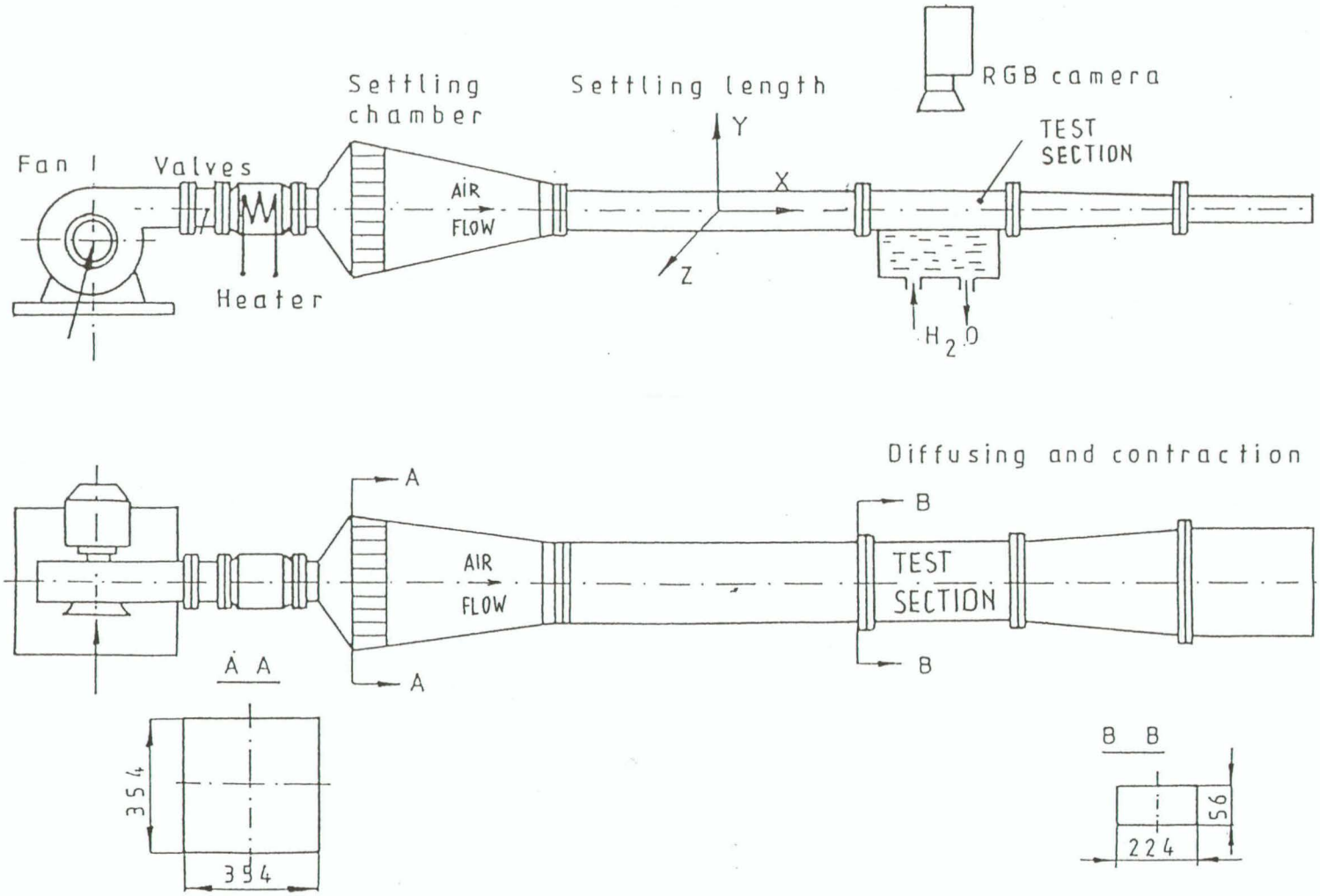

FIGURE 3.1 Schematic of the experimental apparatus for liquid crystal measurements.

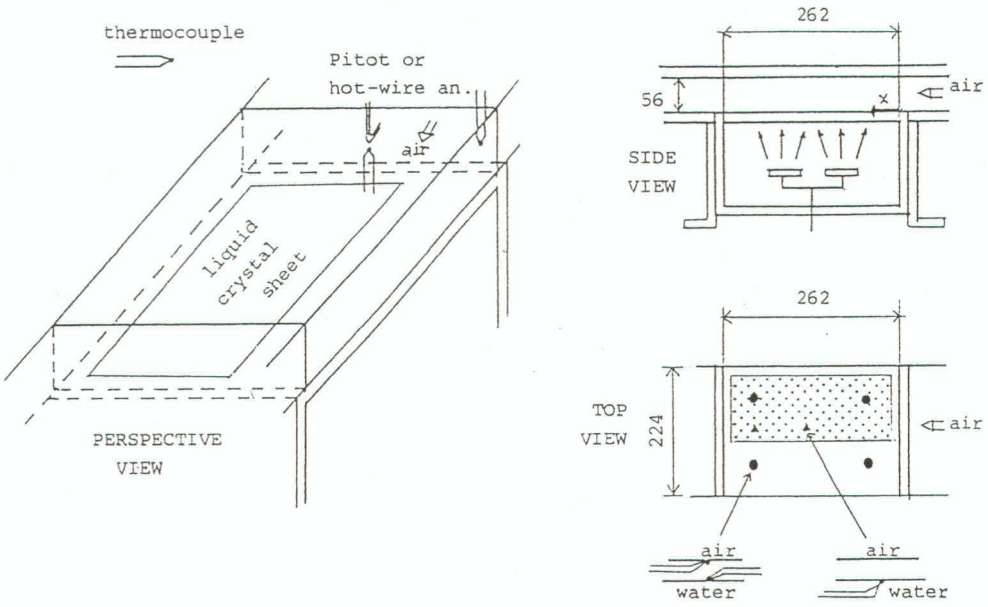

FIGURE 3.2 Schematic of the test section.

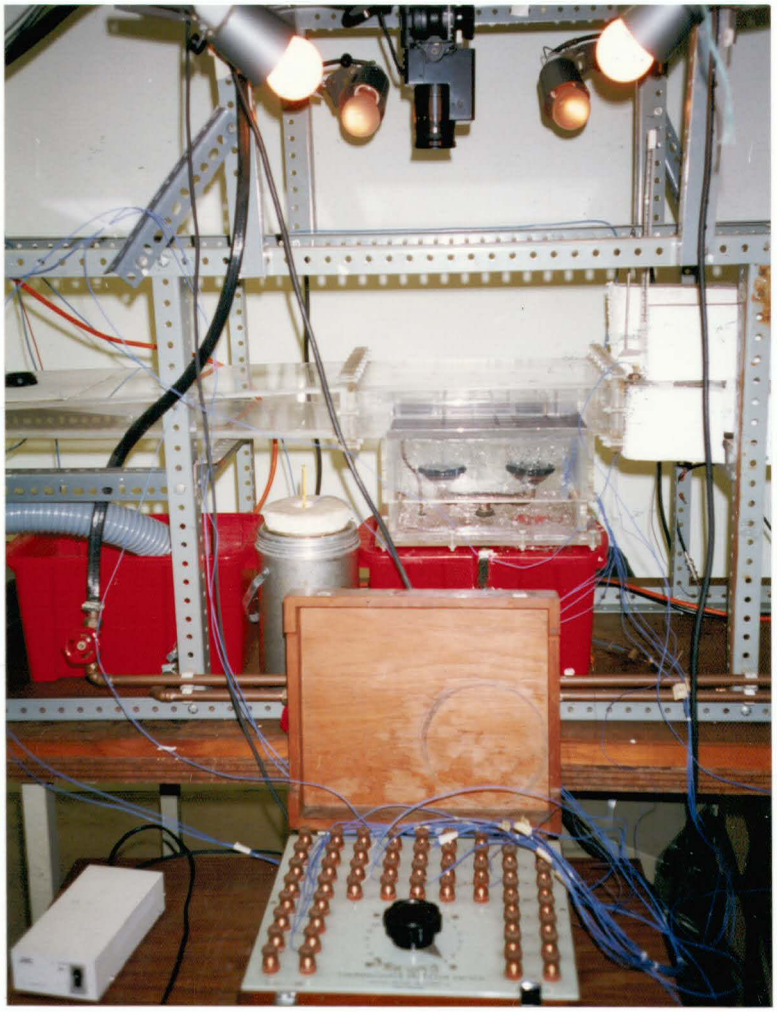

FIGURE 3.3 Photograph of the test section.

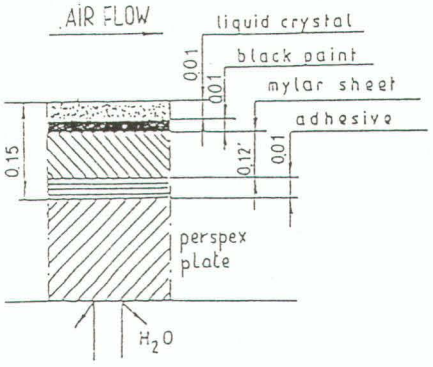

FIGURE 3.4 Section of the test plate (perspex plate and L.C. package).

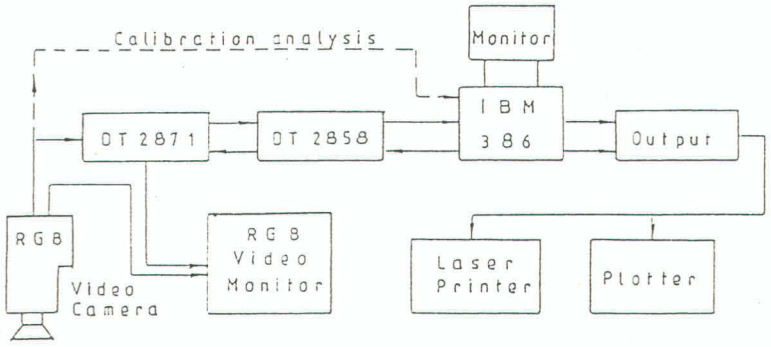

FIGURE 3.5 Flow chart for LC colour image-processing system.

FIGURE 3.6 Photograph of the image-processing system.

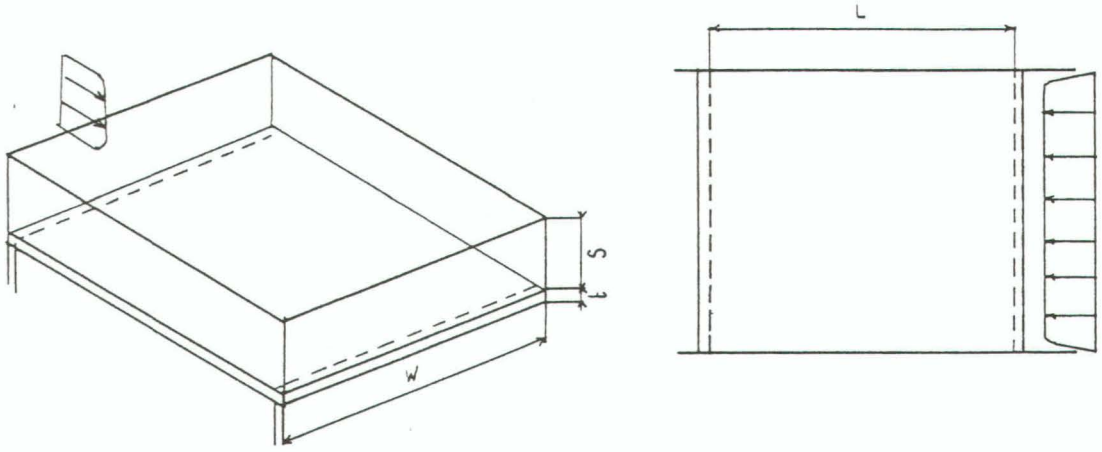

FIGURE 3.7 Test section for **flat plate** experiments.

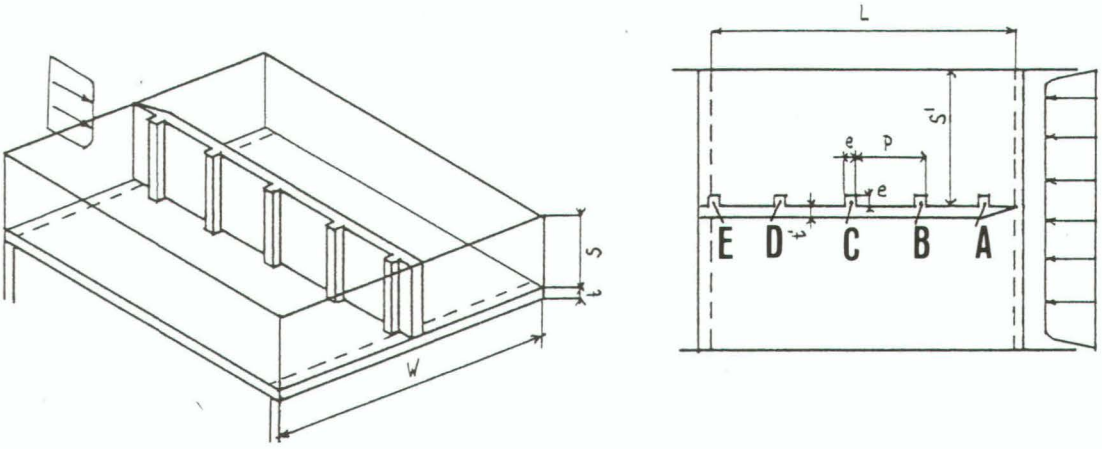

FIGURE 3.8 Test section for experiments on **rib-roughened configuration R1.**

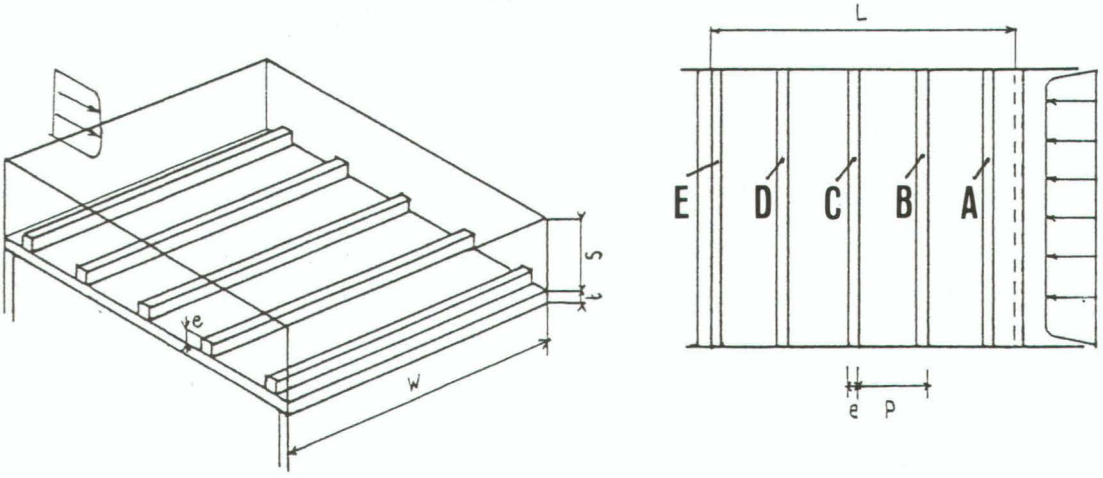

FIGURE 3.9 Test section for experiments on **rib-roughened configuration R2.**

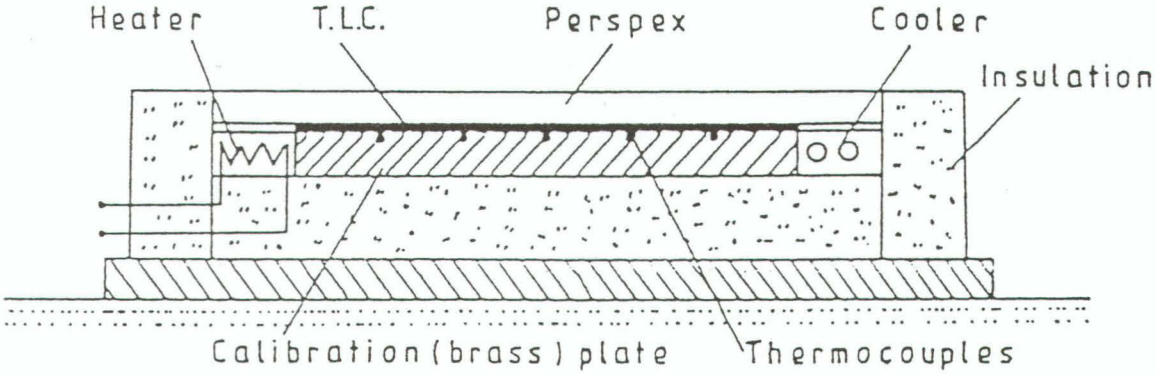

FIGURE 3.10 Sketch of the LC calibration apparatus.

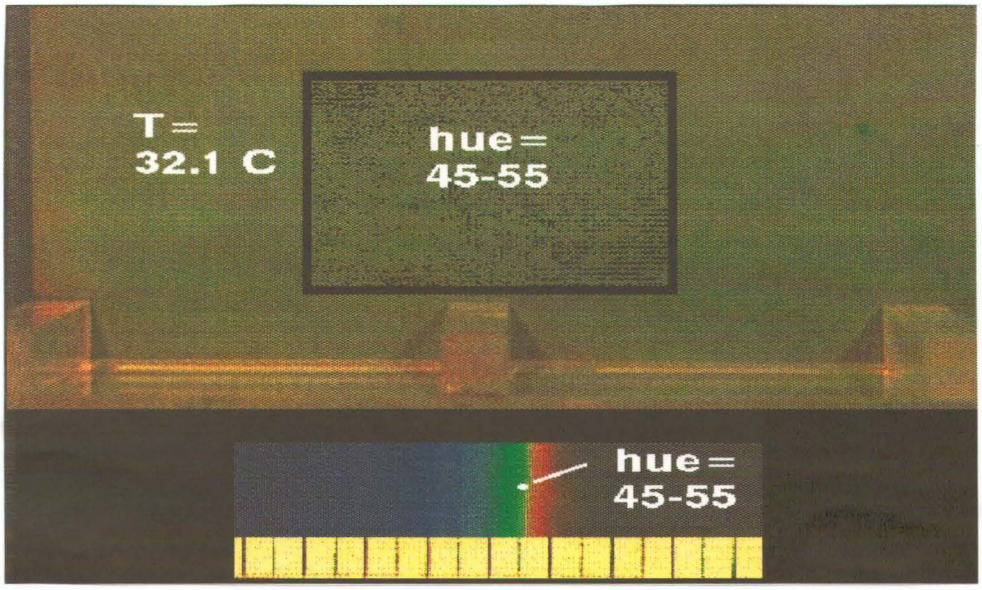

FIGURE 3.11 LC calibration experiments: colours exhibited by LC on the calibration plate (bottom), colour exhibited by LC on the test plate maintained at 32.1°C (top).

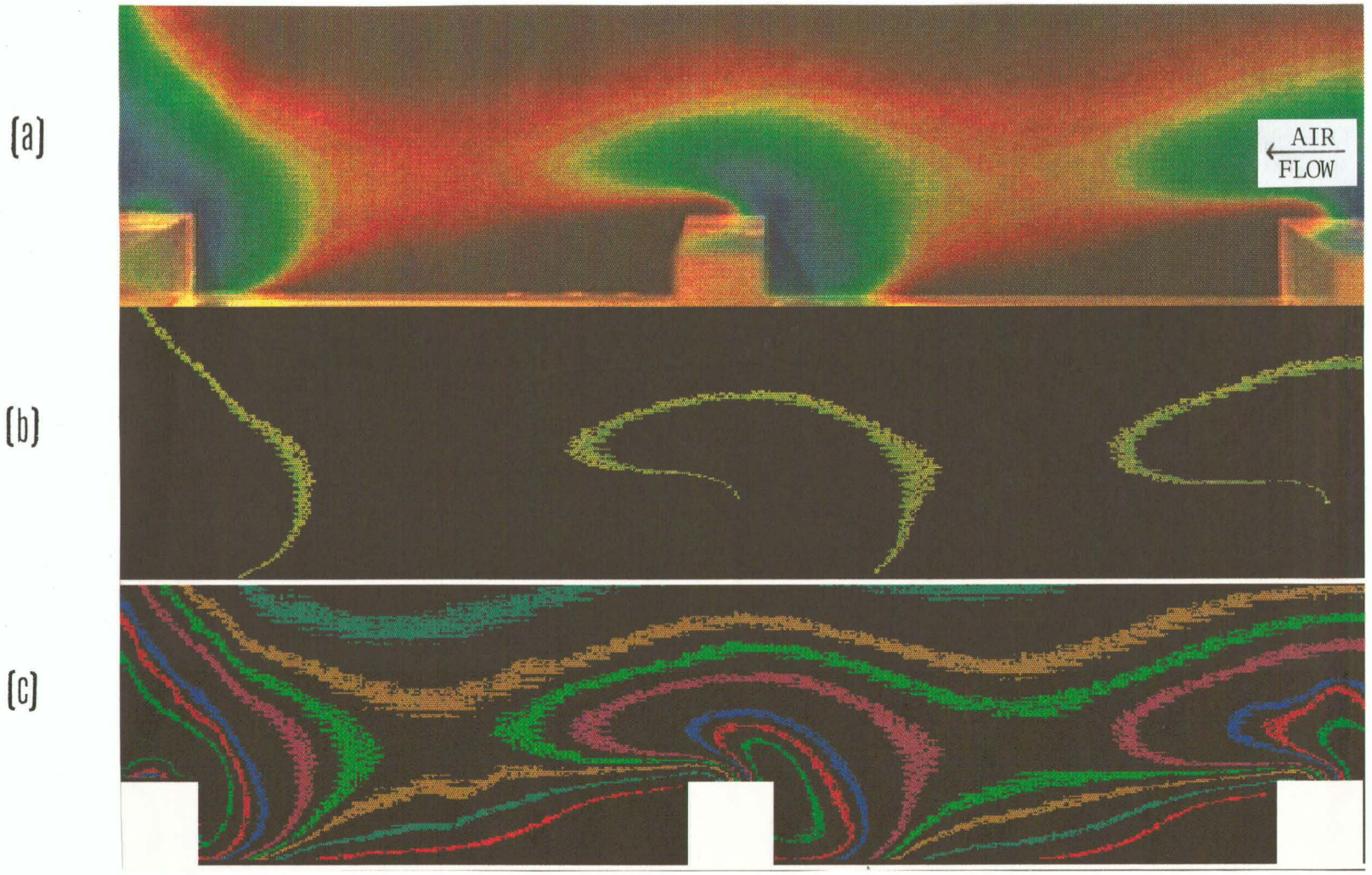

FIGURE 3.12 Image processing steps: (a) true colour image of the test plate under given flow and heating conditions, (b) selection of the green colour band corresponding to a given heat transfer coefficient,(c) false colour image with contours of heat transfer coefficient lines

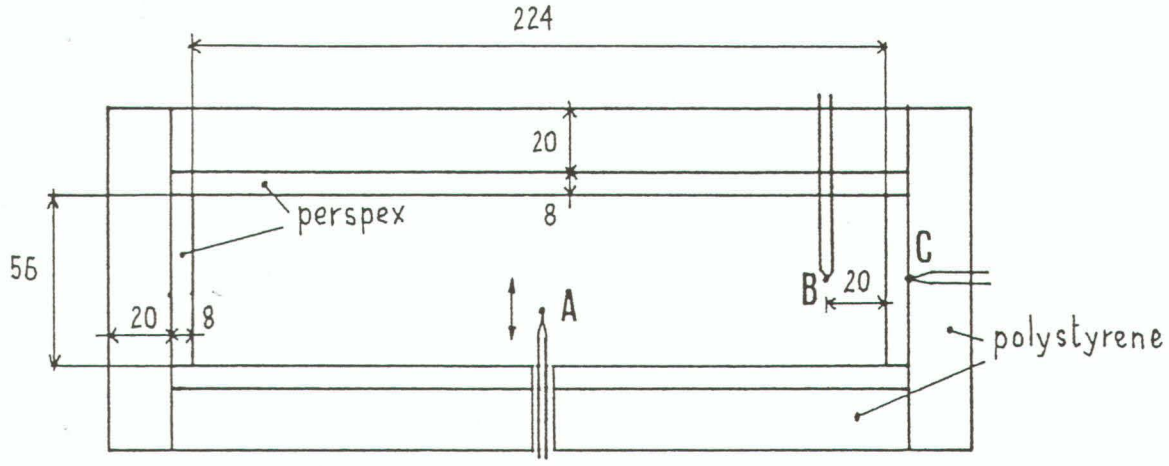

FIGURE 3.13 Test section inlet on a plane orthogonal to the main flow. Detail of thermocouple (A, B, and C) locations.

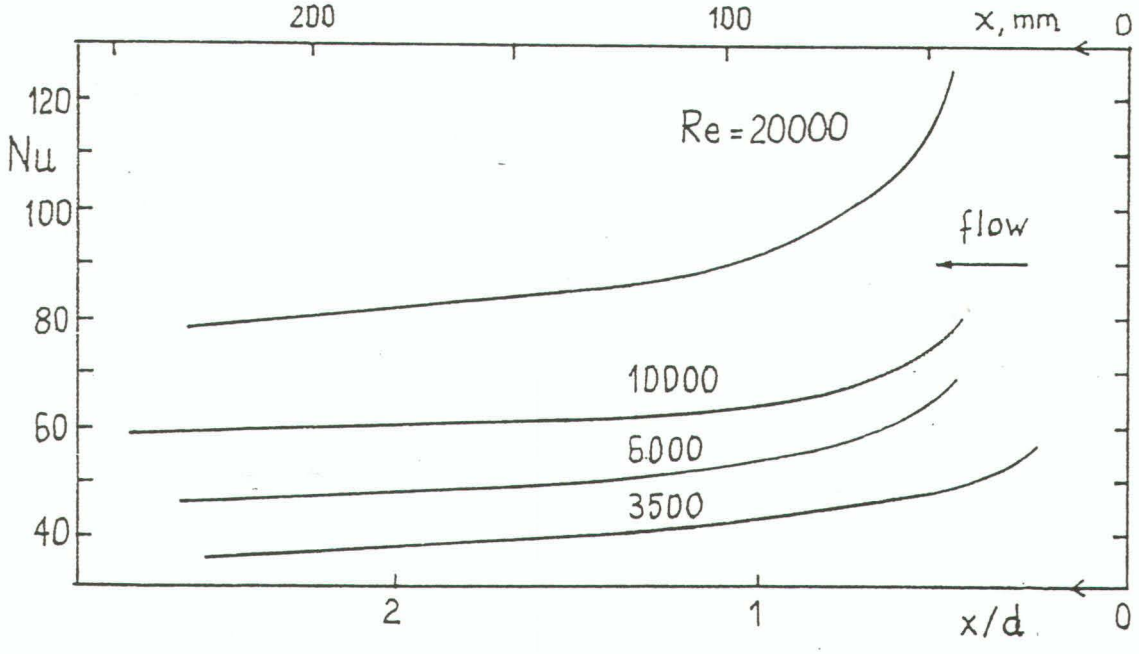

FIGURE 3.14 Nusselt number distributions along the flat plate.

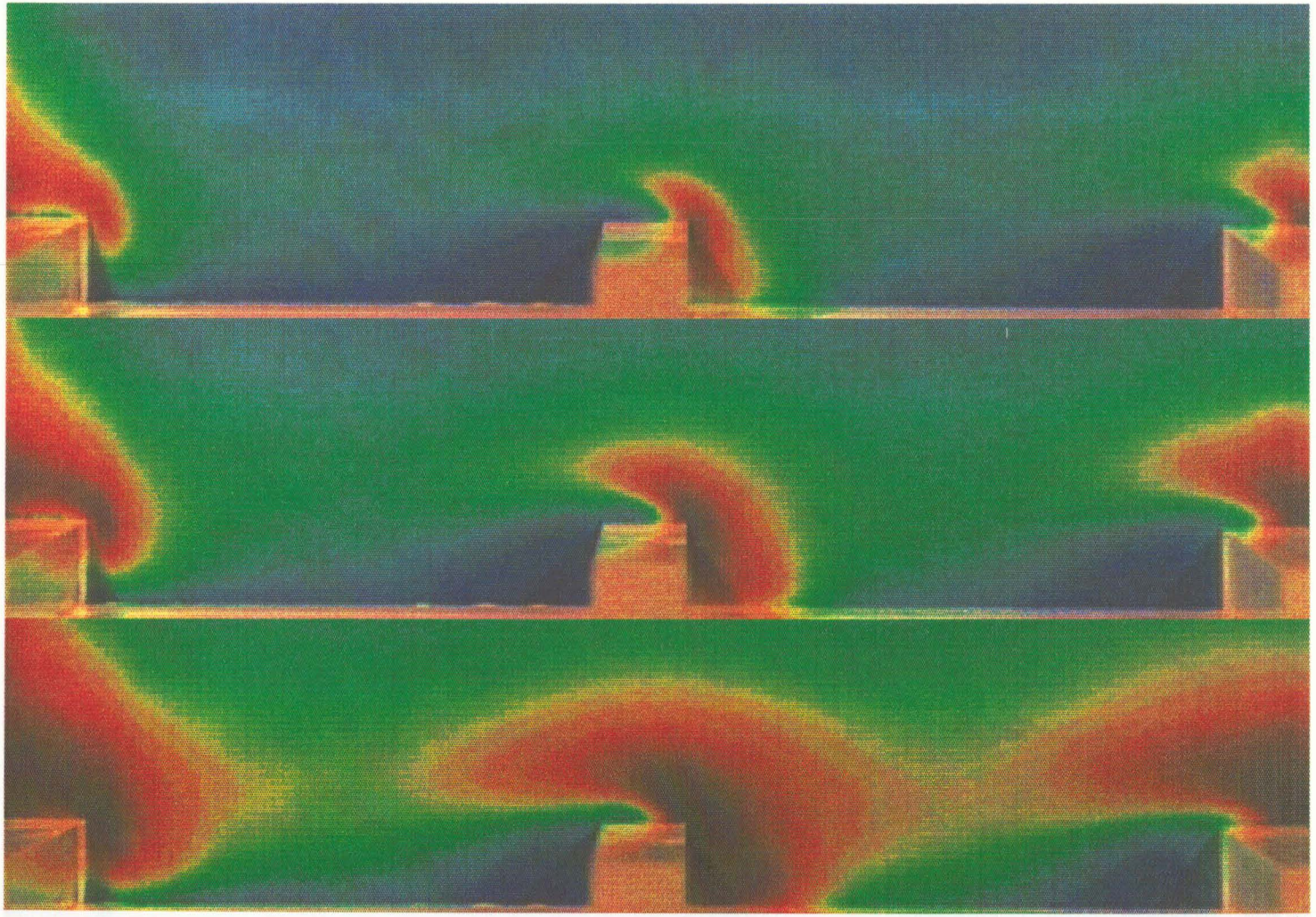

FIGURE 3.15 True colour images of the test plate (Config. R1) for Re=20000 and three different values of the water temperature (**HFU** upward heat flux conditions).

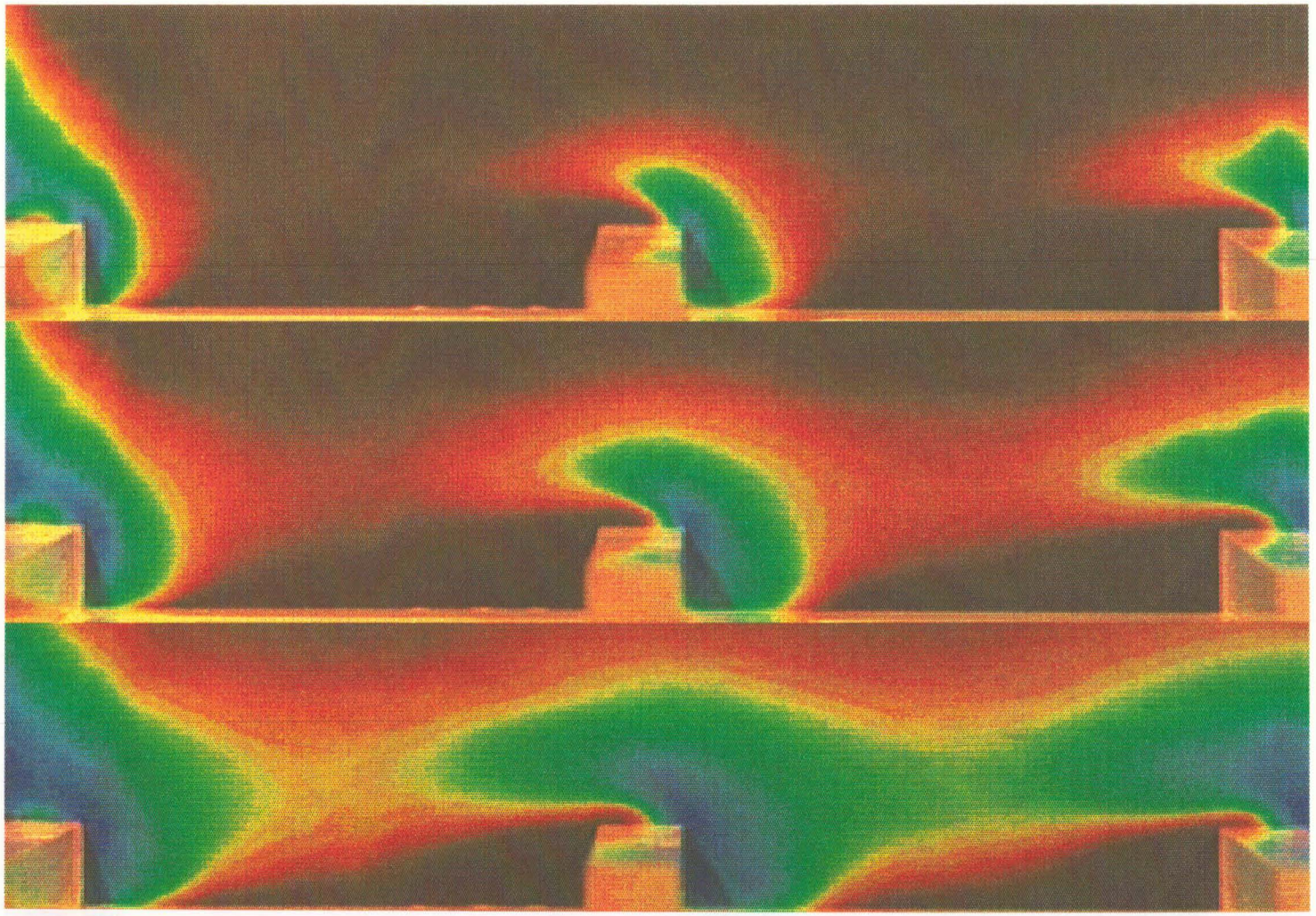

FIGURE 3.16 True colour images of the test plate (Config. R1) for Re=20000 and three different values of the water temperature (**HFD** downward heat flux conditions).

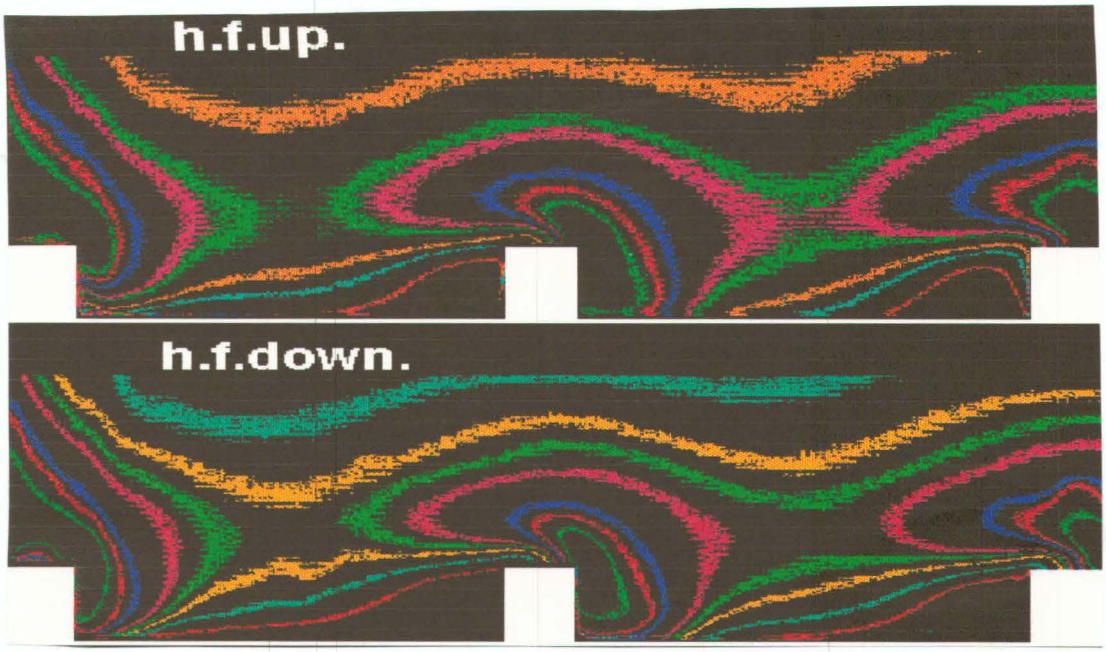

FIGURE 3.17 False colour images indicating the iso-Nusselt number lines for Re=20000 and **HFU** conditions (top) and **HFD** conditions (bottom).

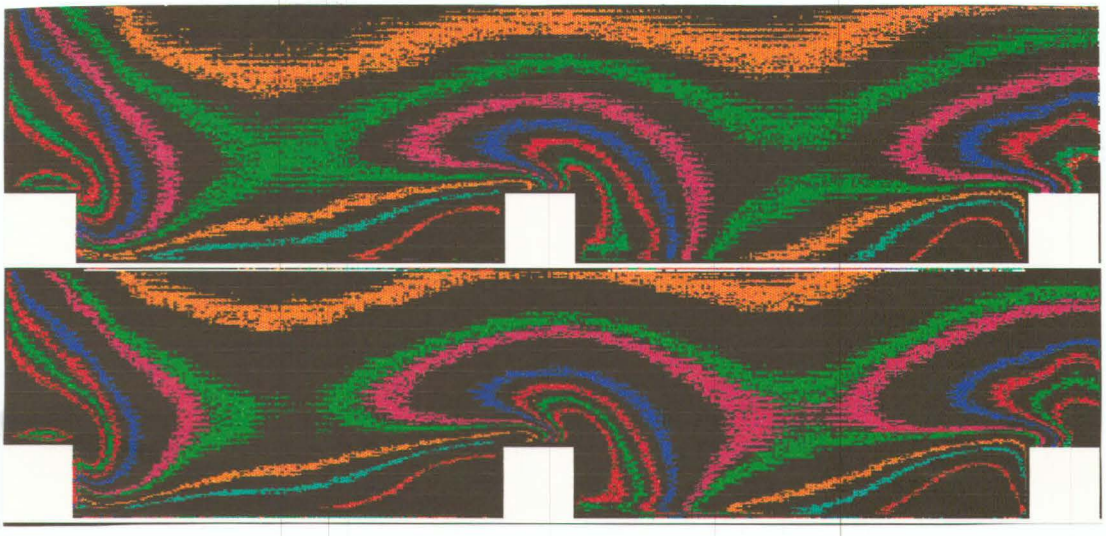

FIGURE 3.18 False colour images indicating the iso-Nusselt number lines for Re=20000: reproducibility test.

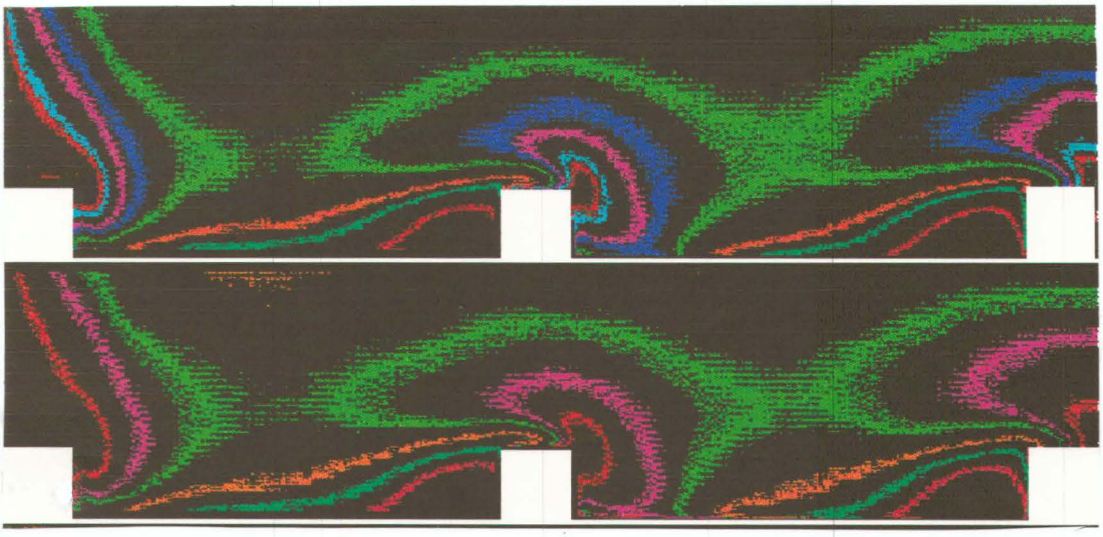

FIGURE 3.19 False colour images indicating the iso-Nusselt number lines for Re=10000: reproducibility test.

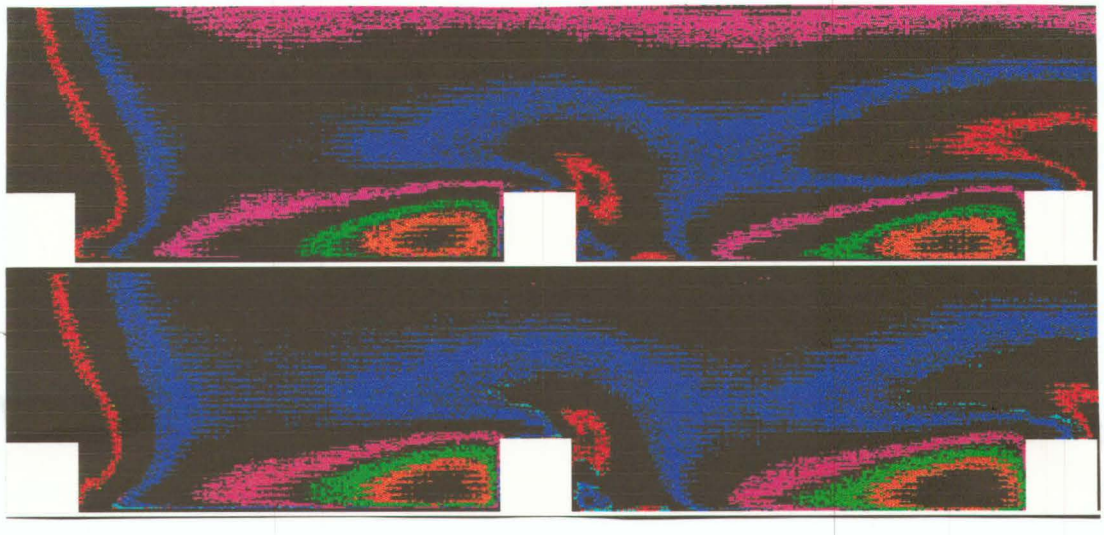

FIGURE 3.20 False colour images indicating the iso-Nusselt number lines for Re=3500: reproducibility test.

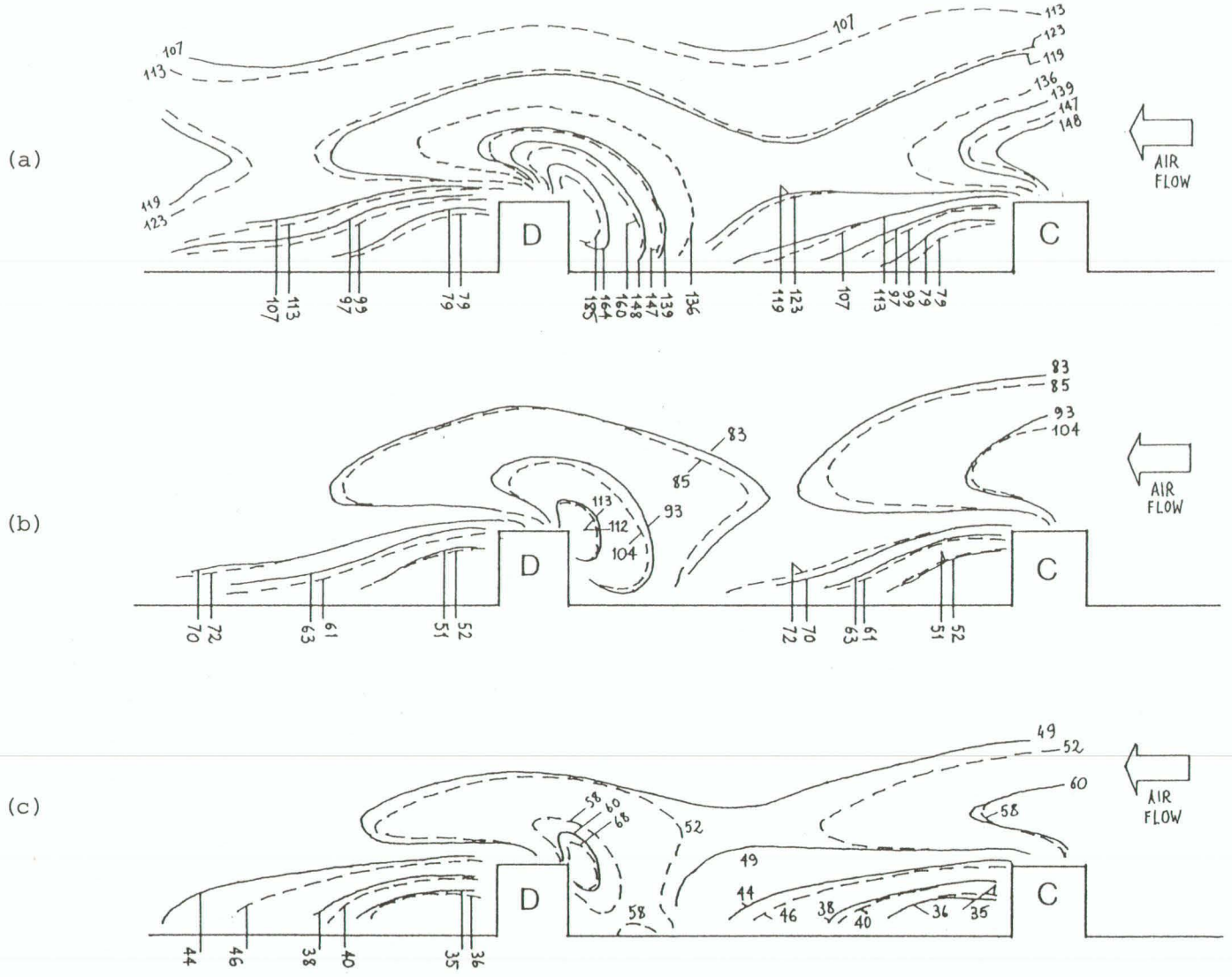

FIGURE 3.21 Comparisons between Nusselt numbers obtained in couples of tests performed in the same experimental conditions: (a) Re=20000, (b) Re=10000, (c) Re=3500.

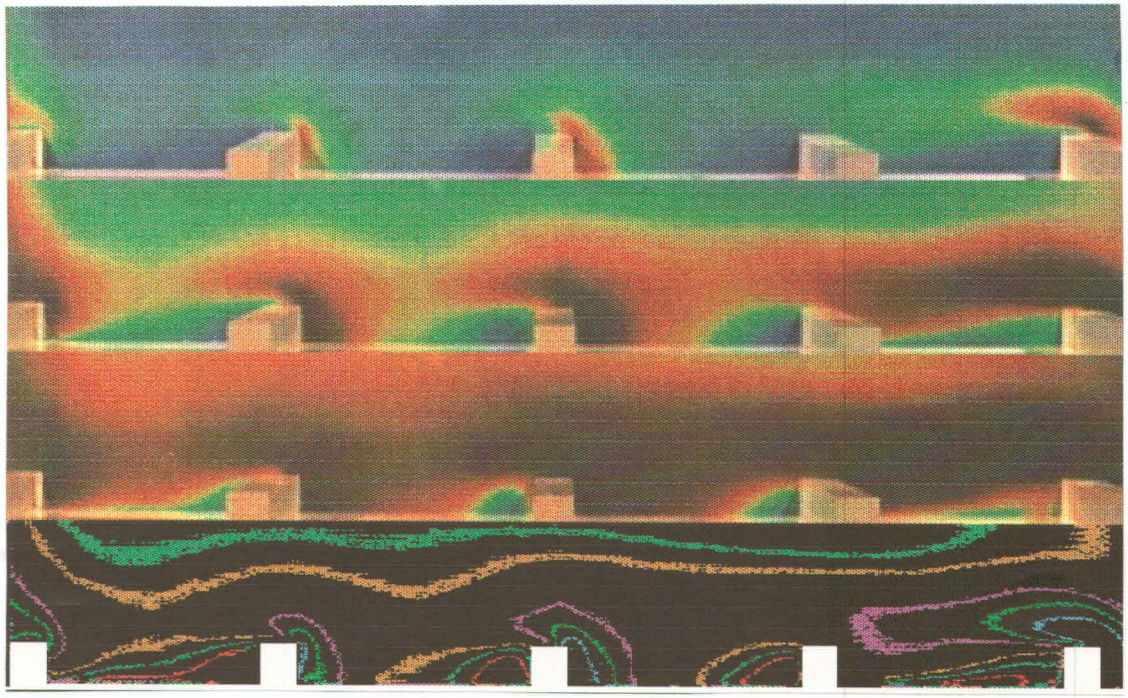

FIGURE 3.22 True colour images of the overall test plate and false colour image indicating the iso-Nusselt number lines, Re=20000.

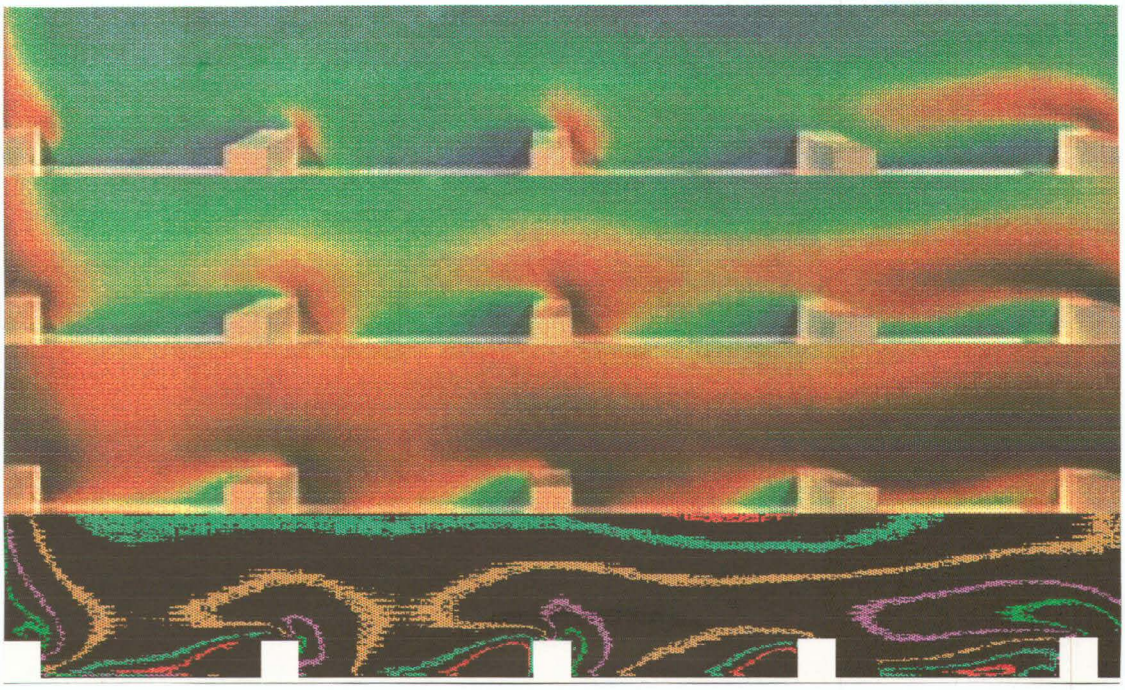

FIGURE 3.23 True colour images of the overall test plate and false colour image indicating the iso-Nusselt number lines, Re=10000.

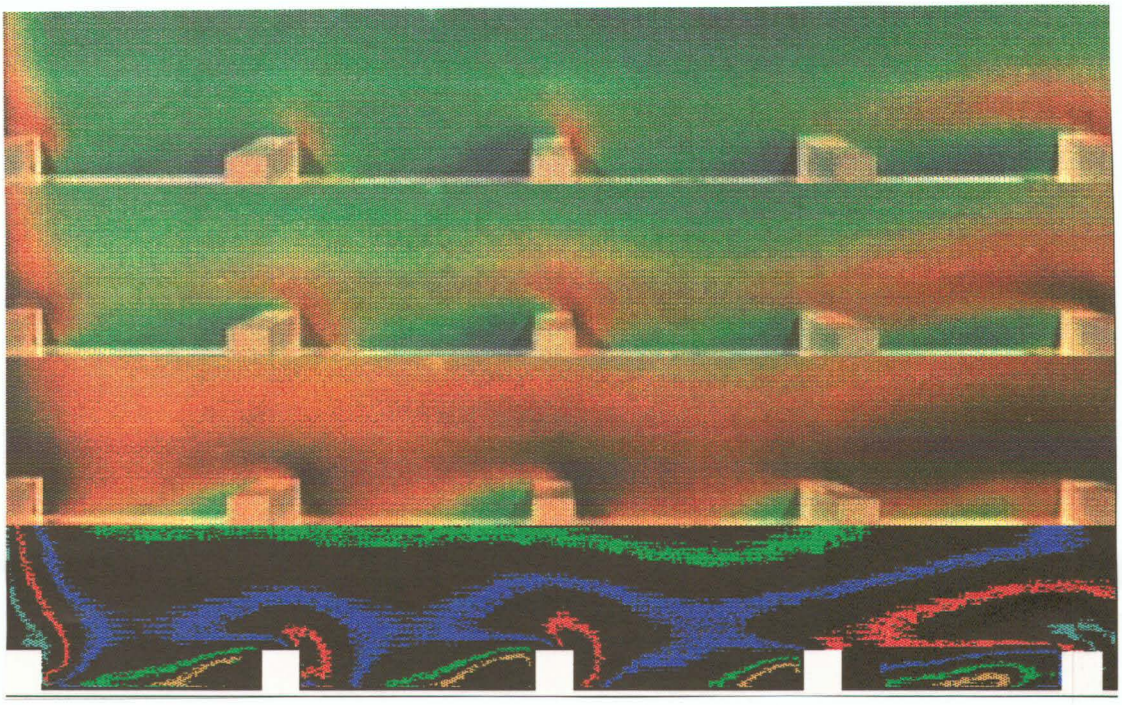

FIGURE 3.24 True colour images of the overall test plate and false colour image indicating the iso-Nusselt number lines, Re=6000.

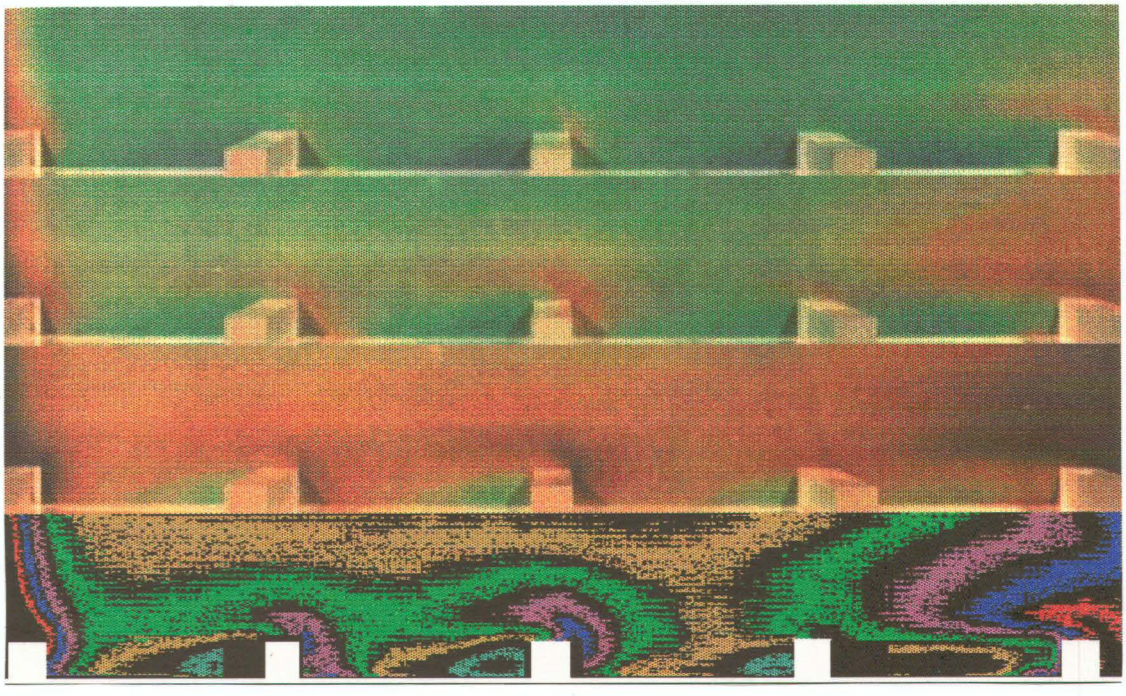

FIGURE 3.25 True colour images of the overall test plate and false colour image indicating the iso-Nusselt number lines, Re=3500.